Experimental Study of the Flow of a Vertical Axis Wind Turbine Farm for Atmospheric Boundary Layer Control

MSc Thesis

J.P.Mulay

Delft University of Technology

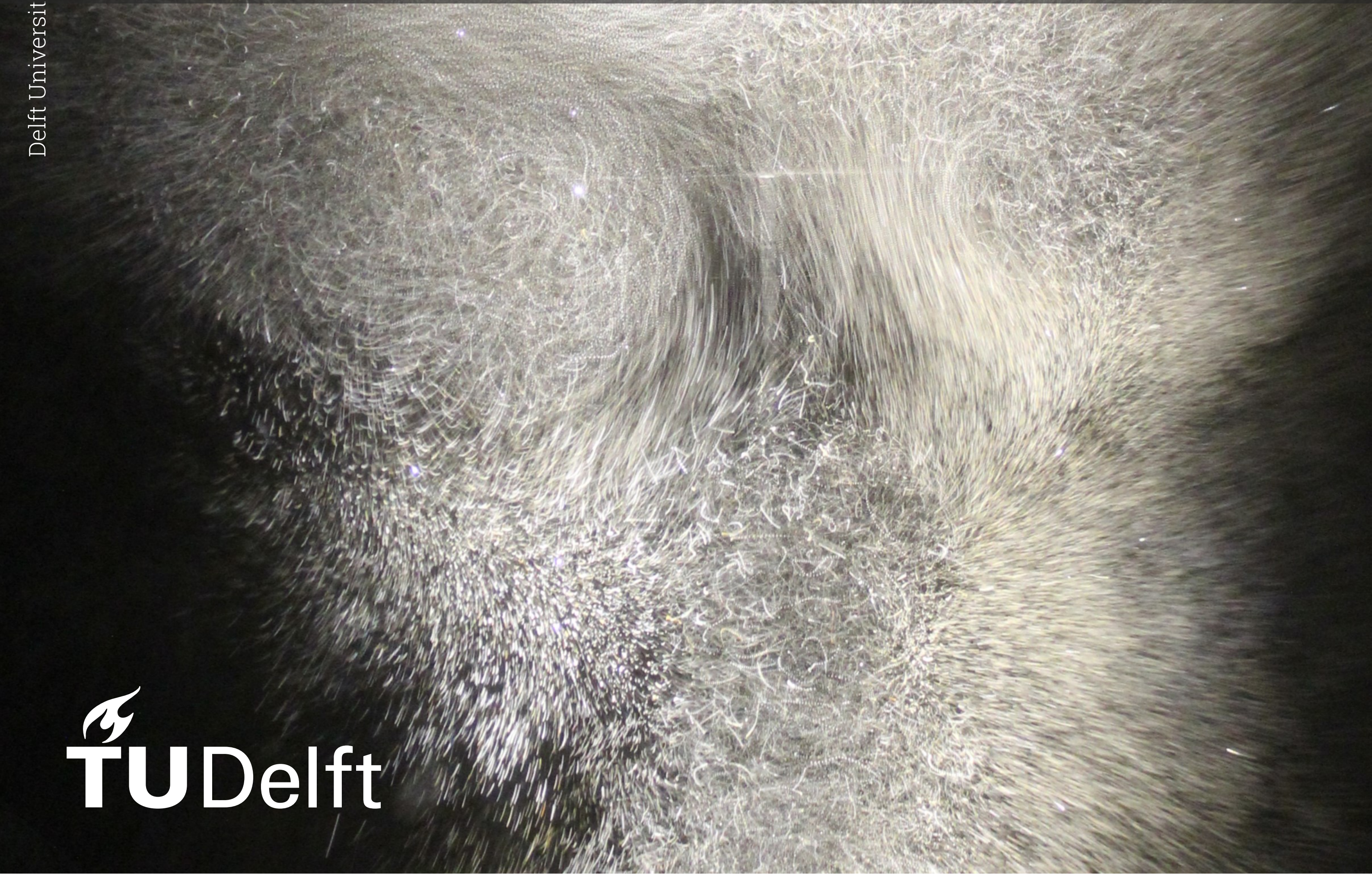

TU Delft

Experimental Study of the Flow of a Vertical Axis Wind Turbine Farm for Atmospheric Boundary Layer Control

by

J.P.Mulay

to obtain the degree of Master of Science
at the Delft University of Technology,
to be defended publicly on Wednesday August 28, 2024 at 15:00.

Student number:	5827833	
Project duration:	November , 2023 – August , 2024	
Thesis committee:	Prof. C.J. Simao Ferreira,	TU Delft, Supervisor
	Ir. D. Bensason,	TU Delft, Supervisor
	Prof. A. Sciacchitano,	TU Delft, Chair
	Prof. A. van Zuijlen,	TU Delft, External Examiner

An electronic version of this thesis is available at `http://repository.tudelft.nl/`.

TU Delft

Preface

This thesis marks the end of my Master's program in Sustainable Energy Technology, at Technische Universiteit Delft. The work carried out over the past nine months is summarized in this document. The transition from the electrical engineering domain into the field of aerodynamics was not an easy journey. Now, as I look back, I wish to extend my heartfelt appreciation and gratitude to all those who supported and guided me.

First and foremost, I want to express my sincere gratitude to Prof. Carlos Simão Ferreira and David Bensason, my supervisors. Carlos, your guidance and mentoring throughout the thesis was invaluable, and I thank you for supporting me as I dive into the world of aerodynamics. David, I am extremely grateful for your insights and for showing me the ropes of wind tunnel experiments. You were always there to patiently clear my doubts, and I could never ask for a better teacher. I also extend my thanks to Prof. Andrea Sciacchitano, for your guidance on the PTV setup, and suitable solutions for any of the issues faced during the experiment.

The success of this experiment would not be possible without the help of Dennis Bruikman, Gert-Jan Berends, and Peter Duyndam who provided their expertise on the design and operation of the experiment setup. Additionally, Frits Donker Duyvis, Henk-Jan Siemer, and the rest of the staff at the High Speed Laboratory played a significant role in the smooth execution of my experiment, for which I would like to express my appreciation. Special thanks to Clem, for assisting in the experiment, and Thomas, for helping me with the data processing.

My warmest thanks to my friends, Max, Shivank, Rohan, Karan, Rishabh, Vijay, Akshay, and Anand, for being a strong support system for me, throughout these years away from home. To my Jaagpad group, Shubham, Rupesh, Divye, and Shubhang, for the memorable year we spent together. Lastly, I want to thank Shriya, and my parents, for your unconditional love, inspiration and encouragement.

Jayant Mulay
Delft, August 2024

Abstract

Wind energy has been at the front of the world's transition to renewable energy sources, due to its sustainable nature and little adverse effects on the environment. This report sheds light on behaviour of vertical axis wind turbines (VAWTs) in a high density wind farm arrangement. VAWTs have been studied extensively in the past, but research interest in them has been rekindled, for their inherent compatibility with offshore environment.

The work presented in this thesis aims to study the effects of enhanced flow entrainment in a VAWT wind farm. This is achieved by advection of low momentum wake into the free-stream flow via lateral forces, and these forces are introduced by pitching the rotor blades. For this study, scaled down VAWT models have been designed and setup in a wind farm layout. This wind farm model has been tested in the Open Jet Facility (OJF) of the Delft University of Technology to gather insight into the farm's flow behaviour. The wake is acquired using Tomographic Particle Tracking Velocimetry (PTV) measurement technique, where the flow is measured by acquiring images of Helium Filled Soap Bubbles (HFSB), suspended in the flow-stream. The performance of individual turbines is characterized by taking the load measurements, and comparing the thrust coefficients.
From the analysis of thrust coefficients, changing the blade pitch angle increases the efficiency of downwind turbines. After implementing this change, the performance of second row turbines rises 2.6 times and third row turbine's performance increases by a factor of 1.6 when compared to the baseline case, where blade pitch is set to $0°$. This increase in efficiency is attributed to the wake deflection and flow advection, caused by introduction of lateral forces, which was studied using PTV. The PTV results clearly show that pitching the blades inwards to the axis of rotation cause the lateral deflection of wake, and pitching outwards lead to axial deflection, stemming from the shed vorticity. This resulted in the entrainment of high speed flow in the wind farm, and hence, an increase in available wind power within the farm was noted. The available power increases upto +181% when blades are pitched inwards, but shows a decreasing trend, which is linked to the interference of laterally deflected wakes of other turbines. On the other hand, axial wake deflection caused by pitching the blades outwards shows a rising trend, and a power increment of +100%.

Results from this work provide a step further for implementing VAWT based wind farms in real world scenarios. By characterizing the effects of wake deflection and their relation with pitch angle, a better design of such wind farms can be developed which can complement current designs and technologies.

Contents

List of Figures

List of Tables

Nomenclature

Abbreviations

Abbreviation	Definition
AC	Actuator Cylinder
AP	Available Wind Power
ABL	Atmospheric Boundary Layer
AEP	Annual Energy Production
ALM	Actuator Line Model
ANN	Artificial Neural Networks
CFD	Computational Fluid Dynamics
DL	Downwind Leeward
DW	Downwind Windward
FOV	Field Of View
FSU	Fluid Supply Unit
HAWT	Horizontal Axis Wind Turbine
HFSB	Helium Filled Soap Bubbles
HSL	High Speed Laboratory
IWFBL	Infinite Wind Farm Boundary Layer
LES	Large Eddy Simulation
NREL	National Renewable Energy Laboratory
O&M	Operation and Maintenance
OJF	Open Jet Facility
PIV	Particle Imaging Velocimetry
PTU	Programmable Timer Unit
PTV	Particle Tracking Velocimetry
STB	Shake The Box
TSR	Tip Speed Ratio
UL	Upwind Leeward
UW	Upwind Windward
VAWT	Vertical Axis Wind Turbine

Symbols

Symbol	Definition	Unit
A	Rotor Area	m^2
B	Number of blades	[-]
C_P	Power Coefficient	[-]
c_t	Areal Thrust Coefficient	[-]
C_T	Thrust Coefficient	[-]
C_{Tx}	Streamwise Thrust Coefficient	[-]
C_{Ty}	Lateral Thrust Coefficient	[-]
C_L	Lift Coefficient	[-]
C_D	Drag Coefficient	[-]
D	Rotor Diameter	m
D_f	Drag Force	N
f	Modified Coriolis Parameter	[-]

Symbol	Definition	Unit
$\mathbf{f}$	Force vector	[-]
f_N	Normal Force Distribution	[-]
G	Geostrophic Wind	m/s
h	Hub Height	m
H	Height	m
k	Von Karman Constant	[-]
L	Monin-Obukov length	m
L_f	Lift Force	N
P	Power	W
P_D	Power Density	W/m^2
Re	Reynolds's Number	[-]
T	Thrust	N
u	Wind Velocity	m/s
U_∞	Freeflow Wind Speed	m/s
u^*	Frictional Velocity	m/s
z	Height	m
z_0	Surface Roughness	m
α	Angle of attack	$degrees(^\circ)$
θ_p	Pitch angle	$degrees(^\circ)$
λ	Tip Speed Ratio	[-]
ρ	Density	kg/m^3
ψ_M	Stability Coefficient	[-]
ω	Vorticity	$1/s$
ω_m	Angular Velocity	$^\circ/s$

1
Introduction

The Paris Agreement held by the United Nations aims to hold global warming below 2 °C and pursue a 1.5 °C target. Predictions using Artificial Neural Networks (ANNs), trained on modeling climate change, suggest crossing the 1.5 °C threshold in between 2033 to 2035 [16]. To achieve the set targets and avoid large scale damage, significant research needs to be conducted to evolve the conventional renewable energy generation technology.

Wind energy has become more significant as a viable substitute for conventional fossil fuels, due to its sustainable nature and little adverse effects on the environment. The growing demand for renewable energy necessitates the need to optimize the efficiency and productivity of wind energy installations. The up-scaling of 3 bladed horizontal axis wind turbine (HAWT) has been a common practice since the past few years [55] [56], following the trend of moving wind farms offshore [44]. This up-scaling has led to longer wakes as a result of the large rotor diameter. When placed in a wind farm layout, the interaction of multiple wakes creates a low velocity turbulent flow that deviates extensively from the Atmospheric Boundary Layer (ABL) wind profile, encountered by the first few rows of the wind farm. The wind speed deficit and available power inside wind farms are significantly influenced by the stability of ABL [4], [25]. This flow inside the "infinite" wind farm re-energizes by vertical kinetic energy transport, associated with atmospheric stability and turbulent mixing, from which a performance limit for wind farms can be evaluated [43]. Figure 1.1 shows this wind farm boundary layer and entrainment of momentum into the layer, where U_o is outer velocity, U_b is characteristic velocity for the interior of the boundary layer, U_f is wind farm velocity, h_f is height of the wind farm, and $h_B(x)$ is height of the boundary layer as a function of streamwise distance x.

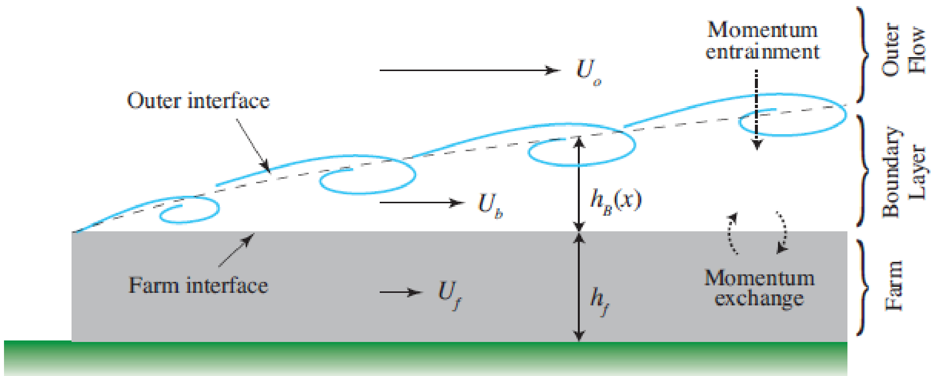

Figure 1.1: Schematic of vertical entrainment of momentum in HAWT wind farms. Figure reproduced from [43]

The wake induced mixing process depends on the ejected blade tip vortices, their instability, and breakdown, which further relies on the stability of the atmosphere. As this process of wake diffusion and entrainment of kinetic energy is slow, enhancing it is a challenge faced in current HAWT wind farms. One of the alternative technologies that shows promise to solve this challenge of vertical kinetic energy entrainment is the vertical axis wind turbine (VAWT).

The interest in vertical axis wind turbines (VAWTs) has been growing recently, resulting from the awareness of turbine up-scaling limitations, lower Operation & Maintenance (O & M) and capital costs, and their compatibility with offshore conditions. Studies pertaining to the wake of VAWT show shorter wake length, and enhanced vertical flux as compared to a HAWT, allowing for higher wind farm density [14]. Flow advection is known to be required for the enhancement of momentum recovery, which has already been accomplished with VAWTs [32]. To assume that VAWT wind farms would perform better than the HAWT counterparts, and show higher magnitude vertical energy transfer, the effects of advection must be studied on a wind farm scale.

The objective of this thesis is to experimentally study the flow inside a VAWT wind farm, with the aim of proving the above assumption. In this experiment conducted in TU Delft's Open Jet Facility, measurement of the flow inside a scaled 3 x 3 H-rotor VAWT wind farm model is undertaken, where flow entrainment is amplified by changing the rotor's blade pitch angle. This technique increases the vorticity shed by VAWTs, making them act as vortex generators. The impact of this enhanced entrainment on the performance of wind turbines and available wind power in the wind farm is studied by obtaining load measurements and performing Tomographic Particle Tracking Velocimetry (PTV).

This report is structured in five different chapters. Following the current introduction chapter, the theory behind wind farm aerodynamics, VAWT aerodynamics, VAWT wake topologies, and wake control methods are briefed in Chapter 2. The chapter ends with the formulation of research questions which will be answered in this thesis study. Chapter 3 highlights the methodology where details about the experiments are presented. Chapter 4 presents the results of the experiments and the conclusions reached from the data are discussed in chapter 5, along with future recommendations.

2 Literature Review

As mentioned in the introduction, this chapter covers important studies about wind farm aerodynamics and wake control methods implemented in them. Then, the aerodynamics of VAWTs are discussed thoroughly, along with the correlation between wake topology and forces on the rotor. Experimental techniques and methods are presented afterward, and the chapter concludes with the research questions.

2.1. Wind Energy

The origin of wind is the result of temperature variations across the earth's surface, causing pressure differences which lead to the formation of circulation cells. The rotation of the earth causes the Coriolis force which opposes the pressure gradient force. This creates wind moving parallel to isobars when the pressure gradient force and Coriolis force are in equilibrium. The resulting wind is called the Geostrophic wind. As we move lower towards the surface of our planet, the drag force needs to be considered, caused due to surface roughness. This drag force is always opposite to the direction of the wind and shifts the wind towards lower pressure. The friction caused by the surface shears the wind and creates turbulence. This combination of turbulence and Coriolis force leads to the formation of the atmospheric boundary layer (ABL). Details on relevant atmospheric sciences behind the formation of wind are presented in the work of Stull [59].
The ABL is divided into three layers. The Geostrophic wind, with velocity magnitude G, lies on the top of the ABL. The Ekman layer resides below the Geostrophic wind layer, where variation in wind direction is observed. The lowest layer of the ABL is labelled as the Surface layer with a height range from 40m-100m, where the magnitude of wind speed changes. Inside the boundary layer, the velocity profile is driven by pressure forces. The velocity distribution and turbulence intensity within the flow are determined by thermal stratification. Further details can be found in the work of Monin [45] regarding the analytical modelling and dynamics of the boundary layer.

For power generation using wind farms, the surface layer is considered important. Equation 2.1 gives the theoretical expression for the wind shear in the surface layer, to find the average wind velocity u at height z.

$$u(z) = \frac{u^*}{\kappa}\left[\ln\left(\frac{z}{z_0}\right) - \Psi_M\left(\frac{z}{L}\right)\right] \tag{2.1}$$

In this equation, u^* is the friction velocity, κ is the Von Karman constant and z_0 is the surface roughness length. The term $\Psi_M(\frac{z}{L})$ represents the stability of the ABL, where L is the Monin-Obukhov length, and is considered zero for neutral conditions.

2.1.1. Future Goals for Wind Energy

According to the European Commission's Impact Assessment [47], achieving the 40% renewable energy objective will need 453 GW of wind energy production in the EU by 2030, (374 GW onshore and 79 GW offshore). The total amount of wind farm capacity that must be installed by 2030 to meet the energy production targets decreases to 325 GW for onshore farms and 59 GW for offshore farms when taking into account today's sophisticated and efficient turbines and using conservative capacity factors of 45% and 35% for offshore and onshore farms, respectively.
Targets set by the Netherlands are presented in the Dutch North Sea Programme 2022-2027 report [46]. Regarding offshore wind energy, two future scenarios were discussed for the sustainable energy supply of the country in the year 2050. The first import-dependent case has a target of 38GW installed offshore wind power with 170 TWh/year energy yield, and the second self-sufficient case sets a target of 72GW offshore power with 325TWh/year yield. A power density of $10MW/km^2$ was determined as a starting point, making the wind farm areas $3800km^2$ and $7200km^2$.
From this data, the calculated capacity factors are 51% and 51.52% for import-dependent and self-sufficient cases respectively.

A numerical prediction model was developed by Sørensen and Larsen [58] to determine the energy production and costs of offshore wind farms. Predicted results from the model were validated against the observed data from multiple existing wind farms and were found to be in agreement. This model was further implemented to assess the offshore wind power production in the North Sea [57]. Analysis of power density and capacity factor of the wind, as a function of turbine spacing S, for different rotor diameters was performed, and presented in the following figures below

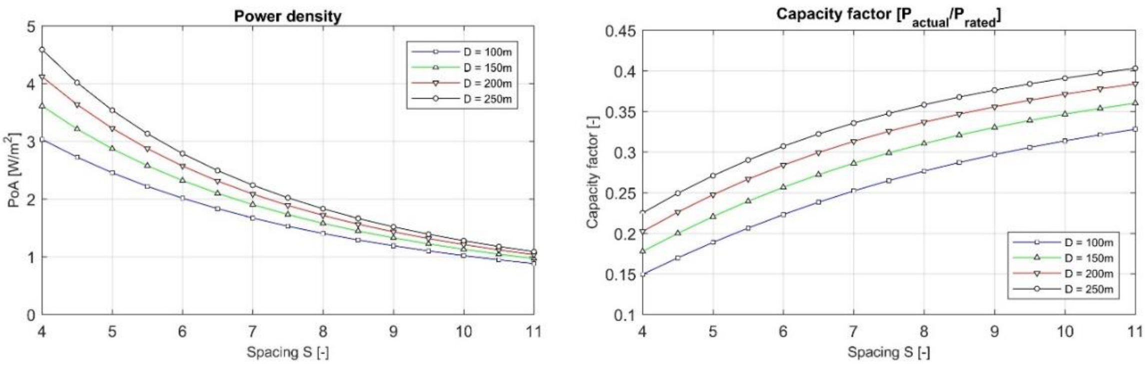

(a) Power Density function

(b) Capacity Factor function

Figure 2.1: Numerical Model prediction of North Sea wind resource by Sørensen et.al.[57].

From the above plots, we can observe that reaching a capacity factor of 51% would require a larger rotor diameter than 250m, or an increase in the turbine spacing S. Considering a rotor diameter of 200m, the highest achievable capacity factor for S=11 is 38%. However, this would lead to a deviation in the proposed power density of $10MW/km^2$, as increasing the turbine spacing leads to the reduction in power density of wind farms, as per Figure 2.1a.
Thus, to fulfill the set targets of the North Sea Programme, more power needs to be extracted by the wind farms, which can be achieved by increasing the wind speed inside the wind farm. To understand the wind profile and the factors governing the wind speed in a large wind farm, we look at the infinite wind farm boundary layer model developed by Frandsen.

2.1.2. Infinite Wind Farm Boundary Layer

The infinite wind farm boundary layer model developed by Frandsen [22] aims to find the wind speed inside the wind farm, where deviation from the ABL profile is seen. The model assumes that all turbines are similar in terms of type and dimensions. He states that two layers are formed at the hub height, one above and the other below the level. Their shear is linked together based on the frictional velocities of the two layers. Representation of this model is given in Figure 2.2 below.

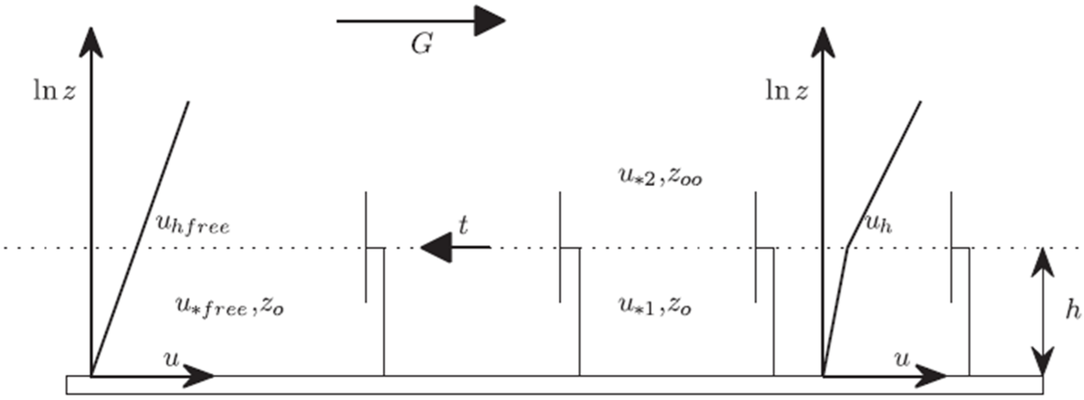

Figure 2.2: Infinite Wind Farm Boundary Layer model by Frandsen. Image taken from Peña and Rathmann[48]

This developed wind velocity inside the wind farm, is given by Equation 2.2 below.

$$u(h) = \frac{G}{1 + (1/k)\ln(\frac{G}{f \cdot h})\sqrt{c_t + (\frac{k}{\ln(h/z_0)})^2}} \tag{2.2}$$

where h is the hub height , f is the modified Coriolis parameter, c_t is the areal thrust coefficient distributed homogeneously.
Peña and Rathmann [48] extended this model to account for atmospheric stability based on MOST (Monin Obukov Similarity Theory). Equation 2.3 gives the wind speed for this extended model.

$$u(h) = \frac{G}{1 + (1/k)[\ln(\frac{G}{f \cdot h}) + \Psi_M(\frac{h}{L})]\sqrt{c_t + (\frac{k}{\ln(h/z_0) - \Psi_M(\frac{h}{L})})^2}} \tag{2.3}$$

The research pointed out that wind speed reduction has a greater dependency on atmospheric stability than roughness length.
The recovery of wind speed within the wind farm is dictated by the rate of mixing between the flow layers. Cal et al. [8] and Calaf, Meneveau & Meyers [9] demonstrated that energy extraction in the wind farm is dominated by the vertical turbulent transport of kinetic energy from the boundary layer towards the turbine hub height level.
In the work of Hamilton et al. [24], the mechanics of vertical replenishment of mean-flow kinetic energy are studied. This vertical entrainment of momentum is caused by large-scale structures within the flow and is important for the power extraction of downstream turbines. Verhulst and Meneveau [63] used artificial vertical forcing to analyse the vertical entrainment of mean kinetic energy in a wind farm. The artificial axial forcing was performed in both directions, where upward forcing resulted in significant power gains compared to the downward forcing of the flow. Similar results are observed in the experimental work of Bossuyt et al. [6], where vertical force was induced by tilting the rotor of a HAWT model. The results of these studies indicate that higher power production in wind farms could be obtained through increased vertical transport of kinetic energy. Schematic representation of rotor tilt and subsequent wake movement is presented in Figure 2.3 below, where U is incoming wind speed, D is rotor diameter, and γ is negative tilt angle. The dashed line represents the downstream propagation of the wake without rotor tilt, and the blue lines depict the wake path when tilt is introduced.

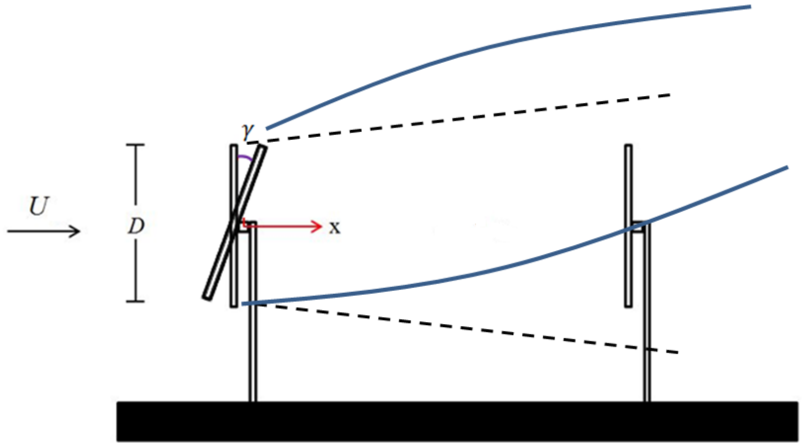

Figure 2.3: Schematic of vertical wake deflection by the introduction of rotor tilt. Figure adapted from [2]

The above method is implemented to control the wake of a wind turbine. These control methods are discussed in the next section, after addressing the aerodynamics of a horizontal axis wind turbine's wake.

2.2. Wake of HAWT

The wake of a wind turbine can be described as low velocity, high turbulent flow behind the rotor plane, occurring as a result of energy extraction from incoming wind. The wake of a horizontal axis wind turbine is a complex 3D helical structure, which can be split into two parts, near wake and far wake. The near wake region can be characterized by the drop in wind speed and from the structure of blade root and tip vortices, with a length of 2 to 4 rotor diameters. The wind speed regeneration happens in the far wake region of a HAWT. Here, the vortices formed in the near wake region are broken down by the external turbulence, caused by the interaction of undisturbed wind outside the stream tube and lower wind speed inside the stream tube. Vermeer et al [64] has surveyed and presented most of the research conducted on the above wake regions. The following figure by Porté-Agel [49] displays a representation of the wake regions and velocity profiles. There, $\bar{u_\infty}$ is the far upwind streamwise velocity component, $\bar{u}$ is the streamwise velocity component profile along the rotor axis in blue, $\Delta\bar{u}$ is the velocity deficit profile in red, and grey shaded area represents the wake of the wind turbine.

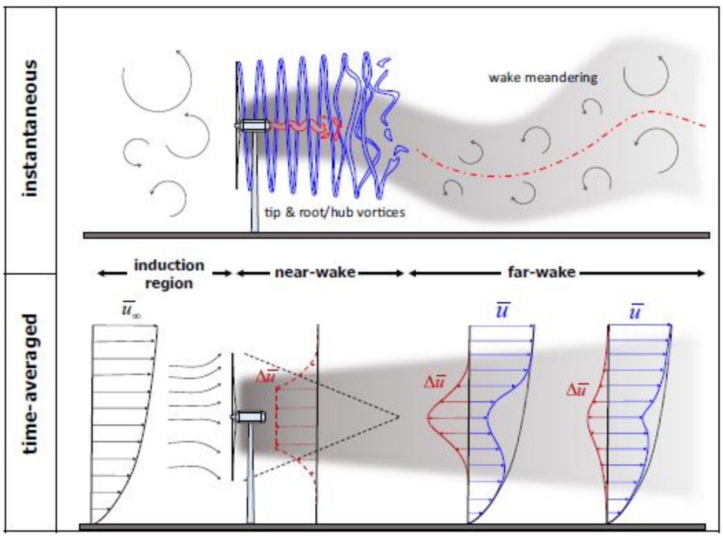

Figure 2.4: Wake of a Horizontal Axis Wind Turbine. Figure reproduced from [49]

Another observed phenomenon regarding HAWT wakes is wake meandering, described as the lateral movement of the wake, both horizontally and vertically, with respect to the wake's time-averaged central line. Although its origin is speculated, this phenomenon is observed in reality and should be considered, as these oscillations can lead to unsteady loading of downwind turbines [12]. The earliest study about wake meandering can be traced back to Ainslie [1], including this effect's correction in the wake prediction mathematical model, while examining the wake decay. The eddy viscosity model implemented in this study incorporated the turbulent mixing in the wake and ambient atmospheric turbulence. The main driving mechanism behind the wake decay is associated with the instability of tip vortices, ejected from the blades of the HAWT. The detailed study of the re-energization of wake has been presented in the dissertation of Lignarolo [41]. There, the analysis of tip vortex pairing instability, termed leapfrogging, was shown to amplify the breakdown and diffusion of the tip vortex. Post-breakdown, existing flow fluctuations were able to increase the efficiency of flow mixing, in the near wake. The visualization of tip vortices conducted by Lignarolo is shown in Figure 2.5.

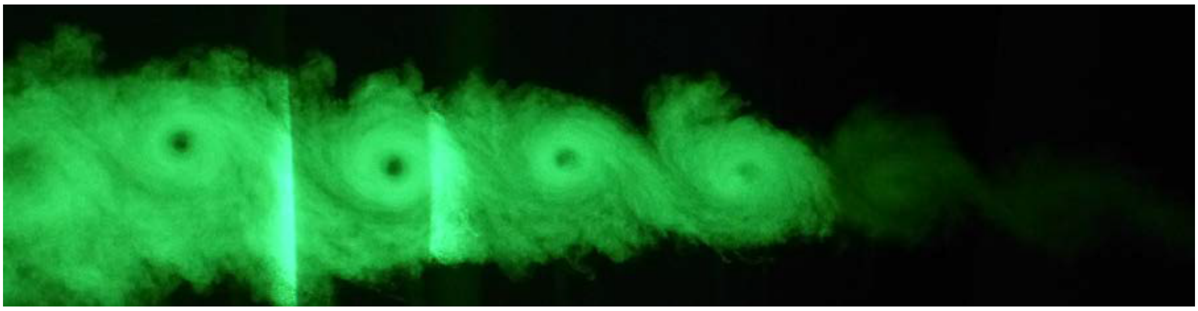

Figure 2.5: Visualization of tip vortices of a HAWT. Figure taken from [41]

2.2.1. Wake control for HAWTs

Yaw Control

The most commonly implemented method of wake control of HAWTs is wake steering by inducing lateral forces through the yawing of the turbine. This has been shown to increase the efficiency of wind farms and reduce turbulent loading on downwind turbines, at the cost of lower power production by upwind turbines. When the turbine is yawed, the reaction force of the rotor is at an angle to the incoming wind and gains a lateral component, responsible for the deflection and deformation of wake. The result of yawing on the wake's shape is presented in Figure 2.6.

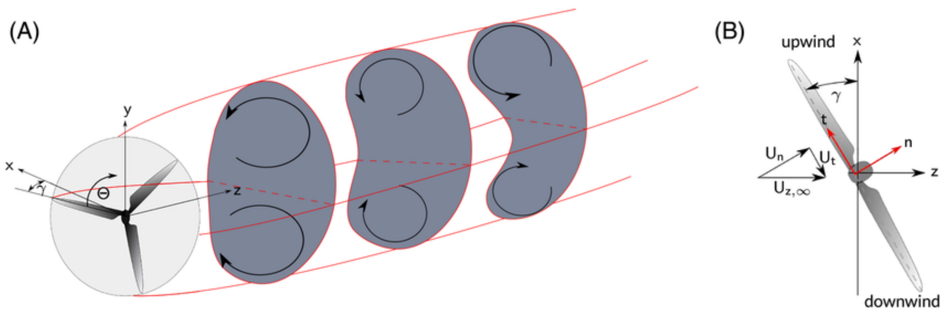

Figure 2.6: A) Schematic of wake development behind a yawed wind turbine. B) Top view showing yaw misalignment along the vertical axis y by yaw angle γ. Figure taken from [37]

Forces are induced by changing the inflow angle on the rotor either by yawing or tilting the turbine's rotor, as seen in the work of Jimenez [33]. Lateral deflection occurs when the yaw angle is changed, and vertical deflection is seen when the rotor is tilted. In the work of Howland et al. [29], the lateral deflection of the wake of an actuator disk model in yawed conditions was studied using hot wire anemometry. The result is depicted in Figure 2.7. LES results were used to confirm the observations of the wake curling, giving it a kidney shape. Further LES simulations performed by Fleming et al. [19] study the counter-rotating vortexes caused by yaw misalignment. It was found that the effect of resulting vorticity

on the downwind turbine lead to wake deflection, even when yaw misalignment was absent in that downwind turbine. Numerical optimization of Princess Amalia Wind Park was carried out by Fleming et. al. [21], using the software package SNOPT. The yaw control optimization was found to have the most contribution among different cases, where the power density of the wind farm increased by 7.7%. Stereoscopic PIV was implemented to study the turbine wake for different yaw angles by Bastankhah and Porte-Agel [5]. In this work, the formation of a counter-rotating vortex pair (CVP) was analysed and explained using the continuity equation. It was seen that spanwise force introduced by yawing lead to flow acceleration in the wake center and was counterbalanced by flow in the opposite direction at the wake's top and bottom regions in order to maintain continuity. The PIV results depicting the deformed wake are presented in Figure 2.8. An experimental study of this wake control strategy in a wind farm setup was carried out by Campagnolo et. al. [10], where a power increase of up to 21% was noted.
Field tests of wake steering controllers have resulted in improved total power production. Howland et al. [28] implemented already optimised yaw angles, based on prior wind data, for a 6-turbine array site and calculated the increase in annual mean power production to be between 7 to 13 %. Fleming et al. [20] also tested a controller that accounted for the dynamic behaviour of the turbine yaw actuator and instantaneous changes in the wind direction. This approach resulted in a reduction in the recorded wake losses by 6.6 % when implemented for specific inflow wind directions.

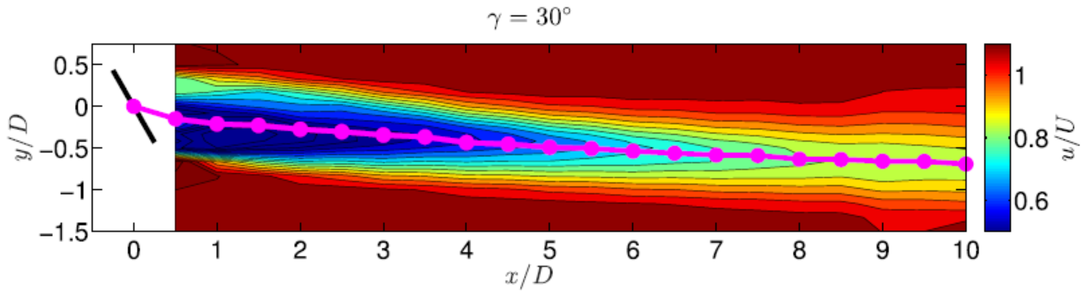

Figure 2.7: Streamwise velocity contour for 30° yaw angle with wake centers shown in magenta. Figure taken from [29]

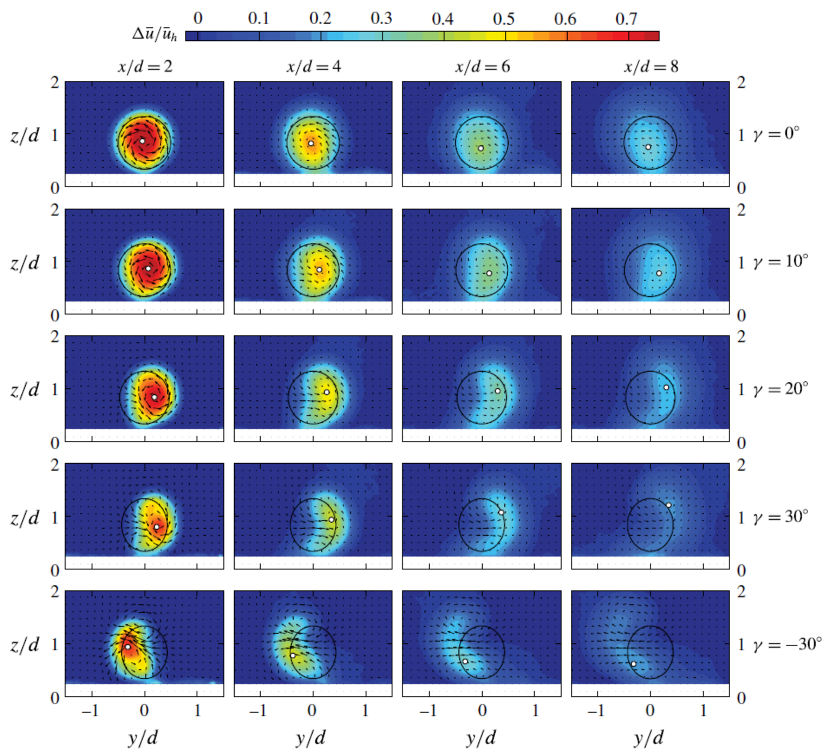

Figure 2.8: Contours of normalized streamwise velocity deficit in yz planes for different yaw angles. Results taken from [5].

Tilt Control

Controlling the tilt angle is considered as another potential strategy for wake redirection. The study conducted by Weipao et. al. [66] showed that tilt angles of 10° and 15° on the upstream turbine increase the total power of the two-turbine setup by 6.9% and 12.0% respectively. Cutler et. al. [13] optimized the tilt angle for maximum Annual Energy Production (AEP) of the Princess Amalia wind farm with 60 NREL 5 MW turbines. A fixed tilt angle increased the power production by 2.77%, but active tilt control lead to a 13.64% increase which was higher than the 7.75% increment of active yaw control. The feasibility of tilt control in wind farms was demonstrated by Annoni et. al. [2] with the help of SOFWA. The LES results indicated 8.3% more power when the turbine tilted towards the ground, causing deflection of wake towards the surface. LES simulation results of tilt control are presented in Figure 2.9 below.

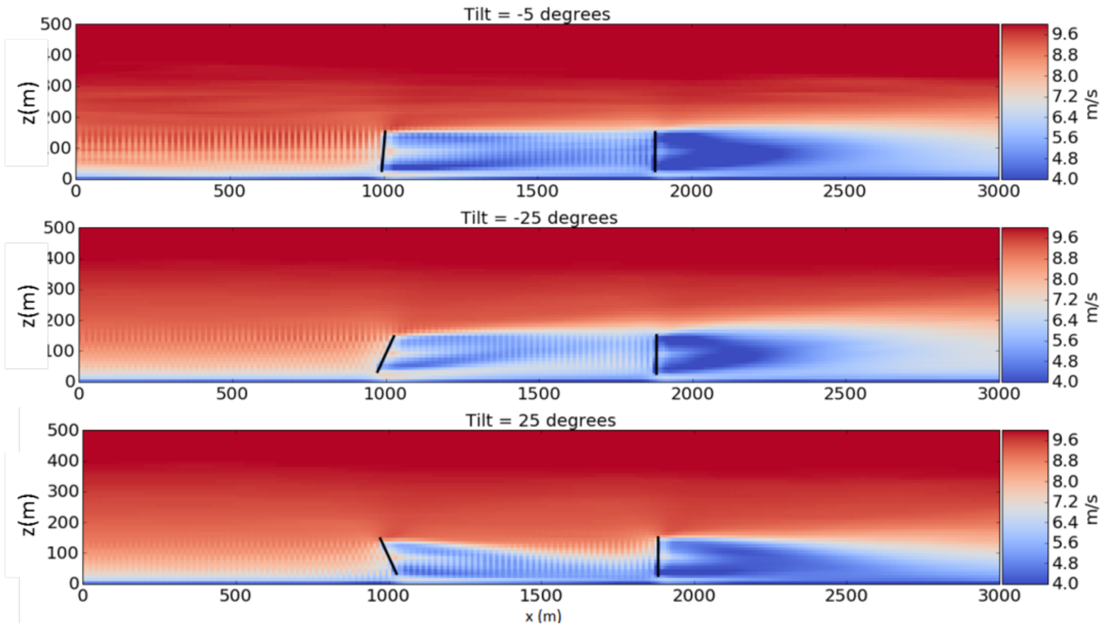

Figure 2.9: LES simulation results of Annoni et. al. [2] for tilt control in wind farm.

2.3. Vertical Axis Wind Turbines

Vertical axis wind turbines (VAWTs) are dated back to 200 BC along the Persian-Afghan borders, used as windmills to grind grains. Having their axis of rotation perpendicular to the wind flow, they worked on the principle of drag force.

In 1931, Darrieus developed the first lift-based VAWT, having oval blade geometry. These curved blades, shaped as Φ, helped to reduce the blade tip effects but possess difficulties in manufacturing. Such issues lead to the decline of the design's popularity [3]. Peter Musgrove invented the variable geometry VAWT in the mid-1970s, which was a modification of the straight blade Darrieus VAWT. The design's unique reefing mechanism to prevent rotor over speeding was later deemed unnecessary due to the passive stalling of aerofoil blades at higher wind speeds. The first H rotor turbine, developed in 1990 with a rated capacity of 500 kW, was short-lived due to a manufacturing error in the fiberglass blade [61]. Also called as straight blade design, it solved most of the problems faced by Φ design and offered a simpler geometry. This design has gained popularity in modern literature as it is easy to manufacture, and can be simulated in 2D CFD [3]. The design also enables the pitching of blades by either a fixed angle or varying the angle using mechanical augmentations, opening new areas and possibilities for research. Later helical or Gorlov VAWTs began to develop, to counter the cyclic torque ripple observed in straight-blade H VAWTs. This design allowed a smoother and more circular torque rose, but the option to vary blade pitch became unavailable, forcing a design choice.

VAWTs have a major advantage that their gearbox and generator are located much lower in their structure, lowering center of mass. This results in ease of access during operation and maintenance, thus reducing the operating cost. The lower center of mass decreases the cost for manufacturing of the foundation and increases compatibility with floating structures. The lower wake length of VAWTs suggests the potential of higher power densities compared to HAWTs when placed in a wind farm, as seen in the study of Rolin and Porte-Agel [51]. To understand the behavior and salient features of the flow of lift-VAWTs, their governing steady and unsteady aerodynamics need to be understood. An in-depth description of them is presented in the following subsections.

2.3.1. VAWT Aerodynamics

A simple way to comprehend the fundamental aerodynamic properties of a lift-driven VAWT is by looking at a 2D blade element. It is to be noted that the theory is taken from De Tavernier's dissertation [15]. The following figure illustrates the top view of a VAWT and will be used to explain the aerodynamics.

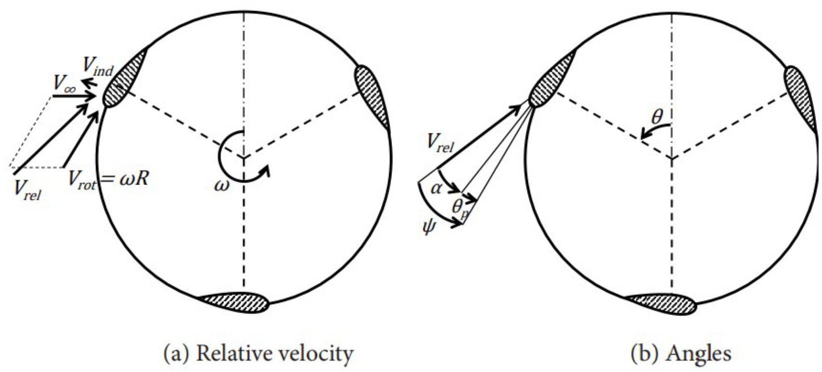

Figure 2.10: Top view illustration of 2D VAWT blade element

The VAWT rotor is defined by its radius R, chord length c, and number of blades B. The Rotational speed of the blades is denoted by angular velocity ω_m, and their length by H. The azimuth angle θ is defined as the angle between crossflow direction and location of the blade, thus ranging from 0°- 180° in the upwind rotor section and 180°- 360° in the downwind rotor section. The inflow angle Ψ is the angle between V_{rel} and tangent to the blade's rotation path. θ_p is the pitch angle of the blade, and α is the angle of attack.

When the turbine rotates, three different velocity components act on the blades. They are the incoming free-stream wind V_∞, rotational velocity V_{rot} which is a product of ω_m and R, and induced velocity V_{ind}, caused by the presence of the force field created by the turbine inside the flow-field. The induced velocity depends upon the thrust coefficient and varies with the turbine's rotation. The relative velocity V_{rel} perceived by the rotating blade can be described as the summation of the three above mentioned velocity components denoted by equation.

$$V_{rel} = V_\infty + V_{rot} + V_{ind} \tag{2.4}$$

Breaking down V_{rel} into X and Y directional components, we get the following two equations

$$V_x = V_\infty + \omega_m R \cdot cos(\theta) + V_{ind,x} \tag{2.5}$$

$$V_y = \omega_m R \cdot sin(\theta) + V_{ind,y} \tag{2.6}$$

These inflow and crossflow components (V_x & V_y) are used to determine the normal and tangential velocity components to the actuator surface, or rotation path of the blade.

$$V_t = V_x \cdot cos(\theta) + V_y \cdot sin(\theta) \tag{2.7}$$

$$V_n = V_x \cdot sin(\theta) - V_y \cdot cos(\theta) \tag{2.8}$$

The angle of attack α is defined as the difference between the pitch angle and inflow angle, while the inflow angle Ψ can be represented using V_t and V_n. This can be observed from the following equations.

$$\alpha = tan^{-1}(V_n/V_t) - \theta_p \tag{2.9}$$

$$\Psi = tan^{-1}(V_n/V_t) \tag{2.10}$$

Implementing the Blade Element Theory, we calculate the lift and drag on a single spanwise blade unit using the equations. As the angle of attack (α) changes with the rotation of the blade, the lift and drag coefficients (C_L and C_D) become functions of α.

$$L_f = \frac{1}{2}\rho V_{rel}^2 \cdot C_L(\alpha) \cdot c \tag{2.11}$$

$$D_f = \frac{1}{2}\rho V_{rel}^2 \cdot C_D(\alpha) \cdot c \tag{2.12}$$

These forces are split into the normal and tangential forces along the blade element as represented in the following equations.

$$F_n = L_f \cdot \text{cos}(\Psi) + D_f \cdot \text{sin}(\Psi) \tag{2.13}$$

$$F_t = L_f \cdot \text{sin}(\Psi) - D_f \cdot \text{cos}(\Psi) \tag{2.14}$$

The average power produced in one revolution is the average tangential force times rotational velocity $\omega_m R$, as defined in the following equation. The thrust of the wind turbine is calculated using the following equation.

$$P = \frac{1}{2\pi}\int_0^{2\pi} B \cdot F_t(\theta) \cdot \omega_m R \cdot d\theta \tag{2.15}$$

$$T = \frac{1}{2\pi}\int_0^{2\pi} B \cdot (F_t(\theta)cos(\theta) - F_n(\theta)sin(\theta)) \cdot d\theta \tag{2.16}$$

Using the above equations, and considering the rotor sweep area of A, we can calculate the thrust coefficient C_T and power coefficient C_P of the turbine.

$$C_T = \frac{T}{0.5 \cdot \rho A V_\infty^2} \tag{2.17}$$

$$C_P = \frac{P}{0.5 \cdot \rho A V_\infty^3} \tag{2.18}$$

The representation of forces acting on the turbine blade are depicted in Figure 2.11 below.

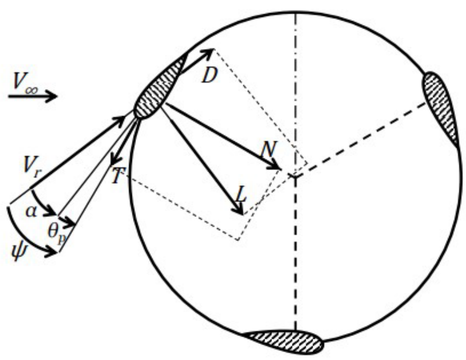

Figure 2.11: Forces acting on VAWT blade

2.3.2. Unsteady Aerodynamics of VAWTs

A couple of unsteady aerodynamic conditions arise from VAWTs, as they experience dynamic loading and variable inflow conditions over their rotation. These phenomena, addressed in the following subsections, are important to comprehend the complex behavior and nature of the wake produced by VAWTs.

Dynamic Stall

This phenomenon is the interaction of flow separation between the leading edge and the trailing edge of an airfoil, as the airfoil experiences variation in pressure distribution and boundary layer development, due to changes in effective inflow direction. During the rotation of a VAWT, the blade experiences the stages of dynamic stall. First, trailing edge separation occurs, causing the shear layer to move towards the leading edge. This leads to the formation of a leading edge vortex, that travels towards the trailing edge. As it finally passes the trailing edge, complete flow separation occurs. Then, the flow reattaches to the surface and aerodynamic loads return to pre-stall values. These stages can be seen in the Figure 2.12 below.

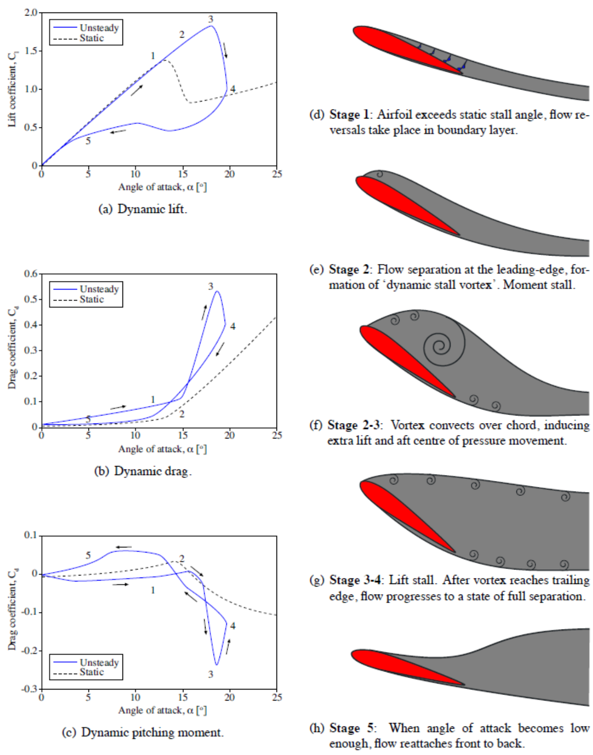

Figure 2.12: The stages of dynamic stall as described by Leishman [40]

Blade-Vortex Interaction

This effect is caused due to the axis of rotation being perpendicular to the airflow, making it a feature of VAWTs. The upwind part of the rotor would experience smooth flow, and shed vortices in the wake, which would be encountered by the downwind rotor section. This leads to oscillations in the angle of attack and loads.

Flow Curvature

The circular rotation of a wind turbine can be broken down into a translation motion and a continuous pitching motion, along the pitching axis. The pitching motion, leading to a varying inflow condition on the blade's airfoil surface, leads to the creation of flow curvature effects. As compensation for the pitching motion, an equivalent angle of attack or camber is added. This would allow the transfer of geometrical airfoil in curvi-linear flow to a virtual airfoil with camber in recti-linear flow.

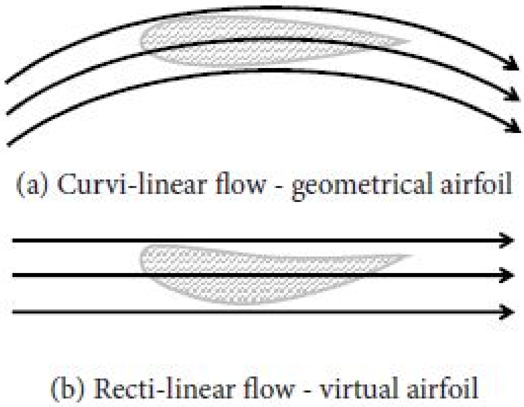

Figure 2.13: Flow Curvature

The above mentioned unsteady aerodynamics of a lift-driven vertical axis wind turbines greatly influence its generated wake. Similar to HAWT, the wake of the VAWT can be divided into near wake and far wake. While studying the near wake of a H-VAWT in dynamic stall, Ferreira [18] describes the formation and shedding of counter-rotating tip vortices that influence the surrounding wake sheet, using Particle Imaging Velocimetry (PIV). Tescione [60] confirms and adds on the influence of the tip vortices on the wake's structure. These vortical structures lead to the vertical contraction of the wake and increase the wake asymmetry as it moves downstream. Enhanced vortex deformation is noted as a result of the tip vortex system, which leads to an earlier vortex breakdown, further leading to a faster recovery of wake, in comparison with HAWTs. The work of Posa et al [50] highlights the effect of tip speed ratio (TSR) on the dynamic stall and size of vortex structures. It is specified that, for higher Reynolds number, TSR is an important parameter to characterise the wake of VAWTs. Another influence on the VAWT wake is the blade geometry. Helical VAWTs with different blade sweep directions and angles were tested and compared with straight blade H-VAWT by Hohman et. al. [27]. The increase in sweep angle leads to a reduction in dynamic stall magnitude, and consequently, a reduction in wake turbulence. However, the findings also showed that straight blade geometry provided the highest momentum deficit in the wake, suggesting maximum generated power.

2.3.3. Wake Control for H-VAWT

Different techniques are applied to introduce lateral forces on VAWTs, aiming to achieve similar wake deflection as HAWTs. The experimental work of LeBlanc and Ferreira [39] indicated that cross-flow loading can be introduced into the flow by pitching the blades of the VAWT. This relation between blade pitching and resulting wake behaviour was studied by Huang et. al. [32] using stereoscopic PIV. The details regarding blade pitching and resulting wake deflection will be discussed in this section.

The work of De Tavernier [15] gives detailed information on these 2D and 3D actuator cylinder models used to represent VAWTs and their wakes. Huang et al. mention the correlation of wake's structure and development, to the force field generated by the wind turbine. The following theory taken from [32], provides the connection between VAWT loading and vorticity structures.

We look at the simplified vorticity equation, generated by a 3D actuator cylinder.

$$\rho \frac{D\omega}{Dt} = \nabla \times \mathbf{f} \tag{2.19}$$

where ρ is density of air, ω is vorticity vector and f is force vector. We apply this equation to a three-dimensional actuator cylinder of diameter D and height H, and rewrite it in cylindrical coordinates.

$$
\begin{aligned}
\rho\frac{D\omega}{Dt} &= \nabla \times \mathbf{f} \\
&= \frac{1}{r}\begin{vmatrix} \hat{e}_r & r\hat{e}_\theta & \hat{e}_z \\ \frac{\partial}{\partial r} & \frac{\partial}{\partial \theta} & \frac{\partial}{\partial z} \\ f_r & rf_\theta & f_z \end{vmatrix} \\
&= \frac{1}{r}\left[\left(\frac{\partial f_z}{\partial \theta} - \frac{\partial (rf_\theta)}{\partial z}\right)\left(-\frac{\partial f_z}{\partial r} + \frac{\partial f_r}{\partial z}\right)\left(\frac{\partial (rf_\theta)}{\partial r} - \frac{\partial f_r}{\partial \theta}\right)\right]\begin{bmatrix} \hat{e}_r \\ r\hat{e}_\theta \\ \hat{e}_z \end{bmatrix}
\end{aligned}
\tag{2.20}
$$

where $\hat{e}_r, r\hat{e}_\theta, \hat{e}_z$ are the unit vectors for the r, θ, and z axes, respectively. Eliminating f_θ and f_z as they equal to zero, we get

$$
\rho\frac{D\omega}{Dt} = \begin{cases} \frac{\partial f_r}{\partial z}\hat{e}_\theta, \text{ for } r = \frac{D}{2}, z = \pm\frac{H}{2} \\ \frac{\partial f_r}{\partial z}\hat{e}_\theta - \frac{1}{r}\frac{\partial f_r}{\partial \theta}\hat{e}_z, \text{ for } r = \frac{D}{2}, |z| \leq \pm\frac{H}{2}, \text{ and } \theta = 90°, 270° \end{cases}
\tag{2.21}
$$

From the above equation, it is evident that the maximum vorticity is created at the top and bottom extreme ends of the cylinder where $z = \pm\frac{H}{2}$, and also along the span for $\theta = 90°$ or $270°$, at the connection points of actuator cylinder's upwind and downwind sections. The representation of this vortex system can be observed in the following figure.

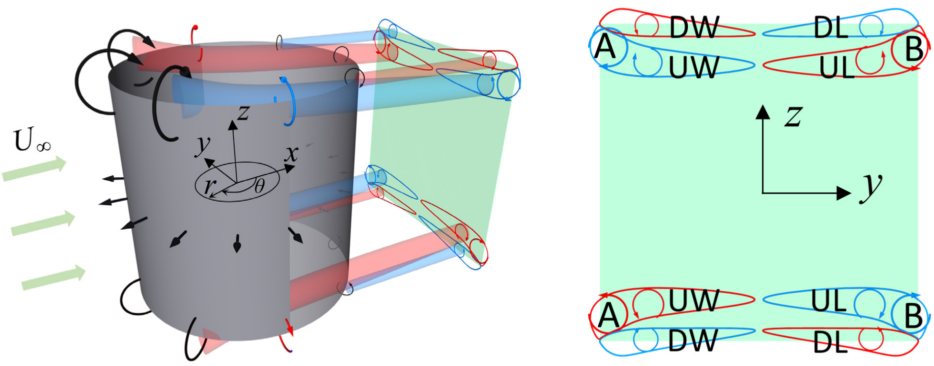

Figure 2.14: 3D actuator cylinder model with trailing vortex system. Figure taken from [32]

The propagation trajectories of streamwise vorticity are depicted by blue and red tubes. The strongest streamwise counter-rotating vortex pairs, marked as A and B, appear in the upwind region of the AC model. These vortex pairs are responsible for the deflection and deformation of the wake. The deformation is in correlation with the induced velocity by streamwise vorticity, which in turn, is the result of loading on the actuator cylinder.

Figure 2.15 depicts the above load cases along with the deformed shape of the wake. The cylinder is divided into four quadrants, upwind windward (UW), upwind leeward (UL), downwind windward (DW), and downwind leeward (DL). The vectors represent normal force.

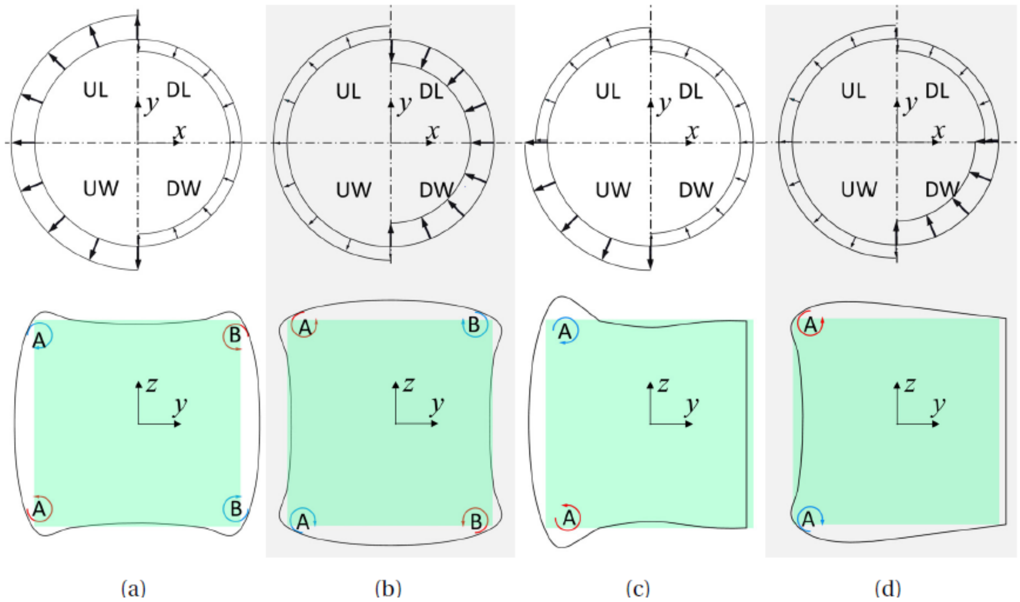

Figure 2.15: Effect of force fields on wake deflection

The initial shape of the wake is similar to the frontal area of a cylinder before deformation occurs. In the absence of lateral forces, expansion of wake laterally is observed for increased loading of the upwind half, whereas vertical expansion of wake corresponds to higher loads on the downwind half of the AC model. These phenomena are illustrated in sub-figures (a) and (b) of Figure 2.15 respectively. For non-zero lateral forces, the wake is deflected towards the windward direction when the upwind windward quadrant load rises, as seen in sub-figure (c). Deflection of wake towards the leeward side is seen when higher loading is present in the downwind windward sector, showcased in sub-figure (d).

Thus, in order to achieve the objective of enhanced vertical flow entrainment, axial expansion of wake is desired. Thus, the forces on the downwind halves of the VAWT rotor need to be amplified. As previously achieved by Huang et. al. in [32], the introduction of lateral forces is executed by changing the blade pitch angle. This variation of AC force field caused by the change in blade pitch is discussed in the following subsection.

2.3.4. Manipulation of forces on VAWTs

The above subsection briefed us about the relation between the force field of the Actuator Cylinder and the strength of vorticity. One of the methods to introduce loads on a H-VAWT is to change the pitch angle of the rotor blades. Pitching the blades towards (positively) and away from (negatively) the axis of rotation produces lateral forces, changing the force field of AC. The normal force distribution is calculated as per the following equation.

$$f_N = \frac{B}{2\pi R}(L_f \cdot \cos(\alpha - \theta_p) + D_f \cdot \sin(\alpha - \theta_p)) \tag{2.22}$$

The illustration of the force fields resulting from the above equation is carried out by Huang [31], and presented in Figure 2.16 below.

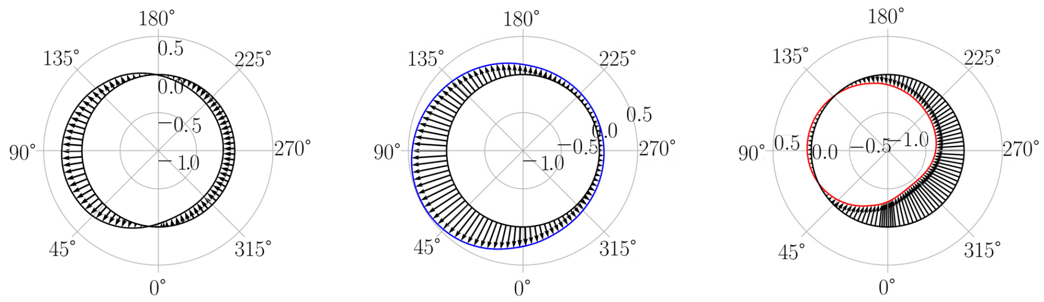

(a) Pitch 0° **(b)** Pitch 10° **(c)** Pitch -10°

Figure 2.16: Distribution of normal force f_N for different pitch cases. Figure adapted from Huang [31]

2.3.5. VAWT Layout Configurations

Unlike horizontal axis wind turbines (HAWTs), vertical axis wind turbines (VAWTs) show an increase in performance when placed close together. Lam and Peng [38] conducted wind tunnel tests for a turbine pair for co-rotating and counter-rotating modes of operation. It was found that the twin turbine arrangement had rapid wake recovery, with small wake expansion and lower tower vibrations. Similar experiment was conducted by Vergaerde et. al. [62] and compared the results with an isolated VAWT, with different tip-speed ratio, rotor solidity σ and inter-turbine distance. The comparison of normalized streamwise velocity at different heights, between isolated and paired VAWTs is presented in Figure 2.17.

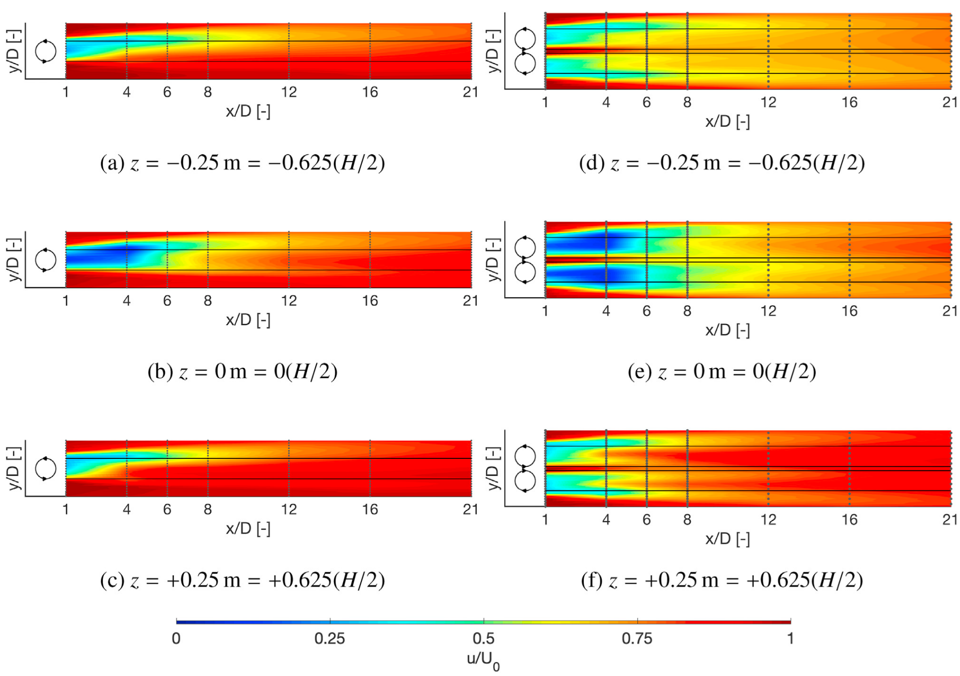

Figure 2.17: Normalized streamwise velocity at different heights, for isolated VAWT(left) and pair of VAWTs (right). Figure adapted from [62].

The VAWT pairs were put in a farm alignment and an experimental field study was conducted by Kinzel et. al. [35]. It indicated that 95% flow recovery behind pairs of counter-rotating VAWTs was achieved at a distance of 6D, while the HAWTs require a 14D distance to achieve the same. This study was furthered into a 3-VAWT cluster by Hezaveh et. al. [26], where actuator line model (ALM) was implemented in a large-eddy simulation (LES) to utilize the interactions between closely-spaced VAWTs, for optimizing the VAWT farm layouts, seen in Figure 2.18. The staggered-triangle cluster arrangement of turbines demonstrated a higher average wind farm power coefficient C_P, and the lowest cost per unit power produced.

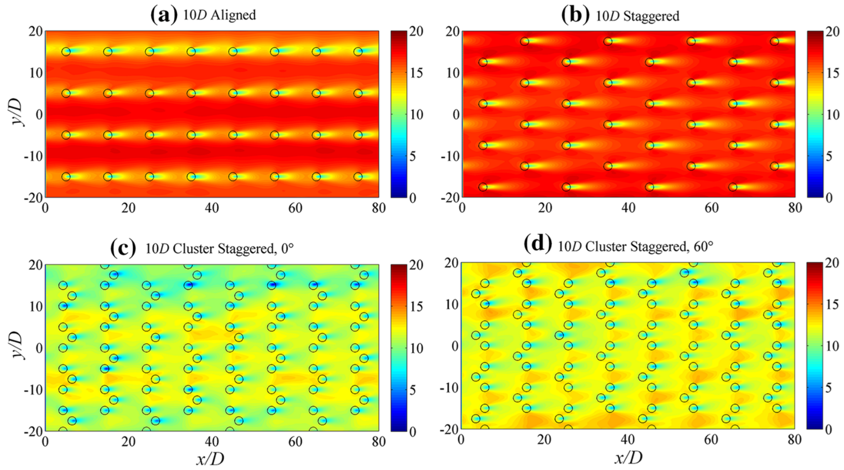

Figure 2.18: LES results of streamwise velocity magnitude by Hezaveh et. al. [26] for different wind farm layouts.

The studies presented thus far provide evidence that VAWTs show increased power output for lower use of area, when spaced closely in a staggered array layout.

2.4. Experimental Techniques

While performing experiments, the relevant models must be scaled in order to capture the physical attributes of interest correctly. It is a common practice to match the non dimensional parameters or coefficients of full-scale structures, as re-creating real world conditions is difficult. According to Edgar Buckingham, a scaled model shows similarity in behavior of the original structure, if the non-dimensional parameters are matched. This is called the Buckingham-Pi theorem. These non-dimensional parameters vary according to the physical attribute, and matching every parameter is difficult. Hence, a choice needs to be made while designing the experiment, regarding which attributes are to be acquired, and thus understand the relevant non-dimensional parameters which need to be matched.

2.4.1. Scaling Laws for Wind Turbines

Up-scaling laws for HAWTs have been developed over the past years, but there has been limited research conducted on down-scaled wind turbine models, developed for wind tunnel testing.
Detailed laws for scaling down wind turbines are formulated in the work of Canet et. al. [11]. There, the rotor characteristics have been given importance, and two strategies are proposed, namely straightforward zooming down, and aero-structural redesign. Three scaled-down models are compared to the DTU 10MW wind turbine, where the previously mentioned strategies are applied.
It is found that the Strouhal number is associated with vortex shedding, which is a phenomenon having significant relevance in wake behavior. This number can be equalized between scaled and full-scale models when the TSR is kept the same between the two models. Even if the absolute value of parameters are not matched, the scaled models can be employed to understand and capture the relevant trends.
The thrust coefficient of a wind turbine is important to characterize its wake deficit which represents the wake structure, and the scaled model should ideally match the coefficient for realistic aerodynamic performance.

Scaling of wind turbines to match the wake characteristics has been prioritized in the work of Wang et al. [65], where the LES-ALM hybrid approach was utilized. Although the LES-ALM code was first verified with measurements performed in a wind tunnel with the TUM G1 scaled wind turbine, it was unable to remove uncertainty. This uncertainty, pertaining to the near-wake inner core, was attributed to the difference in the swirl, rotational augmentation, inboard circulation, and nacelle geometry.
But looking at the bigger picture, the far wake and the near wake showed similarities to the full-scale turbine metrics of wake deficit, shear stresses, turbulence intensity, and others, and no significant

alteration in wake behavior was observed due to the uncertainties.

It is thus understood that to closely match the wake properties of real-world turbines, vortex shedding needs to be matched, based on the Strouhal number. This can be achieved by operating the scaled model at the same tip speed ratio (TSR) of the original structure.

2.4.2. Particle Tracking Velocimetry

Particle Tracking Velocimetry (PTV), closely related to Particle Image Velocimetry (PIV), is a non-intrusive measurement technique that quantifies the displacement of small tracer particles in a flowing fluid. While both methods (PTV and PIV) are employed for the common objective of determining the velocity of particles, PIV identifies the mean displacement of a group of particles, whereas PTV tracks the paths of every individual particle in 3D space.

A PIV/PTV setup comprises of a seeding system, illumination system and recording system. The seeding system injects small tracer particles in the flow of a fluid without disrupting its inherent flow conditions. These tracer particles are illuminated and are recorded using high-speed cameras, by the illumination and recording systems respectively. Based on the number of cameras in the recording system, PIV is classified into three types, Planar PIV, Stereoscopic PIV, and Tomographic PIV. Representation of tomographic PIV is done in the following Figure 2.19 below.

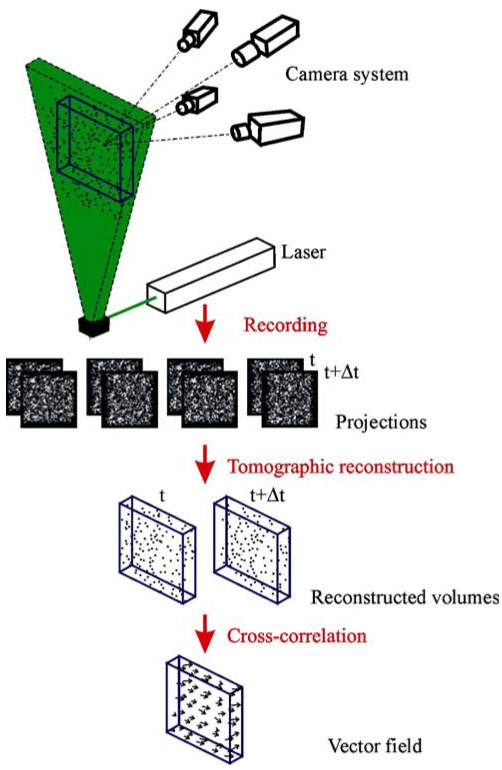

Figure 2.19: Representation of principle behind tomographic PIV. Figure taken from [17]

In Planar PIV, a single camera is utilized, which measures 2 velocity components in a 2D area. Stereoscopic PIV has two cameras, placed at an angle to the measuring area of interest, that record 3 velocity components in the 2D area. Tomographic PIV employs three or more cameras that reconstruct the 3D measurement domain and measure 3 velocity components in the 3D region. Figure 2.20 shows the schematic of tomographic PTV with HFSBs as seeding particles, presented in the work of Schneiders et. al. [54].

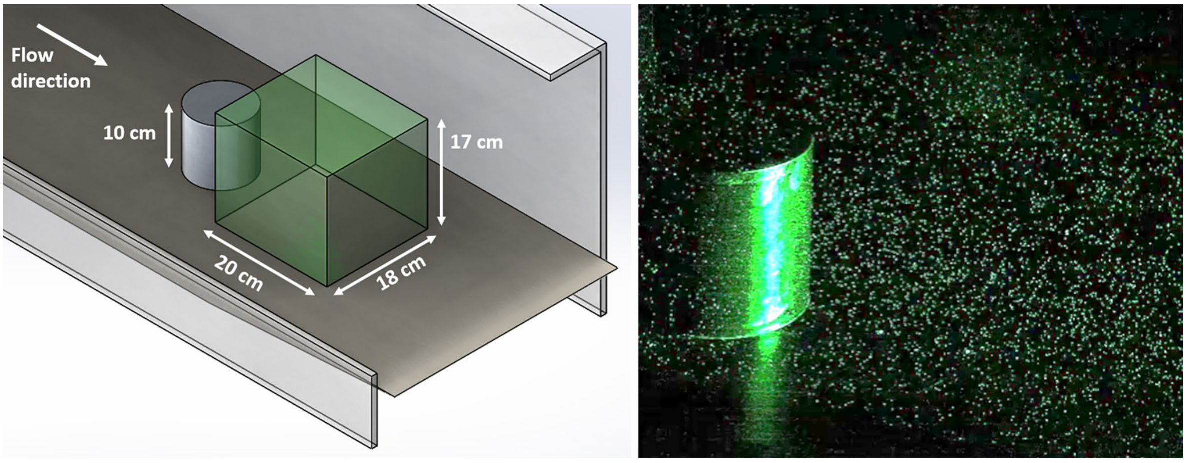

Figure 2.20: Schematic of Tomographic PTV with HFSB, taken from [54].

The analysis of these images, acquired by the high-speed camera setup, is done digitally with the assistance of software. Multiple techniques and algorithms were developed for processing the images like Stereo Matching proposed by Guezennec et. al. [23], or Kitzhofer and Brücker's Short Particle Tracks Exclusion [36]. Shake-the-Box method, an advance technique introduced by Schanz et. al.[53] relies on temporal data and tracks from earlier time steps and anticipates the future particle positions. This prediction is then rearranged and re-positioned multiple times, dubbed as "shaken", till a suitable triangulation match occurs.

2.5. Research Objectives

The preceding sections of this introductory chapter have given a brief idea about the details of wind energy and the aerodynamics of wind turbines. This section aims to summarise the key findings from the provided synthesis of the literature and address the research gap. The research objective will be formulated based on the gap, and supporting research questions will be addressed.

- Targets have been set by the governing bodies to produce renewable energy from offshore wind farms in the North Sea, but are difficult to achieve.
- The ABL profile transforms into the IWFBL profile inside a large wind farm, where the re-energizing of the wind's kinetic energy is dominated by vertical momentum transfer.
- Optimisation of wind farm yield has been thoroughly researched by understanding wake steering methods and wake re-energizing techniques. The wake of a wind turbine can be deflected by imposing a lateral force on the flow, achieved by yawing the HAWT.
- Vertical Axis Wind Turbines have a faster wake recovery, as a result of counter-rotating tip vortices. By changing the pitch angle of the blades of a VAWT, the loading changes and results in increased vorticity.
- Past literature has concluded VAWT wakes to be significantly smaller than their HAWT counterpart. Placing VAWTs in close proximity has shown to increase the power production, compared to isolated turbines.

From the above summary, it can be said that there is scope to further the existing research on VAWTs. First and foremost, limited wake measurements have been done for isolated VAWTs in high-density wind farm grids. Secondly, the re-energization of flow inside a VAWT wind farm is not studied. The effects of blade pitching on wake deflection were studied for two turbine configurations, but no information is present when deflection of wake is executed for VAWTs in a wind farm configuration. Due to this lack of research, another area of interest is the recovery of wind power inside such a wind farm. Thus, the following research questions will be addressed in this thesis.

- How does the flow behave within a high-density VAWT wind farm?
- How can we achieve flow re-energization in a VAWT farm?
  - What is the driving mechanism behind the re-energization of the flow?
  - What is the effect of wake deflection on energy entrainment?
  - What changes can be observed in the wake topology inside the wind farm?
  - How do the two modes of flow re-energization affect the available wind power within the wind farm?

To gain a clear understanding of the impact of flow re-energization in a VAWT wind farm and answer the above questions, flow entrainment will be enhanced by changing the blade pitch angle of turbine rotors. The following flowchart in Figure 2.21 provides the approach taken in this thesis.

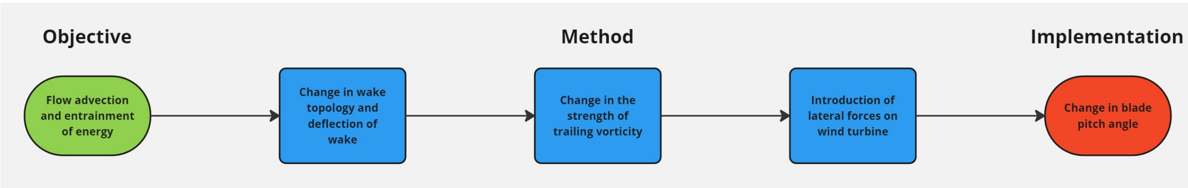

Figure 2.21: Approach taken to achieve enhanced kinetic energy entrainment

By changing the blade pitch angle, lateral forces will be introduced on the wind turbine. These forces will affect the trailing vorticity systems described by the AC theory, which are responsible for wake topology and deflection. Thus, the wake will cause lateral and axial entrainment of momentum from surrounding regions, causing re-energization of the flow. Other methods to achieve entrainment of flow are by tilting the rotors, introducing inclinations in the blade, changing the strut angles, or attaching high lift wings on the tower.

The above approach of changing the blade pitch angle is implemented in the experiment campaign, whose details are presented in the upcoming chapter.

3
Methodology

For this thesis, a quantitative experimental methodology was applied to understand the aerodynamics of a VAWT wind farm, and two campaigns were conducted. Preliminary tests were executed in the first campaign, and the primary experiment was conducted in the second. This chapter briefs the reader on the experiment's apparatus and the details of both experiment campaigns.

3.1. Experiment Apparatus

This section gives detailed description about important equipment used in both the experiments, which includes the designs of turbine model and load balance.

3.1.1. H-VAWT Model

The H-VAWT model used for these campaigns is based on Huang's design, seen in [30], which is designed in-house having rotor dimensions $300mm$ x $300mm$ (span x height). The rotor blades have NACA0012 airfoil, and are supported with struts at a distance of $75mm$ from blade tips. The $1100mm$ long rotor shaft with diameter of $10mm$ is placed inside an aluminium tower housing of length $700mm$ and coupled with two bearings at top and bottom openings. This provides additional stability to the rotating shaft, and increases accuracy of measuring forces. The tower is attached to the VAWT stand, constructed from aluminium extrusions and steel plates. The schematic of turbine can be seen in Figure 3.1 and the detailed specifications are summarized in Table 3.1.

A separate steel plate is manufactured that allows the connection of the VAWT stand and clamps, enabling the rotor units to be attached to the wind farm frame. The VAWTs are driven using Maxon EC motors of rating 260W and controlled with ESCON 50/5 servo controller unit. Bellows couplings are used for the connection, as they help to dampen the vibrations caused by any existing misalignment between turbine and motor shafts. Pitching of the VAWT blades was achieved by connecting fixed pitch adapters between the blades and struts. These $30mm$ long adapters are 3D printed for 0°, $\pm5°$ and $\pm10°$ angles, such that one edge is flat and other matches the NACA0012 geometry, as seen in Figure 3.2. A positive pitch angle indicates pitching inwards to the rotation axis, and negative angle states outwards pitching.

Table 3.1: VAWT Design

Turbine Specifications	
Property	Value
Number of blades	2
Blade profile	NACA0012
Blade length	300 mm
Blade chord	30 mm
Rotor diameter	300 mm
Strut width	30 mm
Tower height	700 mm
Shaft length	1100 mm

Driver Specifications	
Component	Details
Motor	Maxon EC 260 W
Speed	$191 - 764$ RPM
Controller	ESCON 50/5 Servo
Power Supply	Dual Channel $0 - 30V$ DC
Software	LabView, ESCON Studio

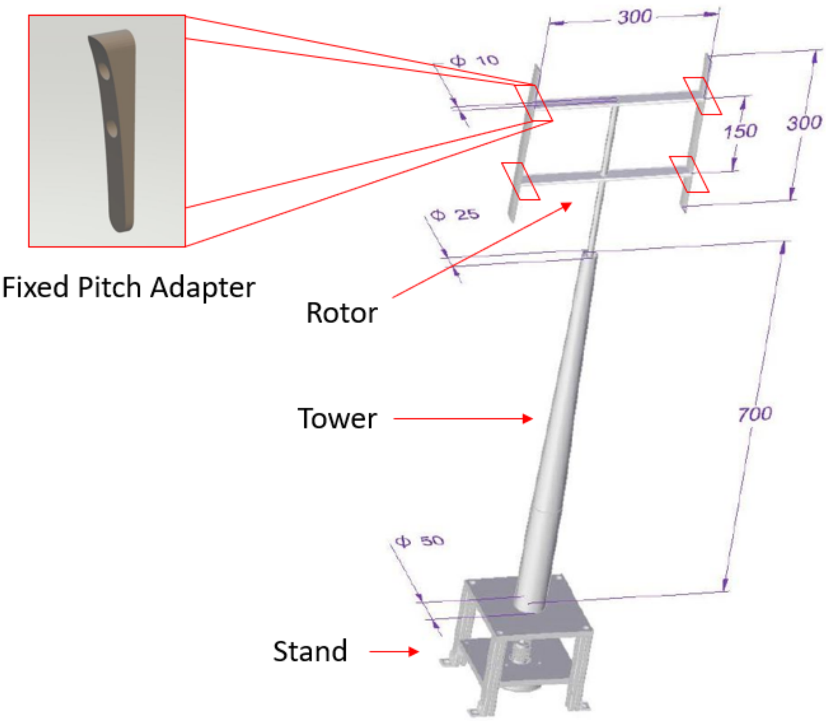

Figure 3.1: Schematic representation of H-VAWT

(a) 0° **(b)** 5° **(c)** -5° **(d)** 10° **(e)** -10°

Figure 3.2: Pitch Adapters

3.1.2. Load Balance

A custom made load balance, as seen in Figure 3.3, was used to measure both the streamwise and lateral forces of the turbine. The load cells used are KD40s type, having a maximum range of ± 50N and maximum error of 0.1%. Detailed information can be found in the work of Huang et. al.[32]. The balance is covered with a plywood box when load measurements are taken. A 3D printed tower cover is screwed to the wooden box in order to transfer loads on the tower to the plywood box, thus removing tower drag from the acquired force measurements.

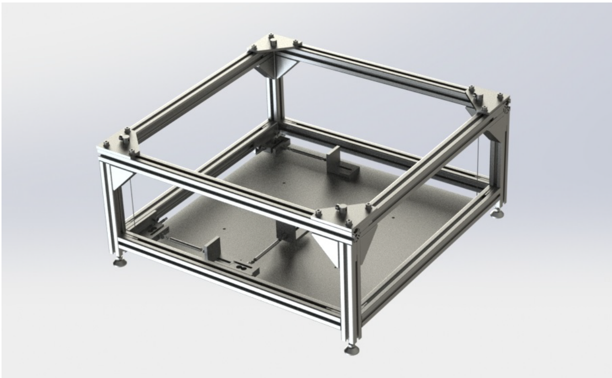

Figure 3.3: Load Balance

3.2. Preliminary Tests Experiment Campaign

The objective of this campaign was to perform load measurements on a single turbine for varying pitch angles of 0°, $\pm 5°$ and $\pm 10°$. From this data, the thrust coefficient vs tip speed ratio plot ($C_T \ vs \ TSR$) was made which finalized the operating TSR of the wind farm for the primary experiment campaign. The secondary objective of the experiment was to perform smoke visualisations for the pitch cases, to estimate the axial displacement of wake.

3.2.1. Setup Details

This campaign was carried out in the W-tunnel of TU Delft's HSL building, a low-speed open-jet wind tunnel having exit cross-section of 0.6m × 0.6m. The load balance described in subsection 3.1.2 was utilised for measuring forces. The balance was connected to NI modules housed within a CompactDAQ chassis, that powers the load cells and enables measurement. LabView software was used to simplify the data acquisition and management processes.

A black background with 50 x 50 mm grid served as the backdrop for the smoke visualizations. The smoke probe was fastened on a steel X beam structure, with its tip aligned at the windward blade tip, facing streamwise direction. This setup can be observed in Figure 3.4a . The camera specifications used for the visualizations are mentioned in Table 3.2 below.

Table 3.2: Camera and Imaging Specifications

Property	Value
Camera	Canon EOS 4000D
Lens	18-55mm
Shutter speed	1/640 sec
F-stop	f/3.5
ISO	3200

3.2.2. Measurements

Measurements and visualizations were carried out at free stream velocity of U_∞ = 3m/s and Reynolds number $Re = 0.6 \times 10^5$. Loads were acquired for TSRs from 1 to 4, where the TSR was set using ESCON Studio software. The blades were then removed to attach new pitch adapters and the process was repeated for all angles.

The smoke visualizations were performed for TSRs from 2.6 to 3.8 with increments of 0.2. The arrangement of cameras can be seen in Figure 3.4b, where camera 1 facing the +Y (lateral) direction measures the axial displacement and camera 2 facing the -X (streamwise) directions captures the lateral displacement. 5 images were taken in continuous mode for each TSR before changing the pitch adapters.

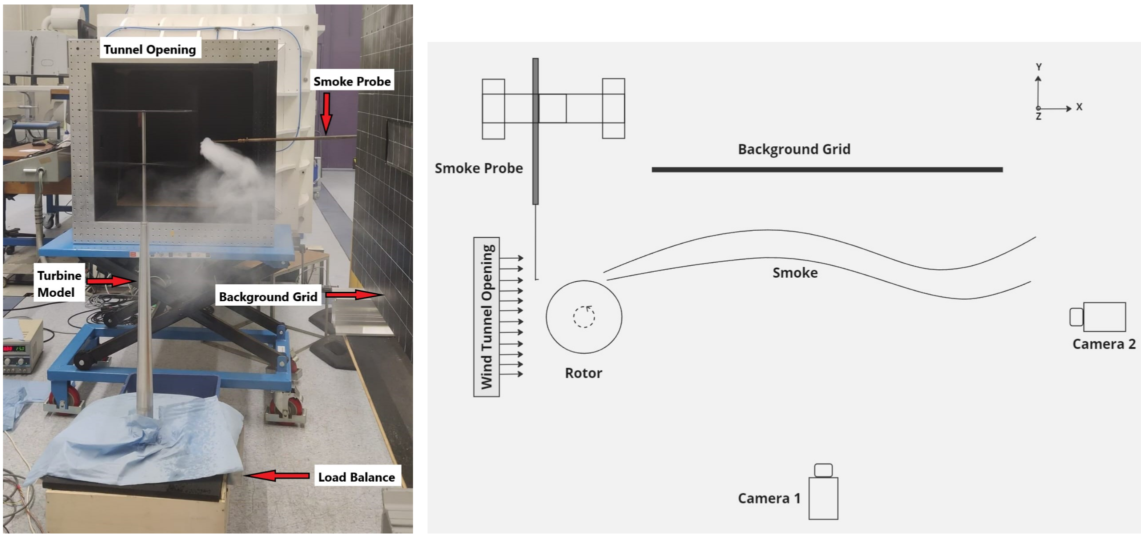

(a) Experiment setup front view **(b)** Top view schematic with visualization volumes

Figure 3.4: Preliminary Tests Experiment Setup

Table 3.3: Overview of measurements

	Pitch Angle	Tip Speed Ratio
Load Measurements	0°	1-4
	5°	1-4
	-5°	1-4
	10°	1-4
	-10°	1-4
Smoke Visualization	0°	2.6-3.8
	10°	2.6-3.8
	-10°	2.6-3.8

The results of this experimental campaign can be found in section 4.1. The following section pertains to the second experiment campaign performed for this thesis, which addresses the primary research objectives of this study.

3.3. Primary Experiment Campaign

This is the principal campaign where the flow inside a H-VAWT wind farm was measured. Along with the flow measurement, the drop in thrust inside the wind farm was measured using similar load measurement techniques mentioned previously in section 3.2. This section provides description about the wind tunnel, wind farm layout, PTV setup, measurement cases and post processing of acquired data.

3.3.1. Wind Tunnel

The wind tunnel experiment was conducted in the Open Jet Facility of HSL. It has an octagonal opening of 2.85 x $2.85m^2$. The tunnel features a contraction ratio of 3:1 and a turbulence intensity of 0.5% up to 1m from the nozzle[42].However, the work of Jux [34] states that the presence of seeding rake inside the settling chamber increases the turbulence intensity to 1.9%. The 500kW fan of the facility is able to produce wind flow velocities in the 0-35 m/s range. For the duration of this campaign, the wind speed was fixed at 3 m/s.

3.3.2. Wind farm layout

A scaled down VAWT wind farm was constructed for this experiment. The base frame of the wind farm was assembled using steel X beams and clamps as seen in Figure 3.5. Dimensions of this frame are $3m$ x $2m$ x $1m$. Steel plates were screwed at the bottom of the supporting $1m$ beams for extra stability. Nine H-VAWT models, described in subsection 3.1.1, are mounted on the frame with lateral spacing of 3.175D and streamwise spacing of 5D.

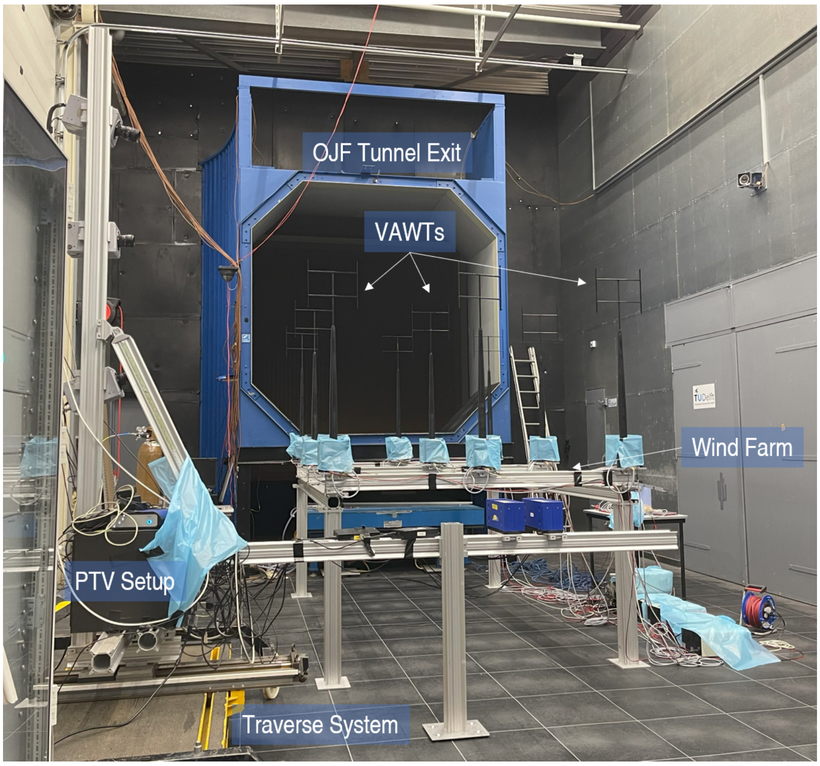

Figure 3.5: Structure of VAWT Farm

The flow inside this wind farm was measured by assembling a PTV setup, which is described in the upcoming subsection.

3.3.3. PTV Setup

To measure the flow inside the VAWT wind farm, Particle Tracking Velocimetry (PTV) technique was utilized. The three key components of this technique are tracer particles, illumination equipment and imaging equipment. The details regarding them will be covered in the following subsections.

Geometry

The geometry of the PTV system was complex due to the nature of the farm model and measurement locations. Cameras were mounted on a vertical 3m beam at different heights, and were angled to capture the rotor, along with the area above it. Details about their placement can be found in Table 3.4, where camera 2 is considered as reference. To prevent the interference of acquisition system with data measurement, the LEDs were mounted on a horizontal 3m X-beam that passed under the wind farm. This L shaped structure was supported with additional beams and was attached to a traversing system, placed besides the wind farm. The traversing system was employed to accurately move the setup, because only a small sub-volume could be measured with the PTV system. This traverse system has a range of 1.5m x 1m with a precision of 1mm, whose movement is controlled using LabView program.

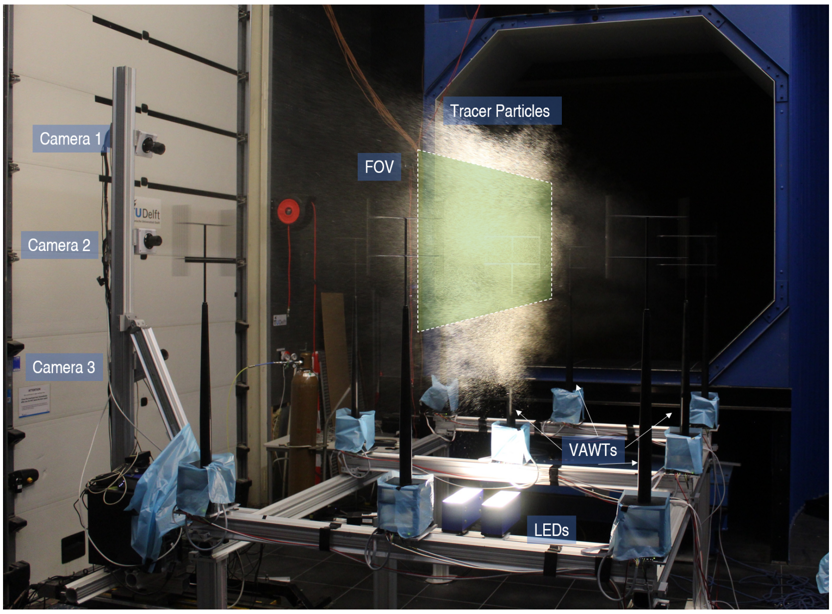

Figure 3.6: Setup of PTV system. Main components of sthe setup are labelled. FOV is visualized as green region.

Optics, Illumination and Timer

Three Photron high-speed cameras were used for imaging the flow field. The model used was FAST-CAM SA1.1, with sensor size of 1 MegaPixel and pixel pitch of 20μm. The camera setup records a 500 mm x 700 mm x 600 mm volume (streamwise x axial x lateral). Two LaVision LED Flashlight 300 were used to get the desired illuminated volume. The cameras and LEDs were synchronized using LaVision's Programmable Timer Unit (PTU-X) and DaVis 10.2 software. The acquisition equipment is connected to the PTU, which is controlled by DaVis, running on a PC.

Table 3.4: PTV System

Component	Parameter	Value
Camera 1 (C1)	Height	+ 540mm
	Angle	-17°
	Lens	60mm
	F-stop	f/22
Camera 2 (C2)	Height	0mm
	Angle	0°
	Lens	50mm
	F-stop	f/22
Camera 3 (C3)	Height	- 740mm
	Angle	20°
	Lens	60mm
	F-stop	f/22
LEDs	Distance	1700mm

Seeding

Neutrally buoyant helium filled soap bubbles(HFSB) are used as tracer particles for the experiment. The seeding rake is placed inside the wind tunnel's contraction nozzle, in the settling area, and the flow of bubbles is controlled by the Fluid Supply Unit (FSU). The rake has a height of 2m and width of 1m, with 15 wings divided in two groups of 7 and 8 wings. Each wing has 27 nozzles that produce helium soap bubbles with median diameter of $300\mu m$ [52]. The seeding area further reduces due to the contraction ratio of OJF's nozzle to 1.15m by 0.57m, seeding only a part of the area of interest. Thus, the seeding rake is also traversed laterally along with the PTV system, ensuring adequate amount of tracer particles in the FOV. Following images show the seeding rake and the HFSB seeding in the flow.

Figure 3.7: PTV Seeding system with seeding rake (left) and HFSB seeded flowstream (right)

3.3.4. PTV Acquisition Details

The following Table 3.5 summarizes the settings used to capture the flow of the wind farm.

Table 3.5: Imaging Details

Parameter	Property	Value
Imaging	Camera exposure time	$250\mu s$
	Light source pulse duration	$200\mu s$
	Imaging rate	500 Hz
	Acquisition volume	500 x 700 x 600 mm
	Number of Images	4600
	Duration	9.2 sec
Seeding	Tracer Particles	HFSBs
	Soap pressure	2 bar
	Air pressure	1.8 bar
	Helium pressure	1.8 bar
Wind Tunnel	Wind speed	2.98-3.03 m/s

3.3.5. Measurement Cases

Thrust Measurement

The force measurements were taken for the central column of turbines to understand the reduction of thrust as we go inside the farm. Necessary changes in the turbine's height were made in order to keep all turbines at the same level. It is to be noted that the streamwise spacing for the load measurements between two rows of VAWTs was 4.84D, and the Reynolds number Re was 0.6×10^5. A larger steel plate was manufactured to accommodate the load balances on the wind farm frame, similar to the small connecting plates for VAWTs. Table 3.6 shows the force measurement cases performed for calculating the reduction in thrust force at different operating TSRs.
Loads for a single turbine were measured first and compared directly with the results of preliminary tests conducted beforehand, for all 3 pitch angles. Then the loads for the central column of the wind farm were measured similarly.

Table 3.6: Overview of load measurements

Configuration	Pitch Angle	Tip Speed Ratio
	0°	1-4.5
Single Turbine	10°	1-4.5
	-10°	1-4.5
	0°	3, 3.5, 4
Wind farm	10°	3, 3.5, 4
	-10°	3, 3.5, 4

Flow Measurement

Before measuring the flow of the wind farm model, the streamwise spacing between the rows was increased to 5D. Using the PTV setup, four regions of interest were acquired. These are marked with red dashed lines in Figure 3.8a. The red dot represents the geometric center of the first row central rotor, and marks the origin (0,0,0) of the wind farm coordinate system. As the range of the traversing system was not enough to cover the entirety of wind farm, it was manually moved downstream to capture the regions of interest. In total, the 129 volumes measured in this experiment are represented as green trapezoids, in Figure 3.8 below.

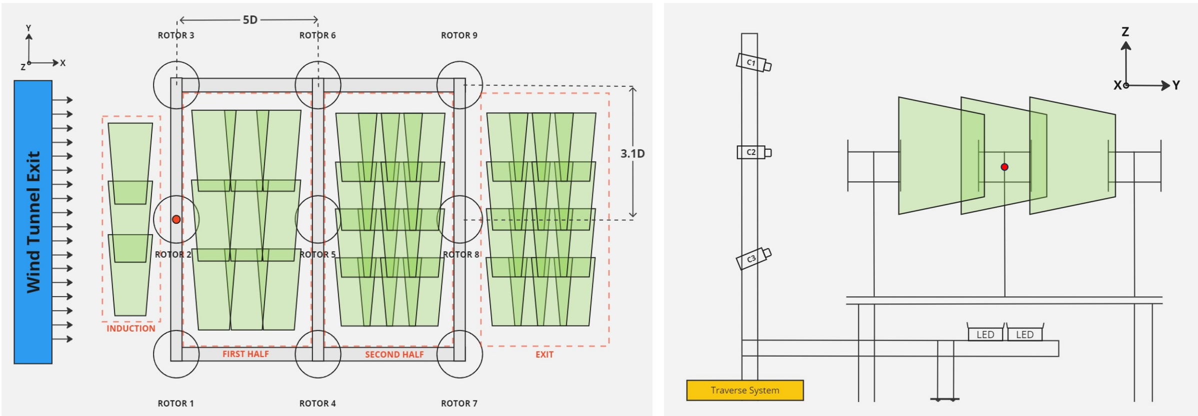

(a) Top View of Measurement volume locations

(b) Front view of volume locations

Figure 3.8: Schematic representation of measurement volumes represented in green. Red dot shows the origin.

Table 3.7 below gives an overview of the flow measurement volumes. The induction region of the wind farm was measured at the second row after removing the first row turbines. The X and Y positions represent the streamwise and lateral distances traversed with respect to the starting position (0 mm), for each measurement location. This origin, for each wind farm region, is around 1 rotor diameter (1D) away from the central VAWT.

Table 3.7: Overview of PTV Measurement Volumes

Location	Pitch Angles (°)	X Positions (mm)	Y Positions (mm)
			-350
Wind Farm Induction Region	0°, 10°, -10°	-360	0
			350
			-450
		0	0
			500
			-450
Wind Farm First Half	0°, 10°, -10°	400	0
			500
			-450
		800	0
			500
			-450
		-100	-150
			150
			450
			-450
		300	-150
			150
Wind Farm Second Half	0°, 10°, -10°		450
			-450
		700	-150
			150
			450
			-450
		1000	-150
			150
			450
			-450
		0	-150
			150
			450
			-450
		400	-150
			150
Wind Farm Exit Region	0°, 10°, -10°		450
			-450
		800	-150
			150
			450
			-450
		1200	-150
			150
			450

From the above table, we see that the PTV setup was moved to different positions to acquire the desired data. Hence, it was necessary to come up with a method to accurately track the measurement volumes with respect to the wind farm. This method is explained in the next subsection.

3.3.6. Mapping Wind Farm in Global Frame of Refernce

To map the volume locations in the wind farm, a calibration stick was fabricated by marking equidistant points on a steel L beam. This stick was placed on the top strut of the VAWTs within the FOV of the PTV system, and the zero marking was aligned with the centre of the shaft. Images of the stick were taken by the PTV setup. After applying the required geometric masking to isolate the markings, 3D-IPR function was used to capture the dots within the acquisition FOV. This method allows us to know the location of measured volumes in the reference frame of wind farm during post processing. Images of this process are shown below in Figure 3.9.

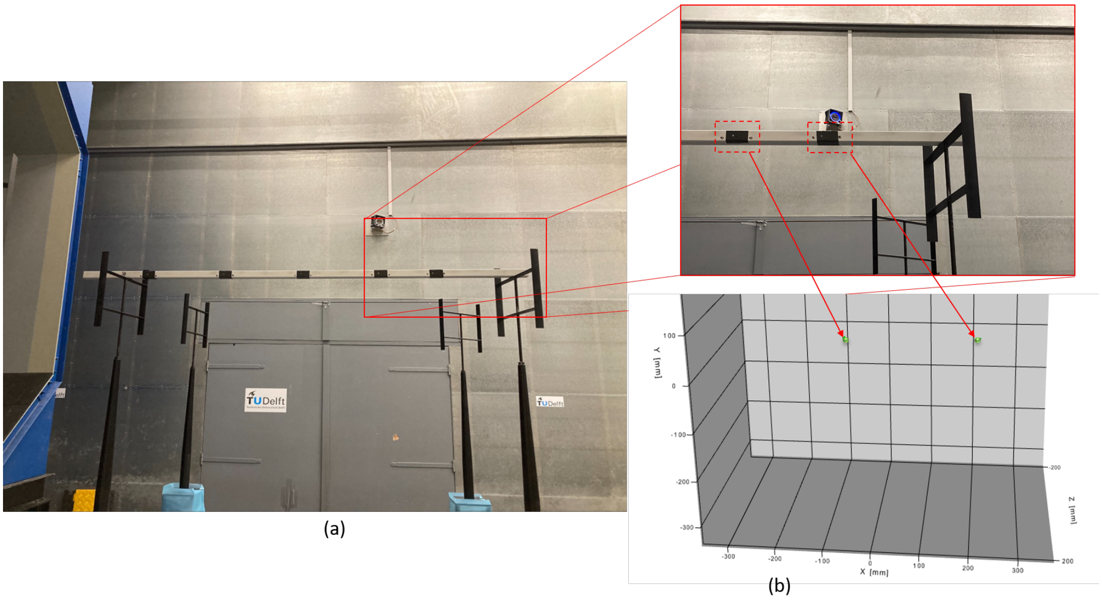

Figure 3.9: Determining the location of wind farm. (a) Setup of calibration stick in between two rows. (b) Identifying marks within the virtual 3D volume.

3.4. Data Post Processing

Before analysing the acquired data from load balances or PTV system, a few processing steps are performed. These are discussed in the following subsections.

3.4.1. Thrust Coefficient Calculation

The instantaneous force readings from the load balance are obtained and stored using LabVIEW software. The data format is converted and averaged over 10 seconds to get the mean forces in streamwise and lateral directions. From the mean streamwise force, the thrust coefficient is calculated using the following equation.

$$C_T = \frac{T}{1/2 \cdot \rho A U^2} \tag{3.1}$$

where

1. T - Thrust
2. ρ - Density of air
3. A - Rotor area
4. U - Wind speed

3.4.2. PTV Data Processing

The processing of PTV data is performed in steps which are sequentially explained in this subsection.

PTV System Calibration

The geometric calibration was performed to define the measurement volume acquired by the PTV system. It was executed using the DaVis 10 software, by correlating images taken of a calibration plate at different lateral distances.

In the following stage, known as volumetric self calibration, pictures of the tracer particles are taken and DaVis examines their motions. This process requires manual adjustments and multiple re-iterations to get a low average disparity, and is crucial since it establishes the PTV data accuracy. Using the above data, the optical transfer function is determined, which allows the software to reconstruct tracer particles from camera images into 3D volume.

Shake The Box

Shake-the-Box algorithm, an advance technique introduced by Schanz et. al.[53], relies on temporal data and tracks from earlier time step images, and anticipates future particle positions. This prediction is then rearranged and re-positioned multiple times, dubbed as ”shaken”, till a suitable triangulation match occurs with the next image. Before the algorithm is applied, the time averaged minimum intensity is filtered using the Subtract Time Filter function, with a filter length of 5 images. This removes the unwanted background light and noise. The details of STB are mentioned in the following Table 3.8.

Table 3.8: Shake the box settings

Volume	X	-250.0mm to 254.7mm
	Y	-348.26mm to 342.21mm
	Z	-604.16 to 0.0mm
Particles	Multi-passes	1
	Detection threshold	70-80 counts
	Triangulation error	1.0-1.5 voxel
Tracking Details	Vx	$1.51 \pm 3.02 m/s$
	Vy	$0 \pm 3.43 m/s$
	Vz	$0 \pm 3.43 m/s$

Stitching the Volumes

As previously indicated, in order to generate the whole volume of interest for a particular pitch angle, multiple volumes were obtained owing to the size of the wind farm model and the restricted size of the seeding rake. These discrete smaller reconstructed volumes from the STB process are shifted and merged to form a single large volume that encompasses the whole region of interest. Davis 10 has a built-in function that accomplishes this.

Binning

The binning operation is performed on the merged STB volumes to acquire the flow data of particles. The stitched volume is divided into sub-volumes of 128x128x128 voxels or 20x20x20 mm with a 75% overlap, where data from all particles within a sub-volume is averaged and stored. The resulting vector resolution from the above settings is 0.052 vectors per mm. This process is represented in Figure 3.10.

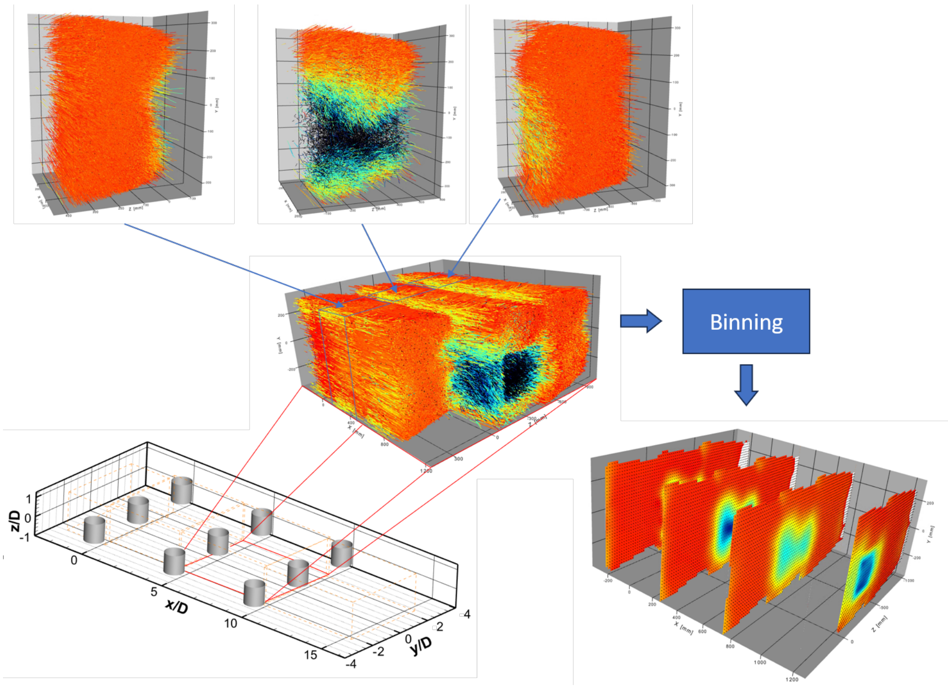

Figure 3.10: Representation of the stitching and binning steps of PTV data.

3.5. Wake Data Analysis

3.5.1. Available Power Calculation

The available wind power (AP) is governed by the cube of wind velocity. As different blade pitch angles of a VAWT lead to different wake topologies, the available power within the wind farm will show variation. For it's analysis, the cube of normalized streamwise velocity $(Ux/U\infty)^3$ will be integrated and averaged over the frontal area of a hypothetical downwind turbine, a method implemented by Huang [32]. The calculation is performed by Equation 3.2 presented below

$$f_{AP}(x_0, y_0, z_0) = \begin{cases} \iint_A Ux^3(x_0, y, z)/U_\infty^3 \, dy \, dz / A \\ A : |y| \leq 0.5D, |z| \leq 0.5H \end{cases} \tag{3.2}$$

where

1. f_{AP} - AP coefficient
2. (x_0, y_0, z_0) - centre coordinates of hypothetical downwind VAWT
3. A - Rotor area
4. $Ux/U\infty$ - normalized streamwise wind velocity
5. D - Rotor diameter
6. H - Rotor height

The schematic of this method is presented in Figure 3.11. There, the contour plots of $(Ux/U\infty)^3$ at a specific x/D distances are taken, and the integration region within the volume cross-section is presented as a black square. This represents the front area of a hypothetical VAWT, with its centre as origin (0,0).

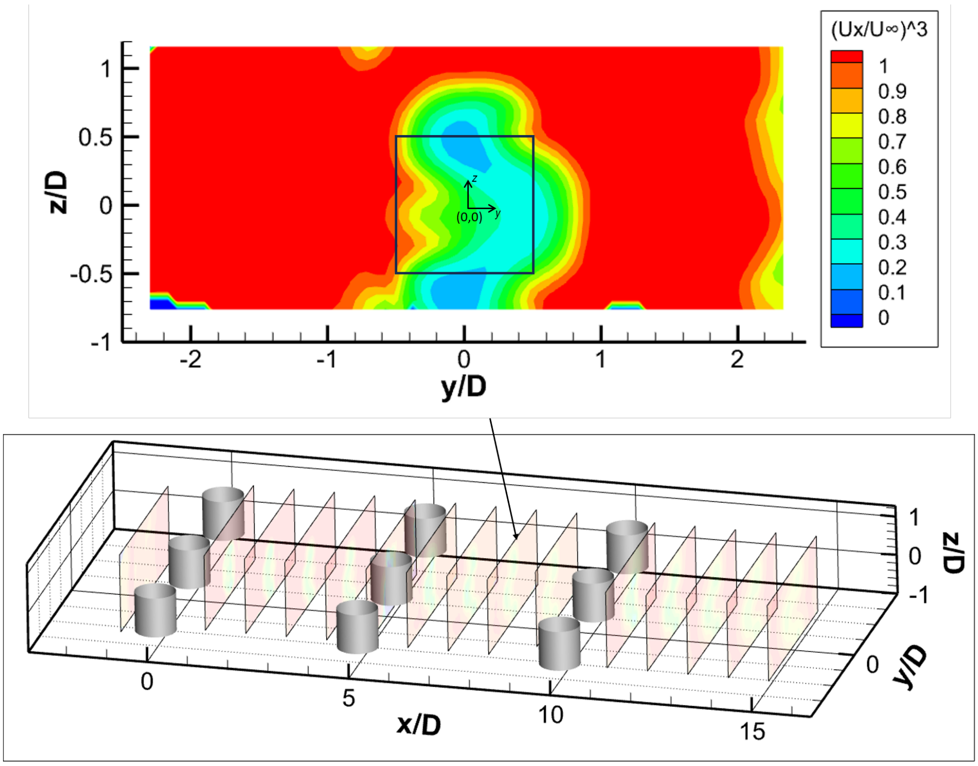

Figure 3.11: AP coefficient calculation. Integration area is represented by black square over $(Ux/U\infty)^3$ contour plot.

3.5.2. Streamwise momentum budget

The analysis of streamwise momentum budget begins with re-arranging the Reynolds-averaged Navier-Stokes (RANS) equation in the streamwise direction, as presented in Equation 3.3. The streamwise advection term is kept on the LHS and the other terms contributing to the momentum recovery are present on the RHS. Due to high rotor diameter based Reynolds number, the viscous terms of the equation can be neglected (Re = 0.6×10^5)

$$\underbrace{\bar{u}\frac{\partial \bar{u}}{\partial x} = -\bar{v}\frac{\partial \bar{u}}{\partial y} - \bar{w}\frac{\partial \bar{u}}{\partial z}}_{\text{advection}} \underbrace{-\frac{1}{\rho}\frac{\partial \bar{p}}{\partial x}}_{\text{pressure}} \underbrace{-\frac{\partial \overline{u'u'}}{\partial x} - \frac{\partial \overline{u'v'}}{\partial y} - \frac{\partial \overline{u'w'}}{\partial z}}_{\text{Reynolds stresses}} \tag{3.3}$$

The above equation is re-arranged to look at the contribution of in-plane advection and Reynolds stress terms on the wake recovery rate, and is further normalized by multiplying both sides by $\frac{D}{U_\infty}$. This process has been implemented earlier by Boudreau and Dumans[7], Huang et. al. [32], and Bossuyt et. al. [6], and resulting equation is presented below, as Equation 3.4. As, the pressure is not measured during the experiments, its analysis will be skipped.

$$\frac{D}{U_\infty} \cdot \frac{\partial \bar{u}}{\partial x} = \frac{1}{\bar{u}}\left(-\bar{v}\frac{\partial \bar{u}}{\partial y} - \bar{w}\frac{\partial \bar{u}}{\partial z} - \frac{1}{\rho}\frac{\partial \bar{p}}{\partial x} - \frac{\partial \overline{u'u'}}{\partial x} - \frac{\partial \overline{u'v'}}{\partial y} - \frac{\partial \overline{u'w'}}{\partial z}\right) \cdot \frac{D}{U_\infty} \tag{3.4}$$

Similar to the Available Wind Power calculation, analysis of the budget terms will be done at multiple x/D locations. The terms will be averaged over the projected frontal area of the rotor.

4
Results and Discussion

This chapter showcases the results obtained from the experiment campaigns described previously, in the methodology chapter. The results presented in this report will describe the efficiency of the wind farm model, and its aerodynamics.

4.1. Preliminary Test Results

Before the primary experiment of the wind farm was conducted, the wind turbine model was tested in the W tunnel. The load measurements and smoke visualizations of the model for pitched blade angles are presented in this section.

4.1.1. Load Measurements

The lateral and streamwise forces of the turbine model were measured for blade pitch angles of 0°, $\pm 5°$ and $\pm 10°$. From those measured values, the time-averaged thrust coefficients in streamwise (C_{Tx}) and lateral (C_{Ty}) directions were computed and plotted against tip speed ratio (λ). Figure 4.1 shows the C_{Tx} vs TSR plots for the pitch angles of $\pm 5°$ and $\pm 10°$.

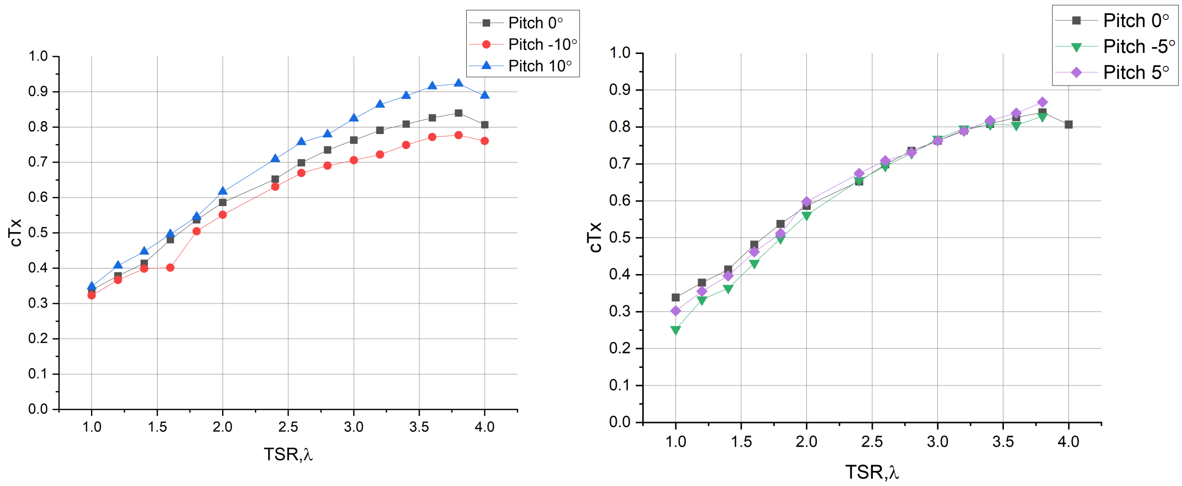

Figure 4.1: Streamwise Thrust Coefficent vs TSR (C_{Tx} vs λ) for $\pm 10°$(left) and $\pm 5°$(right) pitch angles.

The thrust coefficient displays an increasing trend as the tip speed ratio increases. Pitching the blades positively indicates an increase in performance of the wind turbine model. When pitch angle is varied by $\pm 10°$, we observe that the difference in thrust coefficients is higher at higher TSRs, and lower at lower TSRs. This trend is opposite for lower pitch angle of $\pm 5°$.

Figure 4.2 depicts the C_{Ty} vs TSR plots for $\pm 5^\circ$ and $\pm 10^\circ$ pitch angles. Positive values represent forces in the -Y direction and negative values towards the +Y direction (see Figure 3.4b).

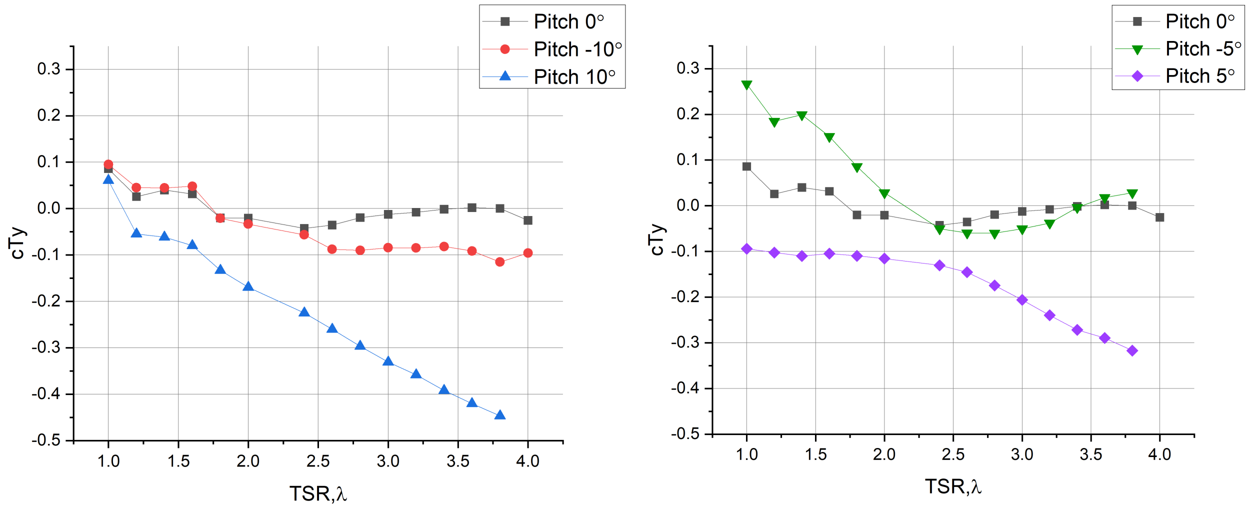

Figure 4.2: Lateral Thrust Coefficent vs TSR for $\pm 10^\circ$(left) and $\pm 5^\circ$(right) pitch angles.

We see the lateral trust increasing towards the +Y direction as the TSR increases, for both +5° and +10° pitch cases. However, for +5° pitch case, this rising trend starts later, after TSR of 2.5. The lateral loading seen in positive pitch case is consistent with the theoretical loading plot discussed in the literature.

For -10° case, the forces act in the -Y direction for TSRs lower than 1.6, and then switch to the opposite direction. A similar trend is observed for -5° pitch angle, but for TSRs 3.5 and up, the lateral forces become positive, indicating forces along -Y direction.

The behaviour of lateral thrust coefficient for baseline case is almost identical to the -10° pitch case, for TSRs below 2.5. Afterwards, the value becomes closer to zero.

4.1.2. Smoke Visualizations

The smoke visualization was performed at the windward side top edge of blade, for pitch angles of 0°, +10° and -10°, to check the feasibility of wake deflection by blade pitching. The following figures show the front and side views of smoke, for a TSR of 3.4.

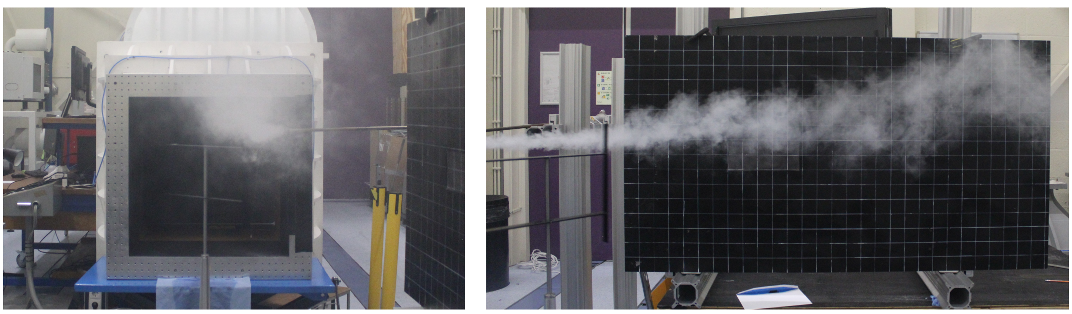

(a) Image from Camera 2 **(b)** Image from Camera 1

Figure 4.3: Pitch -10°

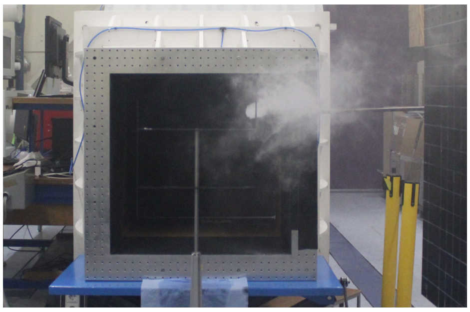

(a) Image from Camera 2

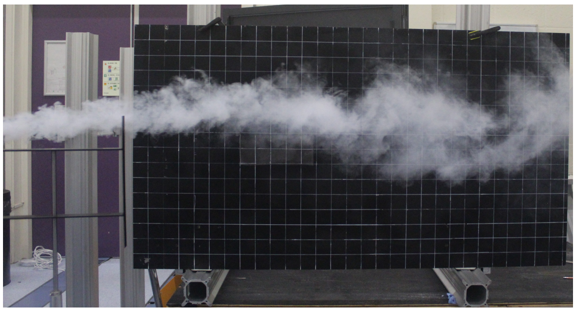

(b) Image from Camera 1

Figure 4.4: Pitch 0°

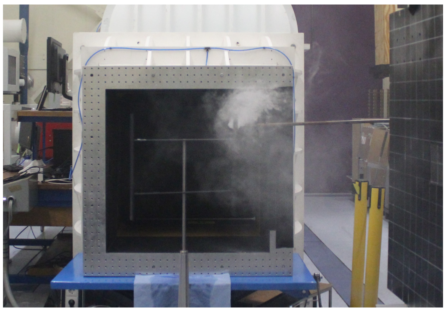

(a) Image from Camera 2

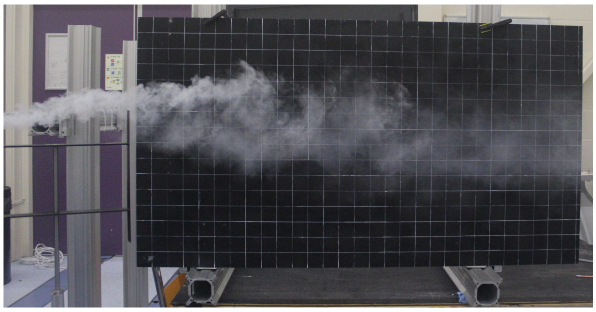

(b) Image from Camera 1

Figure 4.5: Pitch +10°

The visual results helped to give an estimated deflection of the wake in the lateral and axial directions. The path of the smoke was traced using MATLAB functions, and a seventh degree polynomial fit was employed to map the axial displacement. Figure 4.6 shows the tracing implemented on the images. The marks in red indicate pixels with values higher than the set threshold value. The black line indicates the polynomial fit based on the red marks.

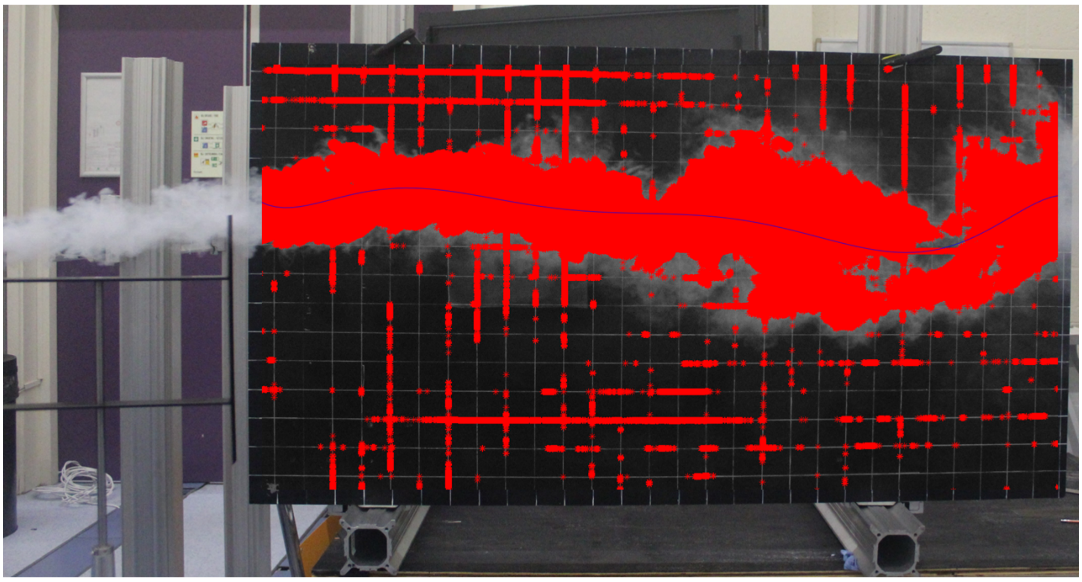

Figure 4.6: Example of smoke path tracing. Points in red indicate high-intensity particles. Black curve represents smoke movement.

Using the above method, the deflection of smoke for different pitch angles was analysed and compared in Figure 4.7. The curve in blue represents the baseline case of no pitch angle. The red curve represented by '+' markers indicates the smoke deflection for +10° pitch angle, and the -10° pitch case smoke movement is plotted with green ' * ' markers.

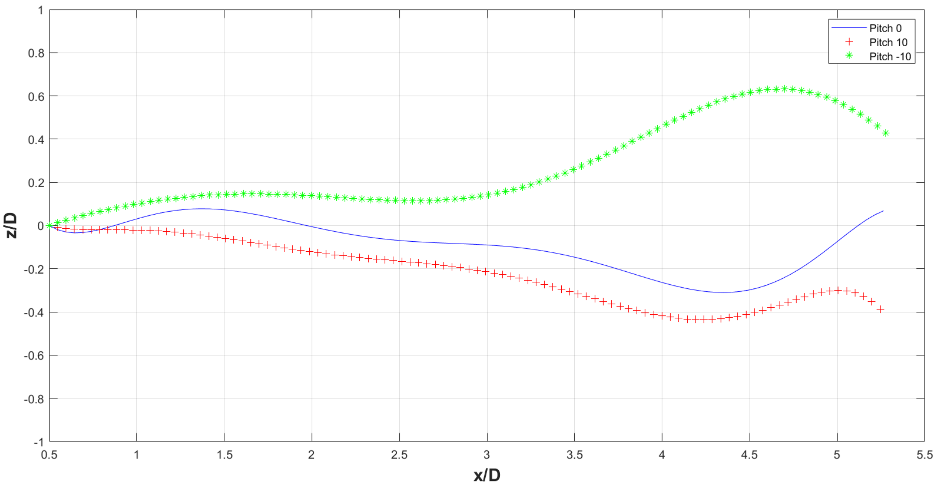

Figure 4.7: Axial displacement of smoke.

A reasonable proof of concept for creating wake deflection through pitch angle modification is provided by the analysis of the polynomial curves. It is clear that highest axial displacement of smoke is produced by pitching the blades negatively, that is away from the axis of rotation. This result reflects on the previously discussed literature, where axial expansion of wake occurs for loading in downwind half, which was observed for -10° pitch angle. On the other hand, the 0° pitch and +10° pitch angles show movement in the -z direction, and trace a similar path.

The preliminary test results provided helpful insight on the behaviour of the H-VAWT model in different pitch cases. The important outcomes are listed below

- From the smoke visualization analysis, it was conclude that pitching rotor blades by $\pm$ 10° causes noticeable deflection of the wake. Thus, the blades will be pitched by 10° in the primary experiment.
- As the target streamwise thrust coefficient (C_{Tx}) was 0.8, it was decided that the turbines in wind farm configuration would rotate at a Tip Speed Ratio (TSR) of 3.5. From this point further, all results are presented for this TSR.

This concludes the results of the preliminary tests. The results of the primary experiment of this thesis are presented in the following section.

4.2. Primary Experiment Campaign Results

4.2.1. Load Data Analysis

Figure 4.8 characterizes the efficiency of the turbines within the wind farm. This is executed by comparing the thrust coefficients of second and third row turbines with the first row turbine, which receives free stream airflow. These coefficients are presented in Table 4.1. It is to be noted that the load data is obtained only for the central turbines of each row.

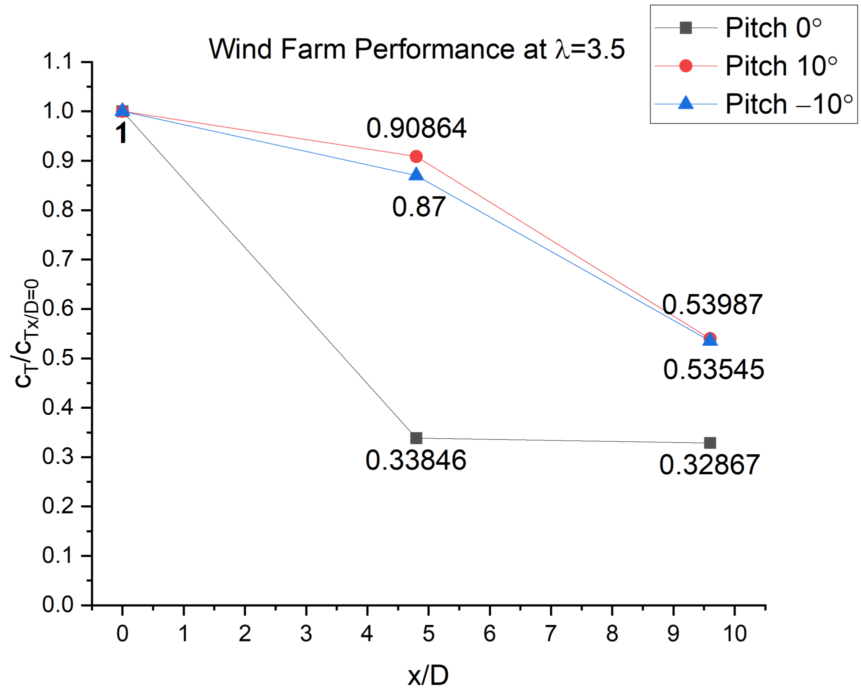

Figure 4.8: Comparison of thrust coefficients of turbines in the wind farm.

Table 4.1: Computed thrust coefficients for different pitch cases

Pitch Angle	Rotor 1 C_{Tx}	Rotor 2 C_{Tx}	Rotor 3 C_{Tx}
0°	0.555	0.188	0.182
10°	0.822	0.747	0.444
-10°	0.495	0.373	0.229

Comparing the thrust coefficients of first rotor with the isolated turbine tested in the preliminary campaign, we observe a significant decrease. This could be linked to the induction of the wind farm, but detailed analysis is required. Unlike 0° and -10° cases, the reduction of C_{Tx} for +10° case is lower. For the baseline case of pitch 0°, the performance of second row turbine drops to 33.8%, and the last row turbine performs at 32.8% capacity. When pitch angle is set to 10°, the second row turbine operates at an efficiency of 90.8%, and the last one's efficiency reaches 53.9% The performance trend of the turbines when blade pitch angle is set to -10° is similar to the case of +10° pitch angle. The second and third turbines are 87% and 53.5% efficient, respectively, as the first turbine which receives free-stream flow.
We can see the greatest loss in performance is for the zero pitch setting. Pitch angle of +10° has the least reduction of efficiency for row 2 VAWT, but then reaches the same value as -10° for row 3. The loss of thrust in between rows 2 and 3 might be the cause of lateral wake expansion of row 2 VAWTs caused by positive pitch angle.

From the above streamwise thrust coefficients, 1D actuator disk theory was implemented to calculate the induction factor 'a', and the power coefficients C_P. These computed power coefficients are presented in Table 4.2 below.

Table 4.2: Computed power coefficients for different pitch cases

Pitch Angle	Rotor 1 C_P	Rotor 2 C_P	Rotor 3 C_P
0°	0.4626	0.1786	0.1733
10°	0.5843	0.5613	0.3873
-10°	0.4232	0.3339	0.2148

The computed power coefficients were used to calculate the theoretical power produced by the wind turbines, by assuming a constant inflow wind speed of 3m/s, and a constant TSR. The power density of the wind farm for different pitch cases was further computed, by considering streamwise spacing of 4.8D and lateral spacing of 3.1D. Table 4.3 presents the power densities and the percentage change compared to the baseline case of 0° pitch.

Table 4.3: Computed power density for different pitch cases

Pitch Case	Rotor 1 P_D $[W/m^2]$	Rotor 2 P_D $[W/m^2]$	Rotor 3 P_D $[W/m^2]$	Average P_D $[W/m^2]$
0°	0.5128	0.1979	0.1921	0.3009
10°	0.6477(+26.3%)	0.6222(+214.4%)	0.4293(+123.4%)	0.5664 (+88.23%)
-10°	0.4619(-9.9%)	0.3701(+87.0%)	0.2381(+23.9%)	0.3591 (+19.34%)

The +10° pitch case shows an average increase of 88.23% in power density, while the -10° pitch case has a +19.34% increase in power density. These values are significantly higher than the observed change after yaw control implementation in HAWT wind farms. For comparison, results from Fleming et. al. [21] showed 7.7% increase after implementation of yaw control. The highest percentage increase occurs for the central rotor 2, with 214% rise for inwards blade pitching, and 87% for outwards.

4.2.2. PTV Data Validation

Pitching the blades of a H-VAWT lead to unique wake structures. A direct comparison with the wake deflection results from the work of Huang et. al. [32] is showcased in Figure 4.9. The plots are divided in two sections at z/D = 0 which is the axis of symmetry, as surface is absent. The top half shows data acquired behind the central turbine of the first row of the wind farm, and the bottom half represents data from Huang. The rotor sweep area is represented with a black square. It is to be noted that the wind turbine operates at a TSR of 2.5 in Huang's experiment, while the TSR of wind farm's turbines is 3.5.

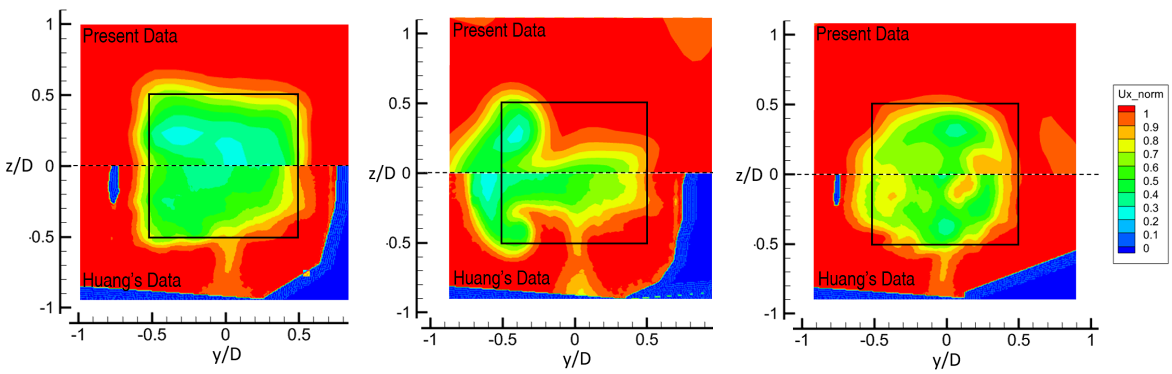

(a) Pitch 0° **(b)** Pitch 10° **(c)** Pitch -10°

Figure 4.9: Comparison of streamwise velocity profiles at distance x/D = 1. Top half represents present data, and bottom half represents data from Huang et. al. [32].

Similarities between the wake profiles for all three blade pitch settings can be observed, but a perfect match between the plots is not present. Since the turbines in wind farm operate at a higher TSR, the lateral thrust induced for +10° pitch angle case is larger and the wake is deflected further. As this lateral force does not have a significant impact for baseline case and negative pitch case, a large mismatch in wake perimeter is not observed. The measured thrust coefficients in Huang's experiment for 2.5 TSR were 0.65, 0.81 and 0.60 for pitch cases of 0°, 10° and -10° respectively, while the coefficients measured in current experiment are 0.55, 0.82 and 0.49 for TSR of 3.5.

4.2.3. Streamwise Vorticity

The flow of the wind farm is dictated by the formation, strength and movement of vortices, created by the VAWTs. The streamwise vorticity is presented in this subsection.

Pitch 0°

Figure 4.10 depicts the normalized streamwise vorticity of the wind farm for the baseline case, where pitching of blades is absent. Iso-surfaces represented in red are drawn for value $\omega_x \cdot D/U_\infty = 0.5$, and blue colored iso-surfaces indicate $\omega_x \cdot D/U_\infty = -0.5$ magnitude. Three slices are made, 1D distance away from each row of turbines, and the vorticity contours within those planes are presented in detail. The in-plane velocity flow is portrayed using vectors, and the rotor area is marked by the grey rectangles.

The vorticity ω_x is normalized by multiplying it with rotor diameter D and dividing by free stream velocity U_∞, a method commonly observed in literature ([32],[51]).

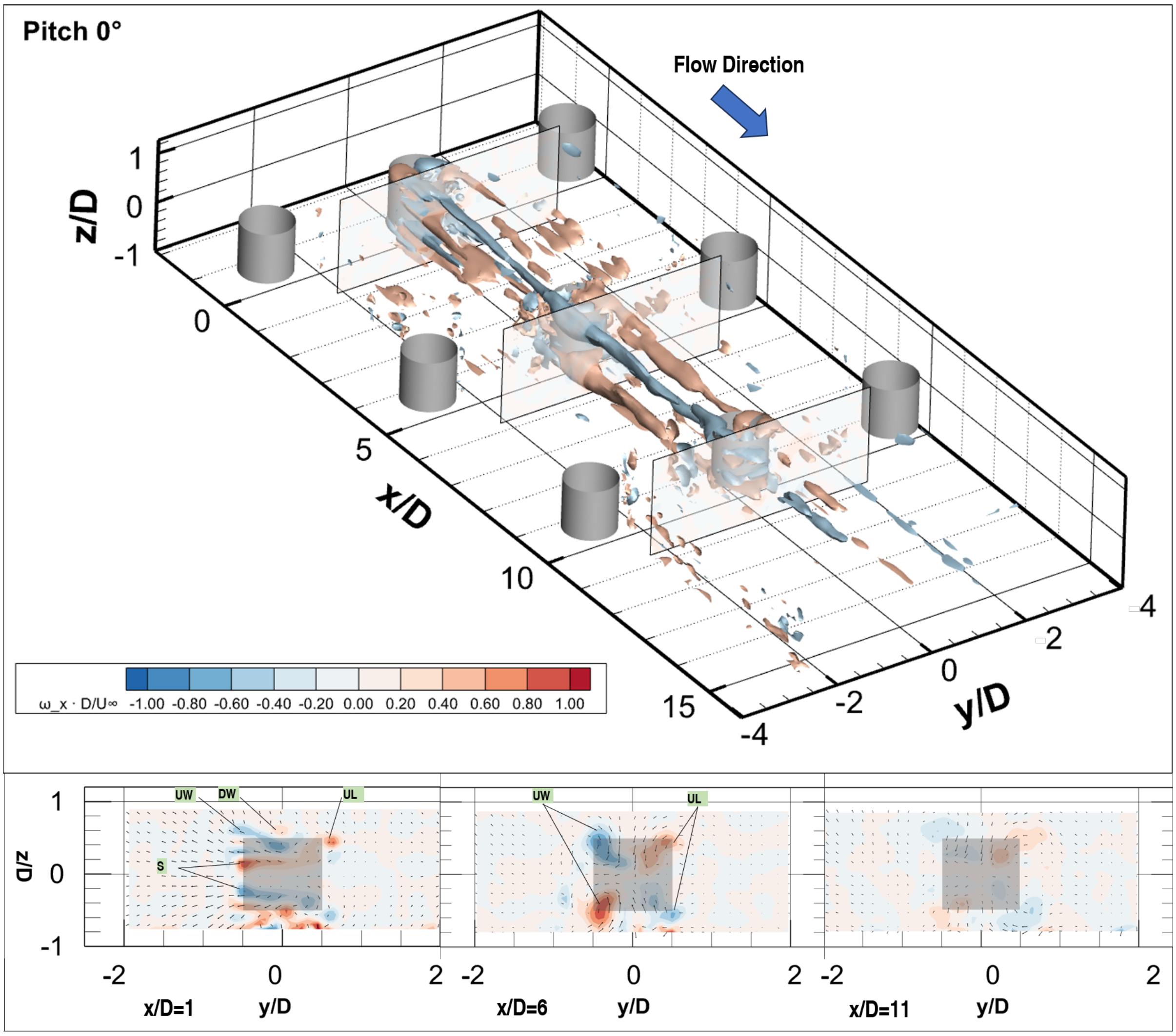

Figure 4.10: Normalized streamwise vorticity for 0° pitch angle. Flow moves in the +x direction. Iso-surfaces are drawn at values of $\omega_x \cdot D/U_\infty = \pm 0.5$. Slices are taken at x/D = 1, 6 and 11. The rotor area is denoted by the grey rectangle.

Few of the vorticity regions described in literature, can be made out in the slices. These are labelled in the slice taken at distance x/D = 1. The vorticity rising from the upwind windward region (UW) extends diagonally from the center, whereas the downwind windward (DW) sector's emerging vorticity, present above the UW region, is barely visible. Besides the projected rotor area at y/D = 0.5, the upwind leeward (UL) area vorticity can be identified. The vorticity resulting from the struts is seen clearly at x/D=1, labelled as ”S”. This vorticity is absent in subsequent slices taken at distances of x/D = 6 and 11, as those turbines come under turbulent wake flow.
The slice taken behind second row VAWT shows homogeneous vorticity regions. The vorticity produced in UW and UL regions is clearly visible in the region, seen at the corners of projected rotor area. The vorticity behind the last row of wind farm is the weakest. Its diffusion can be observed clearly within this plane, drawn at x/D = 11. We can make out 4 regions of low strength vorticity at corners of the projected rotor area, resulting in flow entering this area from top and bottom.

Looking at the in-plane vectors, we observe the flow behind first row turbine moves laterally, towards the -y/D direction. This is because the vortices are not developed in size, to influence the flow direction. Thus we observe flow movement similar to the one around a cylinder. In contrast, a strong vertical movement of the flow is observed behind the second row turbine, at the center y/D = 0. The upwind-windward circulatory structures represented in shades of red and blue are visible prominently, and are responsible for this behaviour. Similar motion is seen in the last slice, where it enters the rotor area from top and bottom, and exits from the sides.

Pitch 10°

The normalized streamwise vorticity of the wind farm for +10° pitch angle is presented in Figure 4.11. Similar to the earlier plot, the iso-surfaces are drawn for values of $\omega_x \cdot D/U_\infty =$ 0.5 and -0.5, in colors of red and blue respectively. Similar slices are made at x/D = 1, 6 and 11 distances, with vorticity contour plots . Flow movement within the planes is depicted with vectors, and projected rotor area is represented with the grey rectangle.

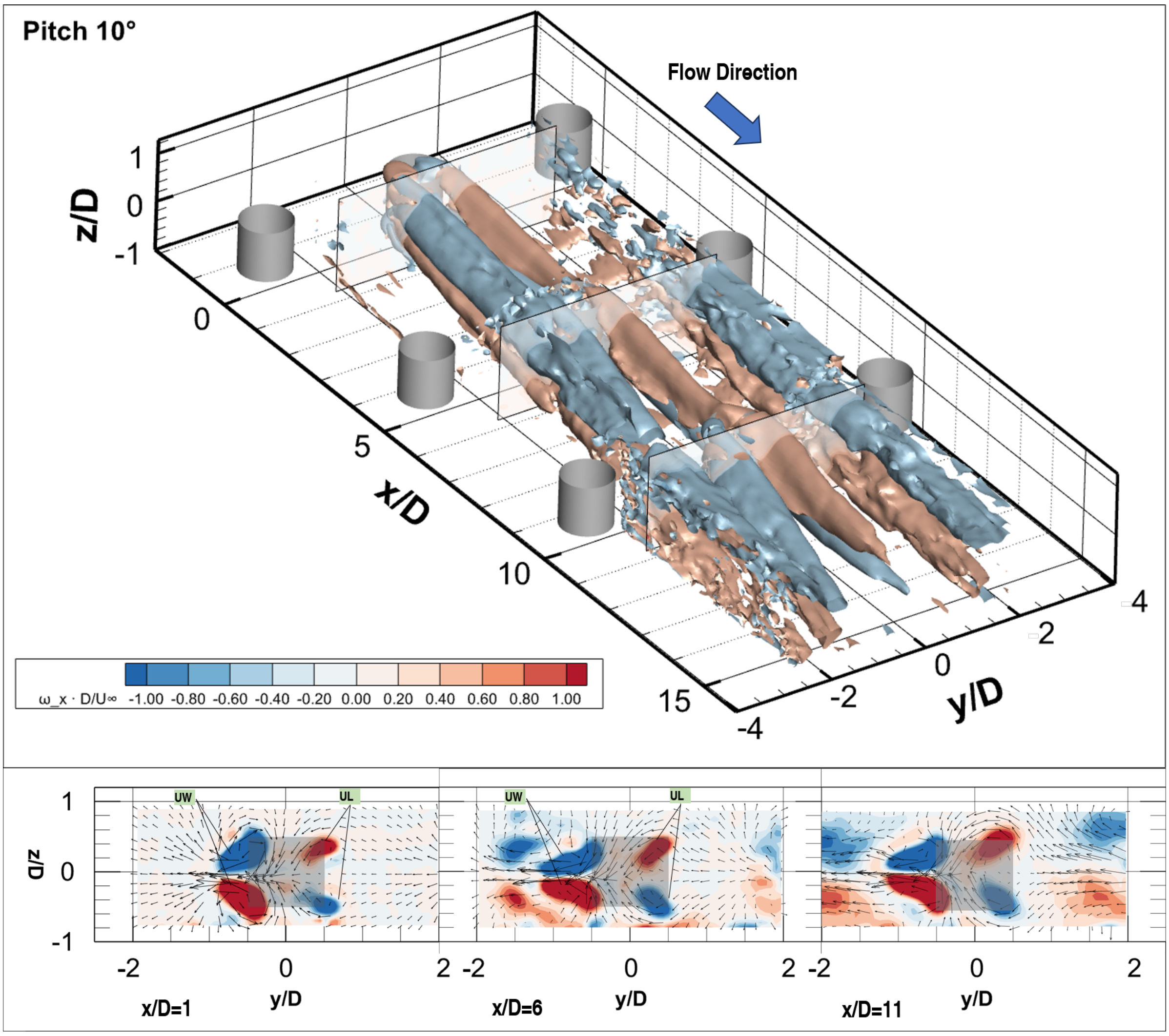

Figure 4.11: Normalized streamwise vorticity for 10° pitch angle. Flow moves in the +x direction. Iso-surfaces are drawn at values of ± 0.5. Slices are taken at x/D = 1, 6 and 11. The rotor area is denoted by the grey rectangle.

We observe a pair of strong counter-rotating tip vortices being formed at the windward side of all turbines and a relatively smaller pair on the leeward side. From the iso-surface plot, we see the vorticity generated by the upwind turbines having a major influence on the vortices generated by the downwind turbines. The plane at x/D = 6 shows the laterally traversed vortical structures from first row VAWT, and the elongation of vortices ejected by the second row VAWT. This trend repeats for the second half of the wind farm, where the vorticty of second row VAWT affects the last row. Similar elongation of tip vortices is showcased by the plane drawn at x/D = 11. On the other hand, the vortical structures formed at the leeward side show almost negligible lateral displacement, but stretch inwards to the center of the area behind the rotor. Across all x-planes, the vorticity shed by the central wind turbines is similar, but we observe the presence of vorticity on the edges of the planes drawn at x/D = 6 and 11. On the right edge, at y/D = 2, we see the vorticity shed by the right column turbines, as they travel laterally towards the centre of the wind farm.

Pitch -10°

Similar to the previous pitch cases, the normalized streamwise vorticity for -10° pitch angle is discussed here. In Figure 4.12, we see similar plots of the iso-surfaces for values of $\omega_x \cdot D/U_\infty = \pm$ 0.5 in red and blue shades. The slices are made for x/D = 1, 6 and 11 distances, and the vorticity contour plots within those slices are presented. The in-plane velocity flow is portrayed using vectors, and the rotor area is marked by the grey rectangles.

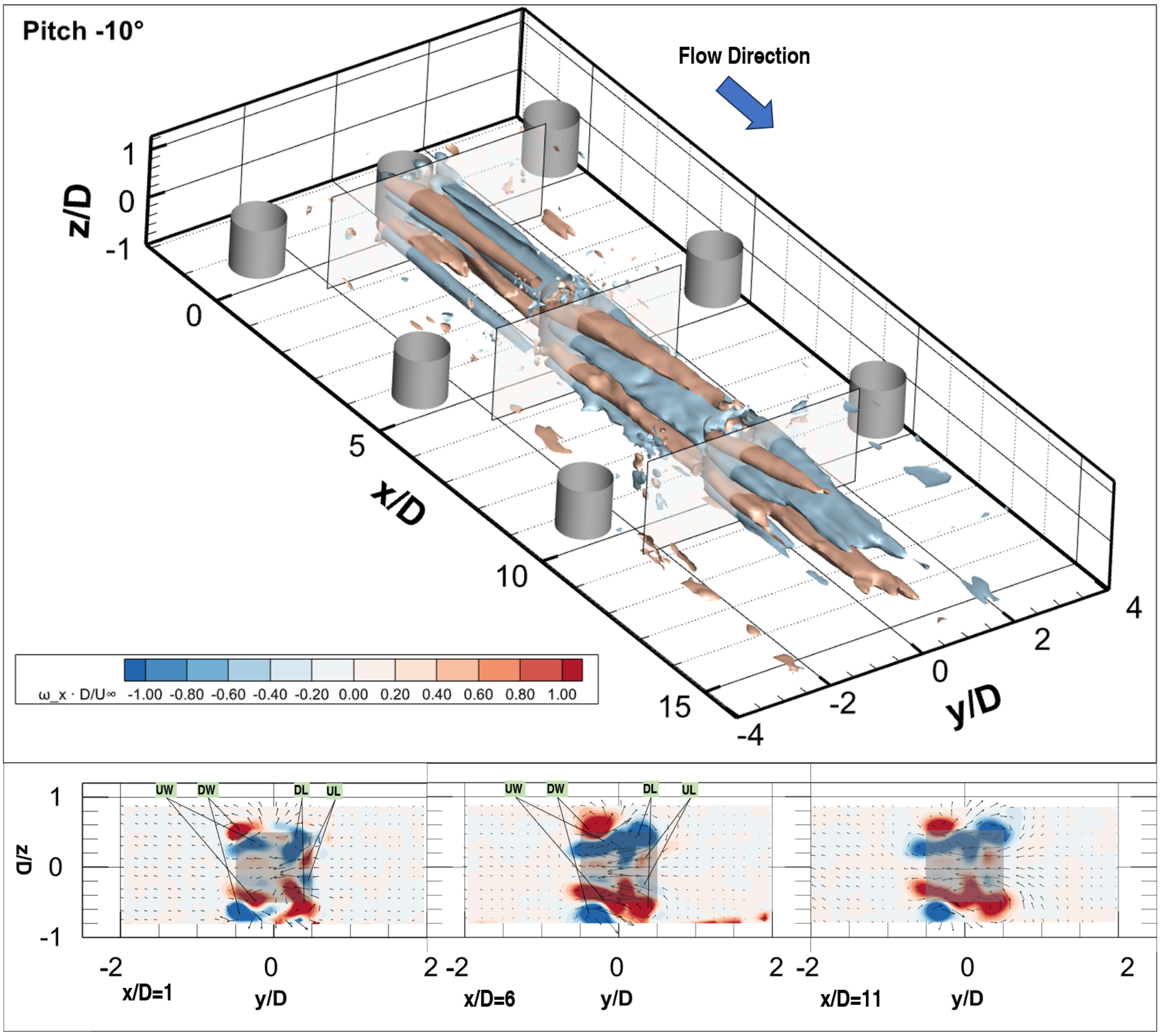

Figure 4.12: Normalized streamwise vorticity for -10° pitch angle. Flow moves in the +x direction. Iso-surfaces are drawn at values of ± 0.5. Slices are taken at x/D = 1, 6 and 11. The rotor area is denoted by the grey rectangle.

It can be seen that the vorticity is dominant in the top and bottom regions of the projected rotor area, with pairs of counter rotating tip vortices. These vortices appear to be discrete behind the first rotor, as seen in plane x/D = 1, but merge further downstream into homogeneous circulatory structures. We see the upwind windward (UW) and downwind leeward (DL) pairs of co-rotating vorticity regions merging together in the second half and exit regions of the wind farm. Lateral advection of flow behind the rotor sweep area can be observed resulting from this vorticity. This advected flow into the projected rotor area shows little vertical movement and exits the sweep area from the windward side.

From the plots presented in this section, the first apparent observation that can be made is the presence of strong vorticity when the blades are pitched, represented by the dark shades of red and blue. This development of streamwise vorticity is in-line with the theory presented by Huang et al. [32], which is discussed previously in the literature review. In the next section, acquired streamwise velocity data of the wind farm is presented.

4.2.4. Streamwise Velocity

In the previous section, the vorticity of the wind farm for different pitch angles was discussed. We now look at the structure of the wake of the wind farm for those angles. This is done by plotting contours of normalized streamwise velocity.

Pitch 0°

The following Figure 4.13 show the normalized time averaged streamwise velocity slices for distances x/D = -1, 1, 3, 5, 7, 9, 11, 13 and 15. In addition, the in-plane velocities are visualized using vectors. The wind turbines are represented by grey cylinders.

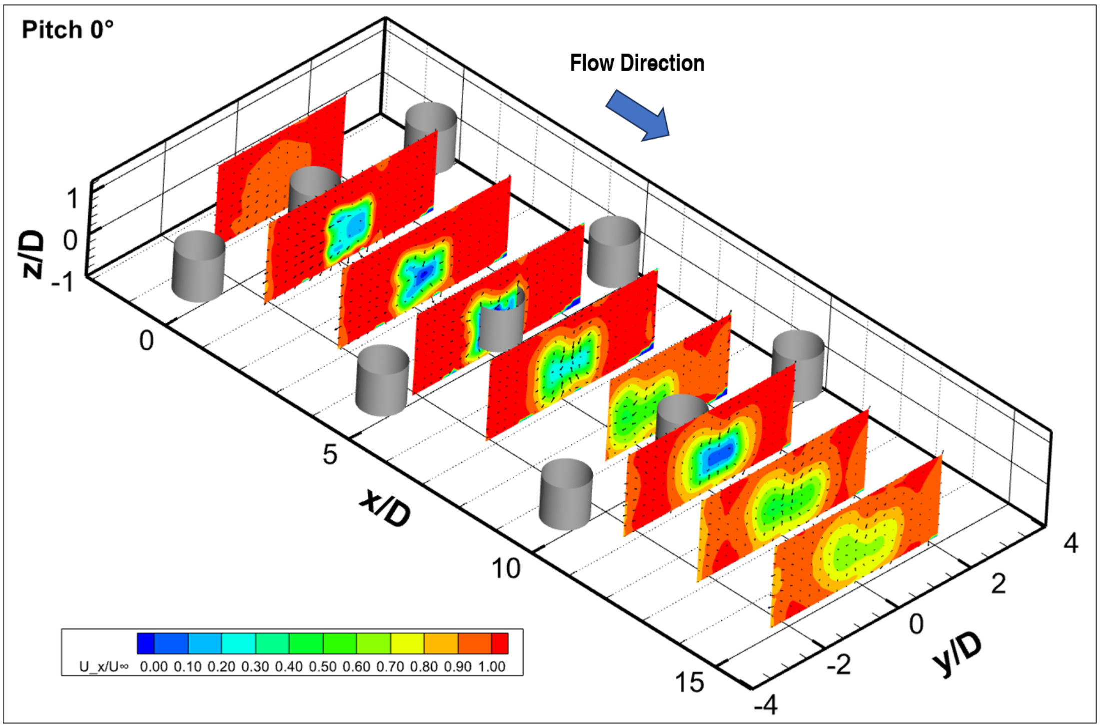

Figure 4.13: Normalized streamwise velocity contour plots. Turbines are represented as grey cylinders. Slices are made at x/D = -1, 1, 3, 5, 7, 9, 11, 13 and 15.

We observe almost no deflection of wake when the blades are not pitched, and the flow deficit interacts with the down-stream turbines. The wake takes a trapezoidal shape, behind the first row central VAWT. The lowest velocity region depicted in shades of blue is consistently observed behind each of the central turbines. The wake of the central turbine expands laterally as it moves downstream. This expansion is in-line with the presence of steamwise vorticity, which in turn, is the consequence of asymmetrical loading in the upwind and downwind halves of the rotor. This vorticity drives the in-plane flow's vertical motion behind the rotor area, and expels it from the sides, and deforms the original trapezoidal shape of the wake.

Pitch 10°

Similar to the above zero pitch case, Figure 4.14 show the normalized time averaged streamwise velocity. The volume is sliced at distances x/D = -1, 1, 3, 5, 7, 9, 11, 13 and 15. The in-plane velocities are denoted using vectors, and wind turbines are represented by grey cylinders.

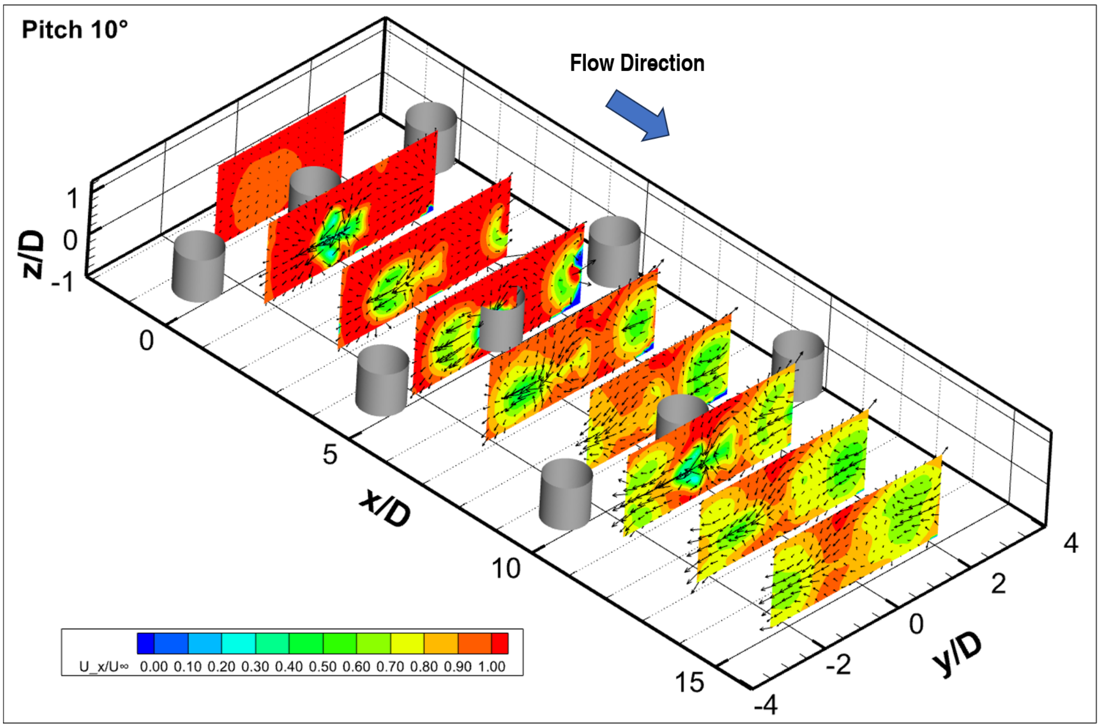

Figure 4.14: Normalized streamwise velocity contour plots. Turbines are represented as grey cylinders. Slices are made at x/D = -1, 1, 3, 5, 7, 9, 11, 13 and 15.

Unlike the baseline case of zero pitch, the wake traverses laterally when the blades are pitched inwards (positively) by 10°. This deflection of wake can be linked to the lateral loading observed in the thrust plots (Figure 4.2). The wake expansion in the -y direction is in agreement with the previously discussed actuator cylinder force field theory, along with the presence of strong pair of counter rotating vortices at the windward side of the rotor. As a result, the region of lowest velocity, depicted in green, is concentrated on the windward side of the turbine where vorticity is dominant. Due to the lateral movement of the wake, the next row turbine receives inflow almost equal to the free-stream velocity. We see small wake regions present at the center and leeward side of the wind turbines.

The laterally traversed wake profiles of the rightmost VAWTs, at y/D = 3, become clear around the second half of the wind farm. The vorticity present at the leeward side diverts the wake in +y/D direction, which later mergers with the laterally shifted wakes, seen in the last slice at distance x/D = 13. Thus, at the exit region of the wind farm, we see two large low velocity regions on either side of the central VAWT column.

Pitch -10°

The measured time-averaged streamwise velocity contour and in-plane velocity vectors are presented in Figure 4.15 below, with turbines represented as grey cylinders.

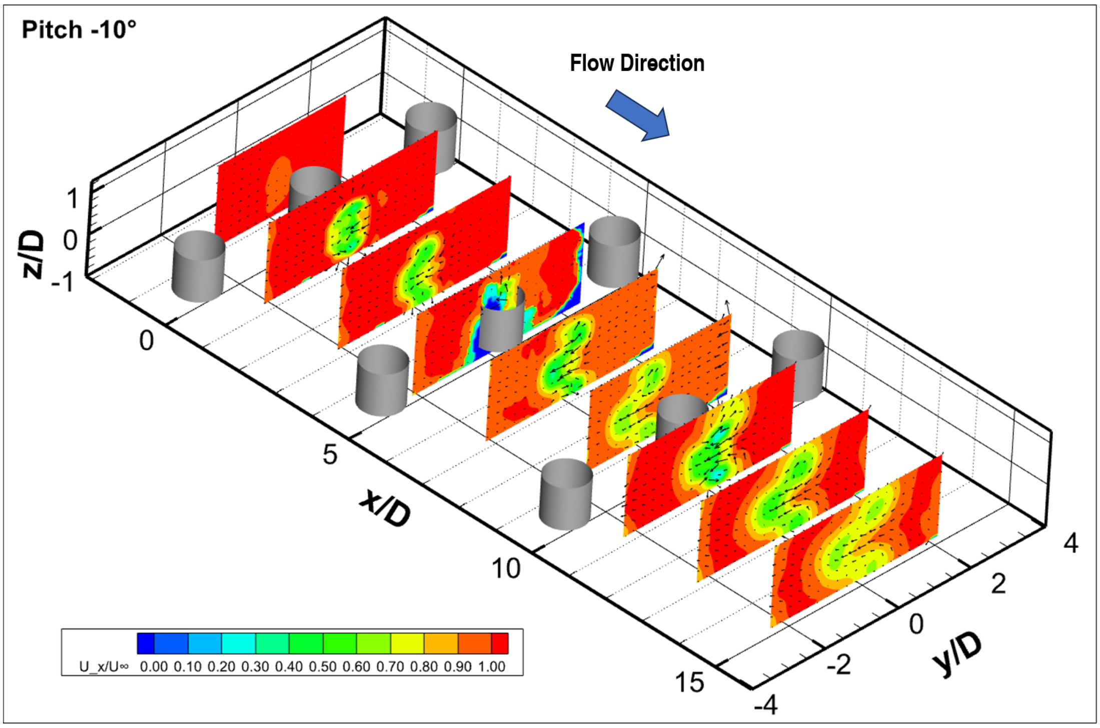

Figure 4.15: Streamwise velocity contour plots.Turbines are represented as grey cylinders. Slices are made at x/D = -1, 1, 3, 5, 7, 9, 11, 13 and 15.

When the wind turbine is pitched by -10°, the vertical deflection of wake is observed, caused by the high strength vorticity prevailing in the axial regions of the VAWTs. This axial movement occurs at a lower intensity behind the first row of wind farm, but increases as it merges with the wakes of second and third row VAWTs. As discussed earlier, the flow advection behind the rotor is observed. This causes the lateral expansion of wake towards the windward direction (-y/D) and we see little vertical movement of flow. This creates a similar kidney-bean shape as observed for yawed HAWTs. Looking at the extreme end slice at x/D = 15, three low velocity regions can be distinguished in shades of green.

4.2.5. Lateral Velocity

In the above subsection, the streamwise velocity plots were presented. Different wake topologies were observed, resulting from the vorticity regions. In this subsection, we see the effect of this vorticity on the lateral velocity component for the three pitch cases.

Pitch 0°

Figure 4.16 shows the normalized lateral velocity for baseline case of no blade pitch angle. Three planes taken at distances z/D = -0.5, 0 and 0.5. The ± 0.5 heights represent planes at the top and bottom tips of rotor, and z/D = 0 is the plane of axial symmetry. In-plane vectors display the direction of flow and wind turbines are represented by grey circles.

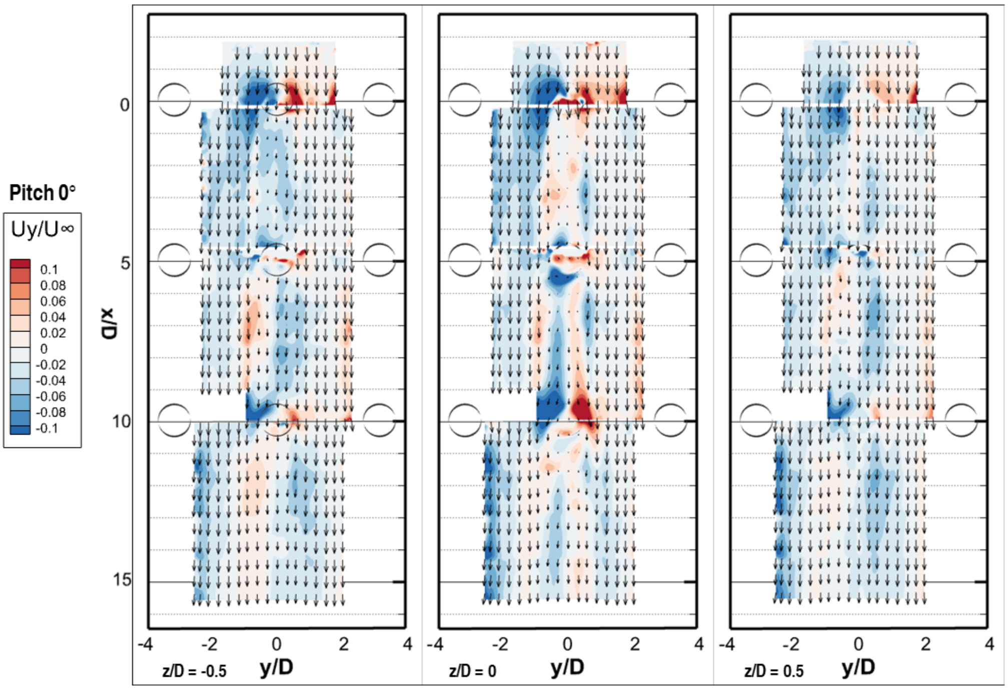

Figure 4.16: Normalized Lateral Velocity. Slices taken at z/D = -0.5 , 0 and 0.5 are presented from left to right. Wind turbines represented as circles.

The flow shows low magnitude of lateral velocity component due to lower lateral load forces, and higher lateral displacement around the turbines can be seen as a result of expansion caused by blockage. We can see the flow behaves similarly at slices taken at heights z/D = 0.5 and -0.5. In the first half of the wind farm, the lateral movement towards the - y/D direction is dominant. In the second half region of the wind farm, the flow shows lateral movement in the +y/D direction from the windward side and towards the -y/D direction from the leeward side, towards the centre of the wind farm at y/D = 0. This movement is absent at the central plane at z/D = 0, where vorticity ejected by the central VAWT propels the flow towards the negative and positive lateral directions, as represented in dark shades of blue and red respectively.

Pitch 10°

The normalized lateral velocity component of the flow for the case of pitching inwards to the axis of rotation by +10° is showcased in Figure 4.17 below. The three planes presented from left to right are taken at distances z/D = -0.5, 0 and 0.5 respectively. Vectors indicate the direction of flow and grey circles mark the locations of rotors.

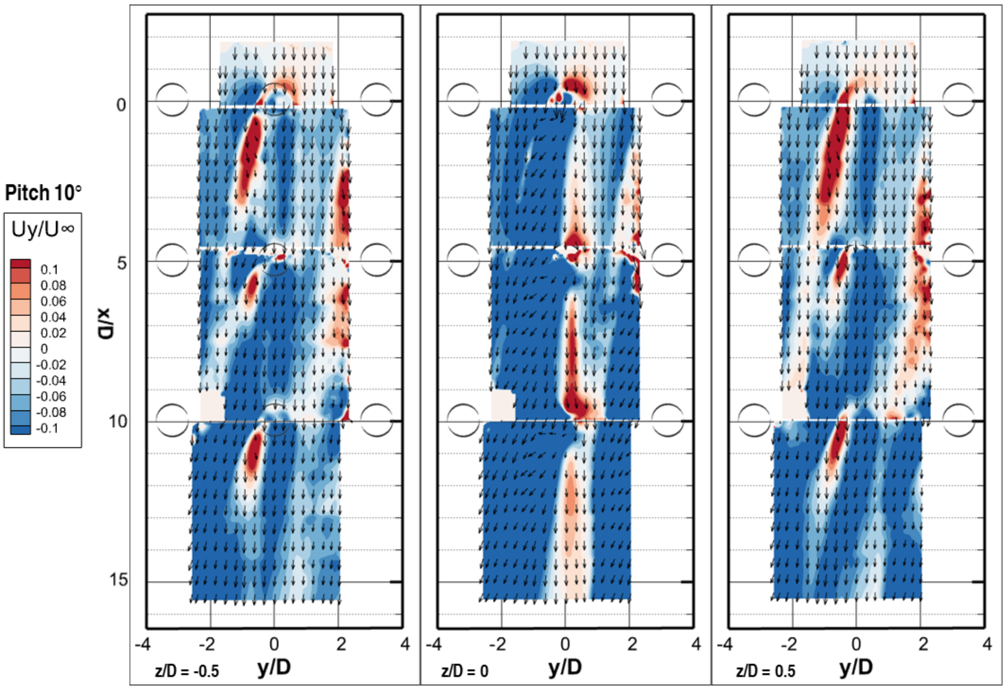

Figure 4.17: Normalized Lateral Velocity. Slices taken at z/D = -0.5 , 0 and 0.5 are presented from left to right. Wind turbines represented as circles.

A strong lateral flow prevails throughout the wind farm regions towards the -y/D direction. The flow towards the +y/D direction, represented in shades of red are observed as a result of either streamwise vorticity, or solid body blockage caused by the turbines. The lateral movement of flow in +y/D direction, observed at the windward(left) side of the VAWTs at slices z/D = ± 0.5 traces the path of trailing vorticity from blade tips. The central plane sliced at z/D = 0 in the volume indicates lateral movement in the +y/D direction at the leeward side (right) of the VAWTs. This movement is driven by the tip vortices formed at the upwind leeward, which cause expansion of wake towards the right.

Pitch -10°

Similar to the previous cases, Figure 4.18 shows the normalized lateral velocity for blade pitch angle of -10°, where the blades are pitched away from the axis of rotation. Slices taken at distances z/D = -0.5, 0 and 0.5 are presented from left to right respectively. In-plane vectors display the direction of flow and wind turbines are represented by grey circles.

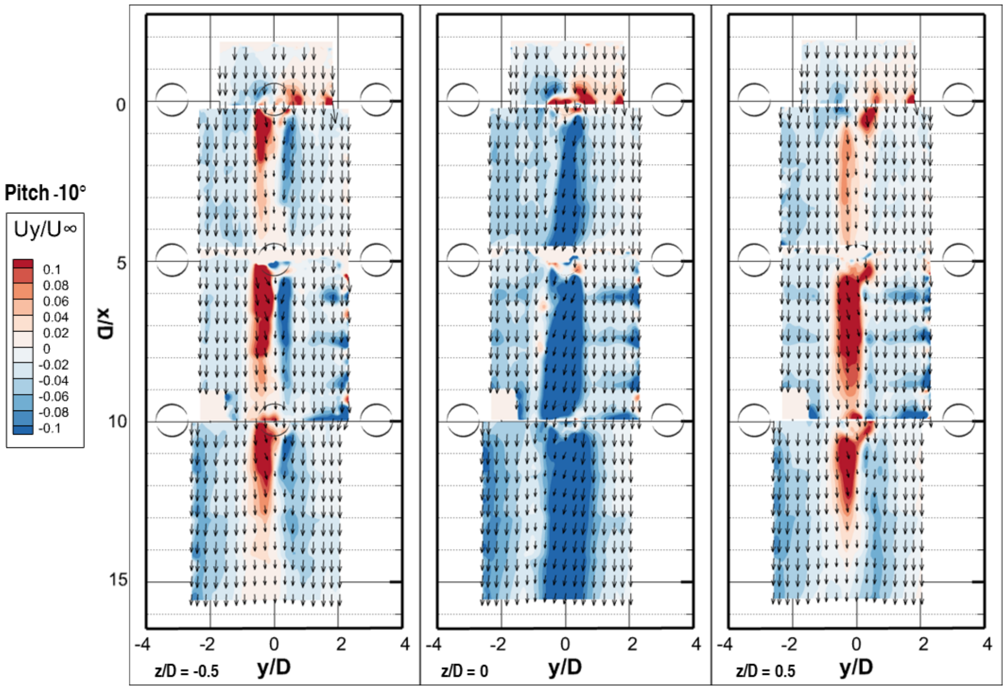

Figure 4.18: Normalized Lateral Velocity. Slices taken at z/D = -0.5 , 0 and 0.5 are presented from left to right. Wind turbines represented as circles.

The lateral component of streamwise flow shows varying behaviour at different heights in the wind farm for this pitch case. The results are in-line with the stratified vorticity regions. We first take a look at the volume slices extracted at distances z/D = ± 0.5. It is previously noted that counter rotating tip vortices ejected from the windward side traverse towards the center, causing lateral movement in the +y/D direction. This movement is presented in shades of red in the left and right plots. Advection of flow from the leeward side, behind the rotors, is observed at the central plane. This movement is displayed in dark blue, around y/D = 0.

By looking at the lateral component of velocity, it can be concluded that pitching the blades positively, which is towards the axis of rotation, leads to highest lateral deflection of wake out of all the pitch cases. For -10° pitch case, variations in the direction of lateral movement is observed from -0.5 to 0.5 distances in axial direction (z/D). In contrast, the baseline case where rotor blades aren't pitched, shows little lateral movement of flow along the leeward (right) side of the VAWT towards the -y/D direction, apart from body blockage.

4.2.6. Axial Velocity Component

After looking at the lateral component of streamwise flow, the axial component is presented in the current subsection, for the different blade pitch cases.

Pitch 0°

The axial component of the wind farm's wake for the baseline case is presented below, in Figure 4.19. Three slices are taken at distances y/D = -0.5, 0 and +0.5. The contour plots depict upward movement in +z/D direction as shades of red and downward movement in -z/D direction as shades of blue. The vectors show the in-plane velocity.

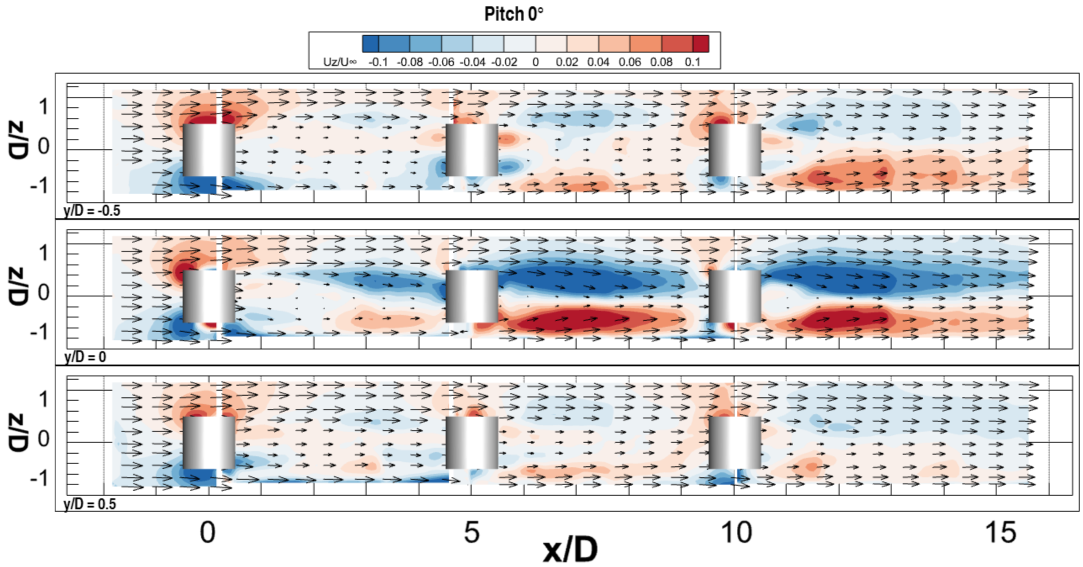

Figure 4.19: Axial velocity component of streamwise flow for baseline case. Slices represent planes at y/D = -0.5, 0, and 0.5 plotted from top to bottom. Grey rectangles represent the wind turbine rotors.

From the above plots, we see that the majority of axial flow movement lies behind the VAWTs, at y/D = 0. Downward movement of flow is observed in the top half wind farm region, and in contrast, upward flow movement is dominant in the bottom half region. This indicates that the wake contracts vertically at the center, and as previously observed, expands in the lateral directions. The vertical convergence of flow behind the first-row turbine becomes significant after a distance of 3D, and is present at the outer regions of the wake. The movement in -z/D direction has higher magnitude in the first half of wind farm region.

In the exit region of the wind farm (x/D = 10 to 15), we see upward movement of flow in the y/D = -0.5 plane. This behaviour can be attributed to the laterally traversed vorticity ejected from the UW region of the rotor area, towards the -y/D direction.

Pitch 10°

Figure 4.20 depicts the vertical movement of flow when the blades are pitched inwards by 10°. Slices taken at 3 lateral distances, y/D = -0.5, 0, and 0.5, are arranged from top to bottom. Movement in +z/D direction is represented in shades of red and downward movement in -z/D direction as shades of blue. The in-plane vectors depict the direction of flow.

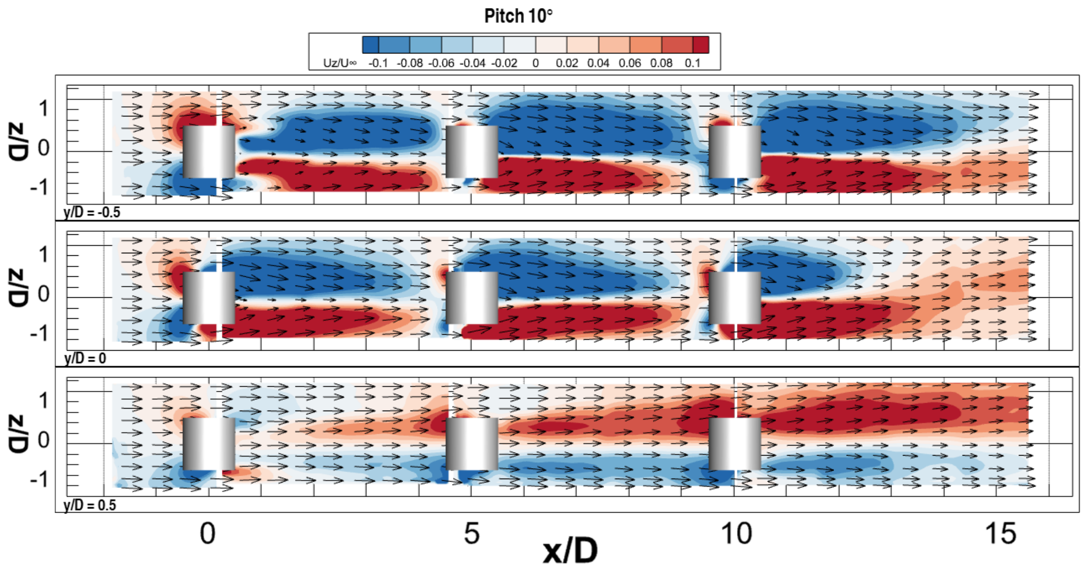

Figure 4.20: Axial velocity component of streamwise flow for pitch angle +10°. Slices represent planes at y/D = -0.5, 0, and 0.5 plotted from top to bottom. Grey rectangles represent the wind turbine rotors.

In the top slice taken at y/D = -0.5, strong down-wash of flow behind the turbines is observed which stops at the center of the plane (z/D = 0), where it is met by equally strong up-wash. Examining the flow around the upper half of the first VAWT at x/D = 0, we observe that body blockage causes movement in the +z/D direction, which then inverts and begins to move in the -z/D direction. This behaviour is mirrored in the lower half region, as vertical symmetry is observed along z/D = 0. The change in direction of flow is the result of vorticity being shed at the windward side.

Similar axial movement can be seen in the central plane at y/D = 0, apart from the noticeable effect of downwind turbine's induction. We see the axial flow component reducing, and ultimately becoming zero around 1D distance before encountering the downwind turbine (at x/D = 4 and 9). In the exit region of the wind farm, the axial movement of flow in -z/D direction lasts till x/D = 13, and afterwards, it is restricted to the +z/D direction. This occurs as the leeward side vorticity translates laterally in the -y/D direction at a faster rate, due to the influence of laterally advected flow from the rightmost turbine column, at y/D = 3.

The last contour plot taken at y/D = 0.5, shows the axial component of flow resulting from the trailing vorticity at the leeward side. As the flow moves downstream, amount of flow subjected to axial induction increases, which can be linked to the vorticity's lateral displacement towards the -y/D direction.

Pitch -10°

Similar to the previous pitch cases, Figure 4.21 presents the axial flow component for outward pitching (negatively) of blades. The XZ planes at lateral distances y/D = -0.5, 0, and 0.5 are sequentially presented from top to bottom. Rotors are represented using grey rectangles, and the vectors show the movement of flow within the plane.

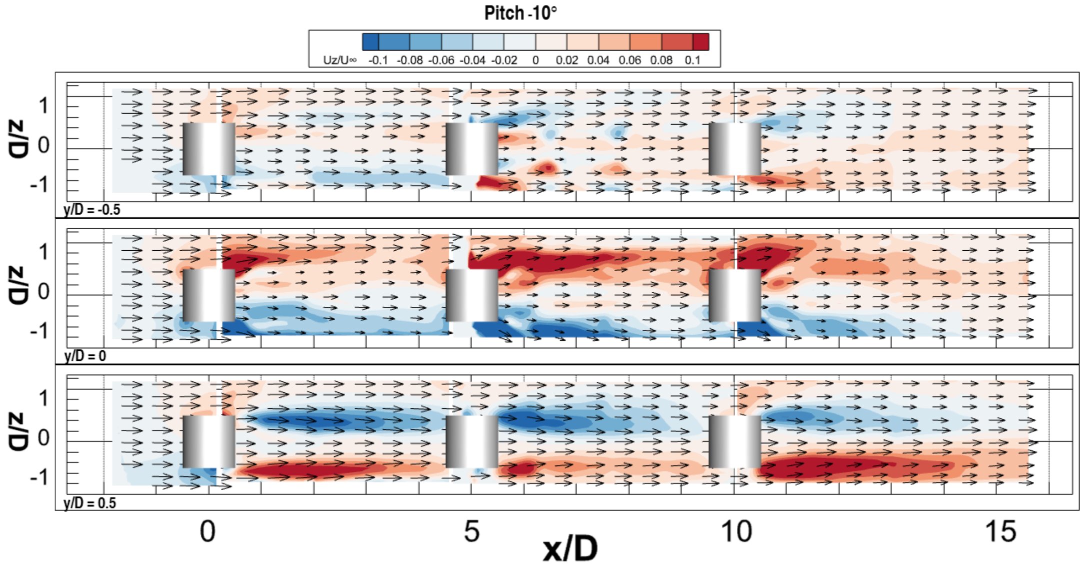

Figure 4.21: Axial velocity component of streamwise flow for -10° pitch angle. Slices represent planes at y/D = -0.5, 0, and 0.5 plotted from top to bottom. Grey rectangles represent the wind turbine rotors.

From the slice taken at y/D = -0.5, we observe little vertical movement of flow, that results from the vortical structures ejected from the top and bottom of the rotor sweep area. As these structures move laterally towards the center of the farm (y/D = 0) when the flow progresses downstream, the magnitude of axial flow component plotted in the plane reduces to zero. We observe the flow being forced in -z/D direction from the top and movement in +z/D direction is seen at the bottom by the trailing vorticity, but this movement is absent behind the VAWTs.

Majority of the vertical advection of flow can be seen in the central slice, taken at distance y/D = 0. We observe the flow in the top half of the wind farm having axial advection in the +z/D direction, and the bottom half in the -z/D direction. This movement is limited to the top and bottom regions of the wind farm, while majority of the area behind the rotors has trace amounts of vertical flow component.

The nature of the axial flow element in the lowest plot, representing the plane at y/D = 0.5, is in stark contrast to the central plane at y/D = 0. The direction of axial flow is reversed, and we observe this flow element's magnitude reducing as the flow moves downstream. This axial advection region is present at the edges of the area behind the rotor and shows slight expansion in the exit region of the wind farm.

4.2.7. Streamwise Velocity Deficit

From the previous subsections, we have looked into the movement of the flow which is dictated by the high vorticity circulatory structures, stemming from the wind turbines. From the differences in wake topology, the distribution of streamwise velocity deficit has been analysed and presented in Figure 4.22. From top to bottom, the outward pitch, zero pitch, and inward pitch cases are presented, where pitch angle is 10°. The slices represent the central XZ plane, at distance y/D = 0. The arrows represent the streamwise velocity profile, drawn at intervals of 1 rotor diameter D.

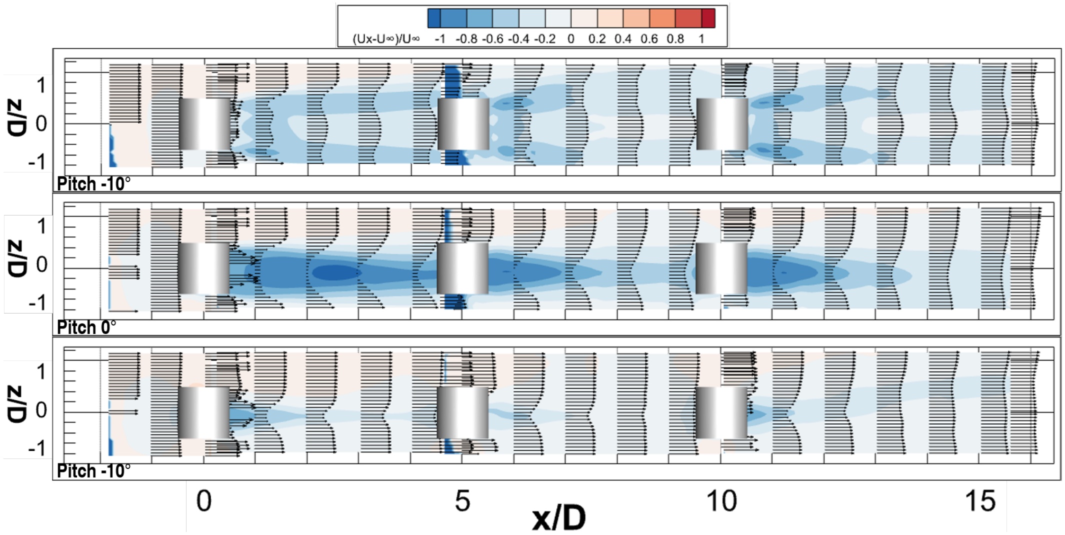

Figure 4.22: Normalized streamwise velocity deficit contour plot. Ux is streamwise velocity and U_∞ is freestream velocity. Top plot: -10°, middle plot: 0°, bottom plot: 10°. The arrows represent streamwise velocity profile.

For the -10° pitch case, it can be observed that the velocity deficit is concentrated at the top and bottom regions of the wind farm. The streamwise flow component recovers earlier at the middle of the wind farm, at z/D = 0, and then gradually, the deficit recovers at the top and bottom regions as the flow moves downstream. The velocity deficit in the area above the rotors starts increases, caused by the up-wash of wake.
Looking at the baseline case of 0° pitch angle, presented in the middle plot, the velocity deficit is concentrated behind the rotors. The highest velocity deficit is present until 3 rotor diameters away from the first turbine (x/D = 3). Most of the flow's recovery is observed in the second half and exit regions of the wind farm, where the highest deficit lasts for a distance of 2D.
The lowest deficit out of all pitch cases is seen for the inward pitch case of +10°. Similar to the previously discussed baseline case, the velocity deficit is present behind the center of the rotors, at z/D = 0. The flow recovers almost completely in the first and second halves of wind farm, before encountering the next downstream turbine. In the exit region of the wind farm, the velocity deficit begins to shift in the +z/D direction, as depicted by the faint blue patch. This movement could be the result of the laterally deflected vorticity, ejected at the leeward side of the rotors.

Based on the above plots and discussion, the pitch case with least velocity deficit, observed in the +10° case, should have a higher recovery of wake, and subsequently, greater available wind power. The analysis of the wake recovery is presented in the next subsection.

4.2.8. Streamwise Momentum Recovery

The RHS terms of the RANS Equation 3.3 are presented in Figure 4.23 as contour plots, with the exception of the pressure term. The slices are taken at a distance x/D=2, with the projected frontal area of the rotor represented as the grey rectangle. The terms are normalized by the maximum value of the LHS, $\bar{u}(\partial\bar{u}/\partial x)$, a method previously utilized by [6] and [32]. The terms are plotted such that positive values contribute positively to the recovery of momentum and vice versa.

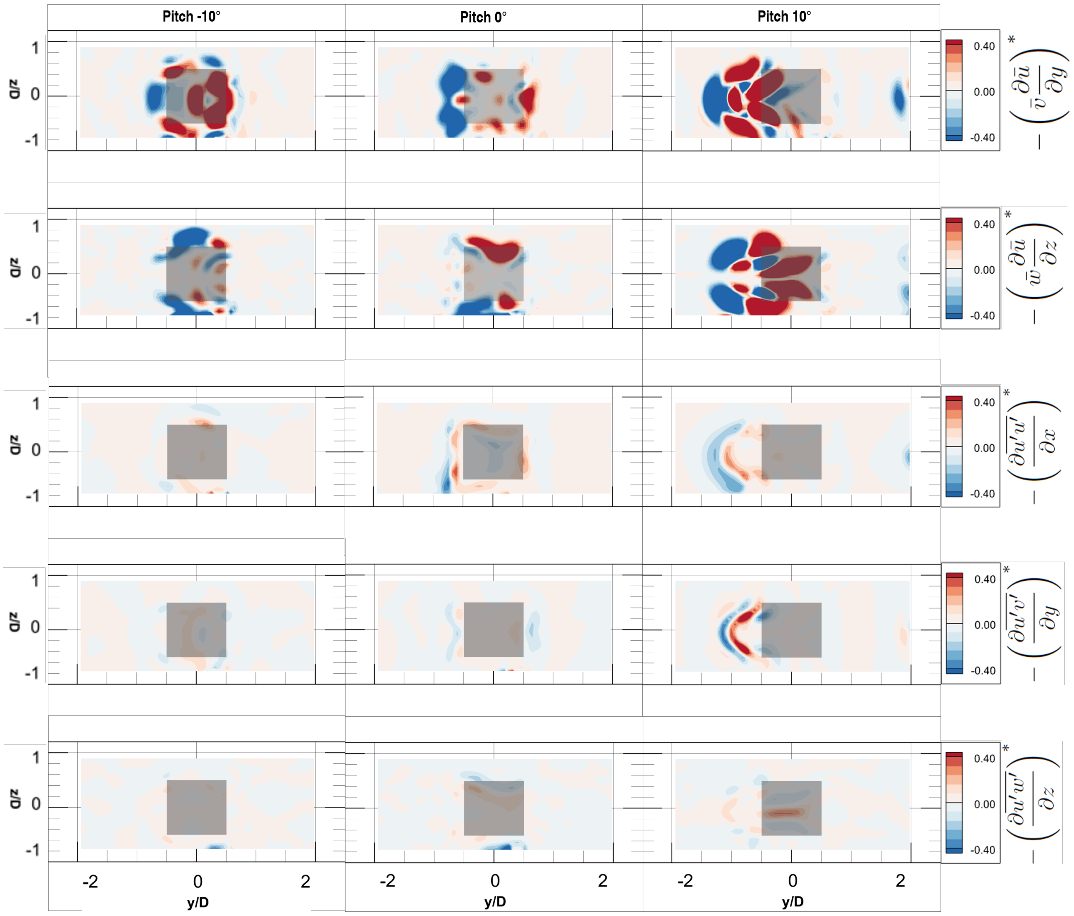

Figure 4.23: Measured terms of the RANS Equation 3.3 in the streamwise direction, at distance x/D=2. Terms are normalized by the maximum value of $\bar{u}(\partial\bar{u}/\partial x)$ represented as *.Central grey rectangle represents the projected rotor area.

The first row represents the lateral advective term of streamwise momentum. We observe positive contribution on the leeward side of -10° pitch case, caused by the strong vortical structures. For the +10° pitch case, the contribution is positive on the windward side. A common observation for all pitch cases is negative contribution regions on the windward edges of the wakes caused by horizontal expansion, similar to the observations of Huang et. al.[32].

Looking at the axial advection plots in the second row, we observe negative contribution regions at the windward side, where axial expansion of wake occurs. +10° pitch case showcases large positive regions along the windward edge, while the baseline case of 0° has them on the top along z/D = 0.5. Very little positive regions are observed for the -10° pitch case, as axial expansion of wake occurs around z/D = ± 0.5. We observe axial advection contributing negatively to the momentum recovery in this expansion region, by the presence of blue regions.

The Reynolds stress terms have significantly less contribution to the momentum recovery, compared to the advection terms. Few regions can be made out for the +10° case, along the windward region, at the edge of wake.

The contribution of each term on the RHS of Equation 3.4 towards the wake recovery is presented in Figure 4.24. From top to bottom, lateral advection, axial advection, and Reynolds stress terms in X, Y, and Z directions are plotted. For each plot, the pitch cases $0°$, $10°$, and $-10°$ are represented in blue, red, and green colours respectively, and values are normalized by $\frac{D}{U_\infty}$. The shaded regions mark the location of rotors in the farm.

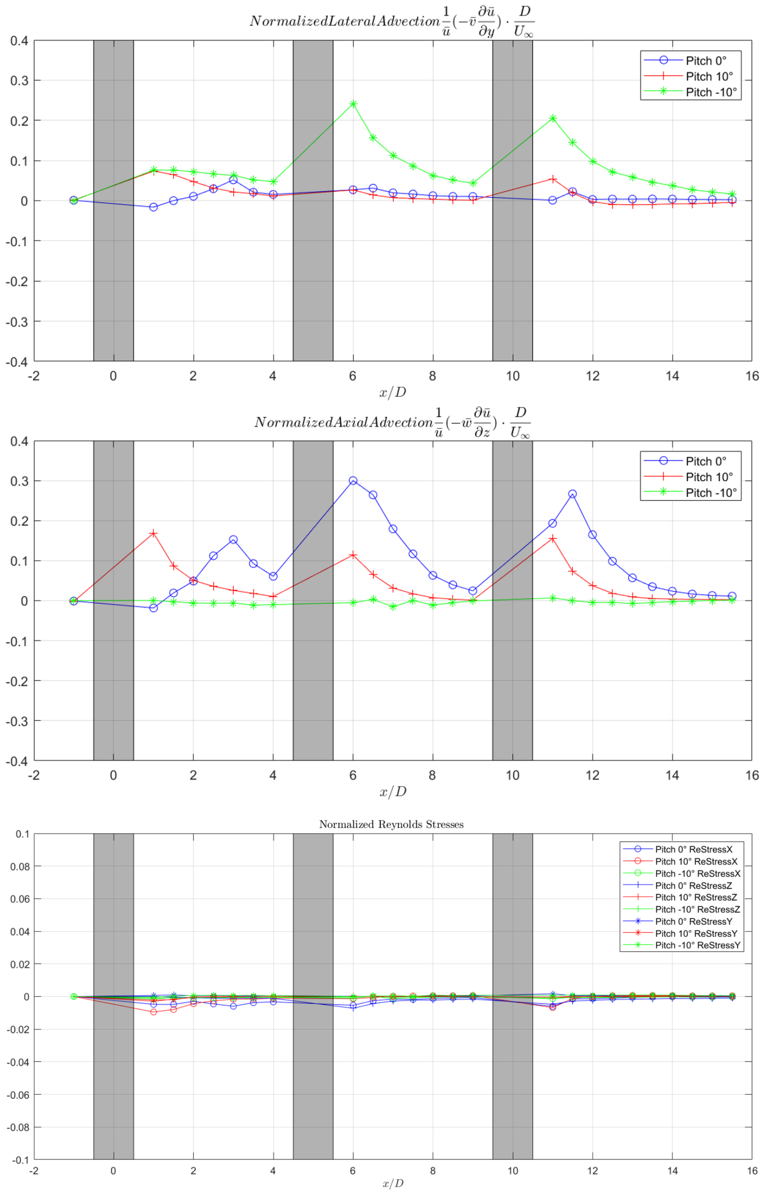

Figure 4.24: Budget of wake recovery. Each term is averaged within the projected frontal rotor area. The grey shaded regions mark the location of rotors along the streamwise direction.

Analysis of the wake recovery budget indicates lateral and axial advection to have the highest contribution. Looking at the axial advection budget, cases of 0° and 10° angles have a positive contribution to recovery, whereas -10° pitch case has negative contribution. The baseline case (0°) shows negative contribution till 2D distance, and then becomes positive further downstream. In the second half and exit regions of the wind farm, the contribution is the highest 1.5D away from the VAWT, and then reduces towards zero further downstream.

The lateral advection budget analysis shows similar trends to the axial counterpart. We see the contribution peaks at 1D distance downstream of the turbines for 10° and -10° pitch cases. The peak for 0° case occurs at 1.5D distance. We also observe the contribution being negative for the baseline case till a distance of 2D from the first row VAWT, which receives freestream flow. This observation has been previously recorded by Boudreau and Dumans[7] for their 3D cross-flow turbine. Lateral advection is the highest contributor of wake recovery for the pitch case of -10°, which can be linked to the high momentum flow entrainment observed at the leeward side of VAWTs. On the other hand, in the exit region of the wind farm for pitch case of 10°, the contribution drops below zero in the wind farm exit region, after distance x/D=13, as the laterally traversed low momentum wake enters the region of interest. Lastly, the Reynolds stress terms are found to have negligible contribution compared to the advection terms, associated to the momentum recovery budget of the wake.

The next subsection discusses the available power within the wind farms for the three pitch cases.

4.2.9. Available Power

The available wind power (AP) integration is carried out at intervals of 1D starting from the induction region at x/D = -1. This is presented in Figure 4.25, for cases of $0°$, $10°$, and $-10°$ blade pitch angles, represented in blue, red, and green colours respectively. The grey-shaded regions represent the streamwise locations of rotors in the farm layout. The solid lines state the AP trend calculated in the projected frontal area of the rotors ($\mid y \mid$ < 0.5D and $\mid z \mid$ < 0.5D). The dashed lines represent the trends of AP, integrated over the complete area inside the wind farm, for y = -2D to 2D, and z = -1D to 1D, from the center of the rotor. AP computation for complete wind farm area at x/D = 9 is omitted due to inconsistency in the integration window.

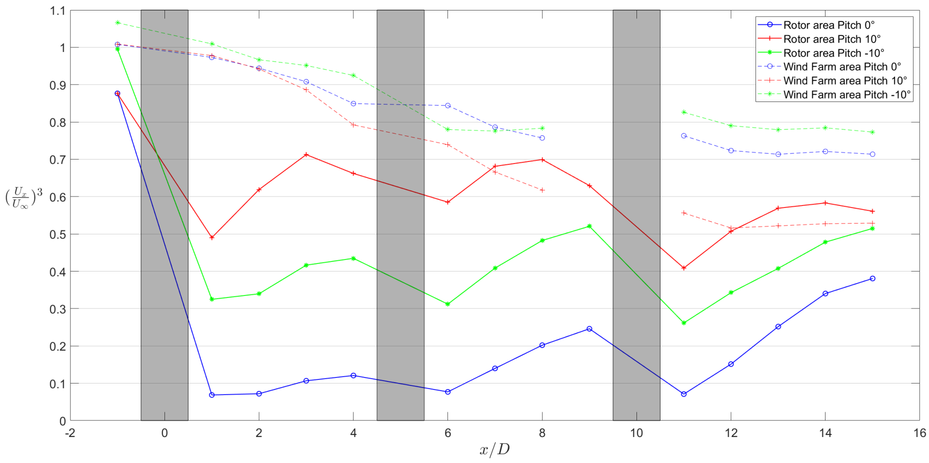

Figure 4.25: Available wind power coefficient. Solid lines represent value in the projected frontal rotor area, and dashed lines represent value in the area inside the wind farm.

Looking at the AP values in the projected rotor area, the curves representing 0° and -10° pitch cases show similar trends in a wind farm region, indicating a similar wake recovery pattern. As observed from the flow-field data, the flow deficit in the -10° case is present at the edges of the rotor area and moves vertically away from the center plane, which results in higher AP than the baseline case. Recovery of velocity deficit is executed by the vortical structures, creating lateral advection of high momentum flow into the integration window behind the rotors.
For the baseline case, the AP coefficient increases due to the diffusion of wake. As the wake encounters downwind turbines, the rate of turbulent mixing increases, and thus, the diffusion occurs at a faster rate.
Before interacting with the subsequent downwind turbine, the AP for baseline and outward pitch cases is the highest. On the other hand, the +10° case shows the highest AP 1 rotor diameter earlier than the other pitch cases.
As the volume cross-section is moved downstream within the wind farm, the integrated AP value displays a rising trend for zero and negative blade pitch angles. In contrast, the AP values for the positive pitch case are confined between 0.6 and 0.7 for the first and second halves of the wind farm. Then they decrease below 0.6, indicating a decreasing trend. This decreasing trend can be the result of laterally deflection of flow, which cause the velocity deficit present at the leeward side to traverse into the integration area. As the influence of laterally deflected wakes from extreme right row VAWTs becomes increasingly prominent in the exit region of the wind farm, the AP coefficient further reduces.

Moving towards the AP values integrated for the complete area within the wind farm, an overall decreasing trend is observed for all pitch cases. We observe the +10° pitch case shows a similar trend to

the 0° pitch case till distance x/D = 3, then reduces significantly further downstream, and has the least available wind power out of all pitch cases. The previously mentioned influence of laterally deflected wakes from right row VAWTs is clearly visible here. The integrated AP values for the projected rotor area are greater than the values for the area inside the wind farm, in the second half and exit regions of the wind farm.
The most available wind power is present for the -10° pitch case, as the low momentum wake is deflected axially, into the flow layer above the wind farm.

The average of the AP values in the projected rotor area and complete area inside the wind farm, throughout the length of the wind farm, are computed and presented in Table 4.4. The percentage increase is considered with respect to the baseline case of 0° pitch setting. A separate average of the AP for each wind farm region is carried out and presented in Table 4.5 for projected rotor area, and Table 4.6 for complete wind farm width.

Table 4.4: Average AP in the wind farm

Pitch Case	Mean AP in Projected Rotor Area	Percentage Change	Mean AP inside Wind Farm	Percentage Change
Pitch 0°	0.2159	-	0.8057	-
Pitch 10°	0.6081	+181.65%	0.6794	-15.67%
Pitch -10°	0.4348	+101.39%	0.8488	+5.35%

Table 4.5: Average AP per wind farm region, within the projected rotor frontal area

Pitch Case	First Half Mean AP	Second Half Mean AP	Exit Region Mean AP
Pitch 0°	0.0921	0.1662	0.2391
Pitch 10°	0.6209	0.6489	0.5258
Pitch -10°	0.3790	0.4310	0.4011

Table 4.6: Average AP per wind farm region, for complete width of the wind farm

Pitch Case	First Half Mean AP	Second Half Mean AP	Exit Region Mean AP
Pitch 0°	0.9185	0.7957	0.7269
Pitch 10°	0.8995	0.6743	0.5300
Pitch -10°	0.9630	0.7796	0.7905

From the above data of Table 4.4, it is evident that blade pitching increases the amount of available wind power behind the rotors, by deflecting the wake. Pitching the blades inwards (positively) by 10° leads to almost 3 times more AP behind the central VAWT, whereas pitching the blades outwards (negatively) by 10° doubles the average AP. However, this analysis is only limited to the projected frontal area of the rotor along the wind farm's length.
Looking at the complete area within the wind farm, the AP drops by 15.67%, when the blades are pitched positively (+10° case). For the -10° pitch case, an increase in AP by 5.35% is observed. Thus, the -10° pitch case performs better on a wind farm scale than the +10° case.

5

Conclusion and Recommendations

This chapter presents the main findings of this thesis, and answers the research questions formulated previously. Recommendations for further research are discussed at the end.

5.1. Conclusion

In this thesis we have discussed the aerodynamics of Vertical Axis Wind Turbines (VAWTs), and have acquired their flow data in a 3 x 3 wind farm configuration. Enhanced entrainment of flow was achieved by making VAWTs behave as votex generators via blade pitching, and the interaction of resulting flow structures was studied. To highlight the main findings of this experiment, the answers to the previously posed research questions are presented below.

- How does the flow behave within a high density VAWT wind farm?

From the PTV measurements, it is seen that similarity exists between vorticity regions of a single H-VAWT and data from past literature. As lateral loading is minimum in the absence of blade pitching, the wakes do not show lateral deflection, and interact with the downwind turbines in the same column. The highest velocity deficit is consistent in the first half of the wind farm, indicating lower wake recovery. For the second half and exit regions of the wind farm, the high velocity deficit prevails till a distance of two rotor diameters (x/D≈ 2), after which the velocity starts recovering. The efficiency of downwind turbines reduce due to the velocity deficit created by upwind turbine. The performance of downwind turbines drop to 30% of the upwind turbine's performance, which receives unperturbed wind flow.

- How can we achieve flow re-energization in a VAWT farm?
  - What is the driving mechanism behind re-energization of the flow?

  For the baseline case of 0° pitch angle, the flow re-energizes by means of axial advection. The vortical structures cause this advection by pulling in the high momentum flow vertically towards the center, and expanding the low momentum wake laterally. Consequently, mixing of the wake with freestream flow is promoted. Axial advection dominates the flow re-energization when rotor blades are pitched inwards. Strong windward vorticity drives the low momentum wake laterally, and pulls in high momentum flow behind the rotors. For the last case of outward blade pitch, lateral advection has the highest contribution towards wake recovery. High momentum flow is pulled into the projected rotor area from the sides, and the low momentum wake is deflected upwards, along with lateral wake expansion in the -y direction. Here, axial advection contributes negatively in the re-energization ,as it leads to the expansion of wake.

  - What is the effect of wake deflection on energy entrainment?

  Pitching the blades inwards provides the highest degree of wake deflection. For the +10° pitch case, the introduction of lateral forces successfully cause high kinetic energy entrainment from the freestream flow, and simultaneous expansion of wake out of the rotor area. However, as the wind farm saturates with low energy wake in the downwind regions, laterally deflected wakes

from the side turbines are entrained into the flow.
On the other hand, pitching the blades outwards also causes lateral entrainment of momentum into the area, but the advection of low momentum flow is in the axial direction. Hence, the downwind regions of the wind farm are less saturated with low momentum wake.
Analysis of the power density of the wind farm shows an increase after implementing wake deflection. Compared to the existing HAWT wind farm densities, the computed values are significantly smaller but the percentage gain in power density is higher.

– What changes can be observed in the wake topology inside the wind farm?

Pitching the blades inwards (positively) leads to lateral deflection of wake, as strength of windward vorticity increases. We see the flow ejecting out of the projected rotor area towards the windward direction, leading to the interaction of wakes from turbines between adjacent columns, as the flow travels downstream. When blades are pitched outwards, the wake shows axial movement, as the vorticity pulls the flow from the leeward side of turbines into the projected rotor area behind the turbines. This flow exits the region from the top of the area. The wake does not show lateral deflection, but promotes lateral expansion as co-rotating vortexes ejected from the top merge together and hinder axial movement of flow.

– How do the two modes of flow re-energization affect the available wind power within the wind farm?

From the analysis of available wind power, we see that pitching the blades inwards leads to the highest available power behind the turbines. However, this power shows a reducing trend as we move downstream. When the complete area within the wind farm is considered, the +10° case shows a decrease in AP by 15.6%. The AP shows an increasing pattern for the pitch cases of -10° and 0° integrated within the projected rotor area. Pitching the blades outwards (by -10°) increases the available power by a factor of 2, compared to the baseline case of zero pitch angle. When analysed for the complete wind farm area, a 5.3% increase in AP is noted. These findings highlight that changing the blade pitch angle away from the axis of rotation (negatively) is an effective technique to amplify energy entrainment and increase the amount of available wind power within the wind farm.

To conclude, the implementation of blade pitching improves the overall performance of the VAWT wind farm. A higher available wind power in the wind farm is observed, along with better performing turbines. This study indicates that employing VAWTs in wind farms would offer better power densities, but their wake re-erergization is a fast advection driven process. To further enhance the re-erergization process, different techniques like introduction of blade pitch seem viable, which prove to improve the power production and density significantly.
However, there exist a few limitations to the introduction of blade pitch angle. Additional loads on the wind turbine can lead to early degradation of supporting structures. Hence frequent maintenance will be required, increasing the O&M costs. Implementing outward blade pitching would facilitate the enhanced vertical kinetic energy entrainment in the wind farm, but at the cost of reduced turbine performance.

As studies about such VAWT wind farms are fairly new, there exists multiple directions of research which are not addressed in this thesis study. These recommendations are presented in the next section.

5.2. Recommendations

The current study characterizes the flow of a VAWT wind farm under different energy entrainment modes. As this enhanced entrained flow has indicated a positive response towards wake recovery and available power of the wind farm, it is possible to extend the study into different research areas.

The experiment is conducted in a wind tunnel with laminar flow. Studying the model in ABL flow, effect of surface roughness, and the addition of inflow turbulence would characterize the wind farm's behaviour for real world scenarios.
When considering the layout of the wind farm, a 3 by 3 rectangular grid was studied with lateral spacing of 3.1D and streamwise spacing of 5D. Increasing the lateral spacing, would decrease the adjacent

row's influence when positive blade pitching is implemented. Thus a relation between blade pitch angle and lateral spacing can be derived.
In this experiment, blades are pitched by a fixed angle. One can implement active blade pitching, and analyse the optimum pitch angles for specific objective of interest.
From the analysis of outward blade pitching case, it is observed that the wake deflects in the axial direction, and expands laterally. As lateral wake deflection is absent for this pitch case, misalignment of rotors would allow greater wake recovery, and higher efficiency of turbines can be seen.
Previous literature has indicated that counter rotating VAWT pairs show better performance than isolated VAWTs. Thus one can change the direction of rotation of the central column turbines, and study the changes in the flow's behaviour.
Vertical deflection of wake was observed for the -10° pitch angle case, where the readings were taken at the height of the rotor. Further analysis of wake recovery can be studied in detail by acquiring the flow above rotor height.

References

[1] J.F. Ainslie. “Calculating the Flowfield in the Wake of Wind Turbines”. In: *Journal of Wind Engineering and Industrial Aerodynamics* 27.1-3 (Jan. 1988), pp. 213–224. ISSN: 01676105. DOI: 10.1016/0167-6105(88)90037-2. URL: https://linkinghub.elsevier.com/retrieve/pii/0167610588900372 (visited on 07/06/2024).

[2] Jennifer Annoni et al. “Evaluating Tilt for Wind Plants”. In: *2017 American Control Conference (ACC)*. 2017 American Control Conference (ACC). Seattle, WA, USA: IEEE, May 2017, pp. 717–722. ISBN: 978-1-5090-5992-8. DOI: 10.23919/ACC.2017.7963037. URL: https://ieeexplore.ieee.org/document/7963037/ (visited on 07/15/2024).

[3] Andrew Barnes, Daniel Marshall-Cross, and Ben Richard Hughes. “Towards a Standard Approach for Future Vertical Axis Wind Turbine Aerodynamics Research and Development”. In: *Renewable and Sustainable Energy Reviews* 148 (Sept. 2021), p. 111221. ISSN: 13640321. DOI: 10.1016/j.rser.2021.111221. URL: https://linkinghub.elsevier.com/retrieve/pii/S1364032121005086 (visited on 07/06/2024).

[4] R. J. Barthelmie and L. E. Jensen. “Evaluation of Wind Farm Efficiency and Wind Turbine Wakes at the Nysted Offshore Wind Farm”. In: *Wind Energy* 13.6 (Sept. 2010), pp. 573–586. ISSN: 1095-4244, 1099-1824. DOI: 10.1002/we.408. URL: https://onlinelibrary.wiley.com/doi/10.1002/we.408 (visited on 07/07/2024).

[5] Majid Bastankhah and Fernando Porté-Agel. “Experimental and Theoretical Study of Wind Turbine Wakes in Yawed Conditions”. In: *Journal of Fluid Mechanics* 806 (Nov. 10, 2016), pp. 506–541. ISSN: 0022-1120, 1469-7645. DOI: 10.1017/jfm.2016.595. URL: https://www.cambridge.org/core/product/identifier/S0022112016005954/type/journal_article (visited on 07/06/2024).

[6] Juliaan Bossuyt et al. “Quantification of Wake Shape Modulation and Deflection for Tilt and Yaw Misaligned Wind Turbines”. In: *Journal of Fluid Mechanics* 917 (June 25, 2021), A3. ISSN: 0022-1120, 1469-7645. DOI: 10.1017/jfm.2021.237. URL: https://www.cambridge.org/core/product/identifier/S0022112021002378/type/journal_article (visited on 07/11/2024).

[7] Matthieu Boudreau and Guy Dumas. “Comparison of the Wake Recovery of the Axial-Flow and Cross-Flow Turbine Concepts”. In: *Journal of Wind Engineering and Industrial Aerodynamics* 165 (June 2017), pp. 137–152. ISSN: 01676105. DOI: 10.1016/j.jweia.2017.03.010. URL: https://linkinghub.elsevier.com/retrieve/pii/S0167610516305633 (visited on 07/31/2024).

[8] Raúl Bayoán Cal et al. “Experimental Study of the Horizontally Averaged Flow Structure in a Model Wind-Turbine Array Boundary Layer”. In: *Journal of Renewable and Sustainable Energy* 2.1 (Jan. 1, 2010), p. 013106. ISSN: 1941-7012. DOI: 10.1063/1.3289735. URL: https://pubs.aip.org/jrse/article/2/1/013106/284553/Experimental-study-of-the-horizontally-averaged (visited on 07/06/2024).

[9] Marc Calaf, Charles Meneveau, and Johan Meyers. “Large Eddy Simulation Study of Fully Developed Wind-Turbine Array Boundary Layers”. In: *Physics of Fluids* 22.1 (Jan. 1, 2010), p. 015110. ISSN: 1070-6631, 1089-7666. DOI: 10.1063/1.3291077. URL: https://pubs.aip.org/pof/article/22/1/015110/256621/Large-eddy-simulation-study-of-fully-developed (visited on 07/06/2024).

[10] Filippo Campagnolo et al. “Wind Tunnel Testing of Wake Control Strategies”. In: *2016 American Control Conference (ACC)*. 2016 American Control Conference (ACC). Boston, MA, USA: IEEE, July 2016, pp. 513–518. ISBN: 978-1-4673-8682-1. DOI: 10.1109/ACC.2016.7524965. URL: http://ieeexplore.ieee.org/document/7524965/ (visited on 07/06/2024).

[11] Helena Canet, Pietro Bortolotti, and Carlo L. Bottasso. “On the Scaling of Wind Turbine Rotors”. In: *Wind Energy Science* 6.3 (May 3, 2021), pp. 601–626. ISSN: 2366-7451. DOI: 10.5194/wes-6-601-2021. URL: https://wes.copernicus.org/articles/6/601/2021/ (visited on 07/06/2024).

[12] Matthew J. Churchfield et al. “A Numerical Study of the Effects of Atmospheric and Wake Turbulence on Wind Turbine Dynamics”. In: *Journal of Turbulence* 13 (Jan. 2012), N14. ISSN: 1468-5248. DOI: 10.1080/14685248.2012.668191. URL: https://www.tandfonline.com/doi/full/10.1080/14685248.2012.668191 (visited on 07/06/2024).

[13] James J. Cutler et al. “Optimization of Turbine Tilt in a Wind Farm”. In: *AIAA Scitech 2021 Forum*. AIAA Scitech 2021 Forum. VIRTUAL EVENT: American Institute of Aeronautics and Astronautics, Jan. 11, 2021. ISBN: 978-1-62410-609-5. DOI: 10.2514/6.2021-1180. URL: https://arc.aiaa.org/doi/10.2514/6.2021-1180 (visited on 07/06/2024).

[14] John O. Dabiri. “Potential Order-of-Magnitude Enhancement of Wind Farm Power Density via Counter-Rotating Vertical-Axis Wind Turbine Arrays”. In: *Journal of Renewable and Sustainable Energy* 3.4 (July 1, 2011), p. 043104. ISSN: 1941-7012. DOI: 10.1063/1.3608170. URL: https://pubs.aip.org/jrse/article/3/4/043104/284824/Potential-order-of-magnitude-enhancement-of-wind (visited on 07/15/2024).

[15] D.A.M. De Tavernier. “Aerodynamic Advances in Vertical-Axis Wind Turbines”. [object Object], 2021. DOI: 10.4233/UUID:7086F01F-28E7-4E1B-BF97-BB3E38DD22B9. URL: http://resolver.tudelft.nl/uuid:7086f01f-28e7-4e1b-bf97-bb3e38dd22b9 (visited on 04/17/2024).

[16] Noah S. Diffenbaugh and Elizabeth A. Barnes. “Data-Driven Predictions of the Time Remaining until Critical Global Warming Thresholds Are Reached”. In: *Proceedings of the National Academy of Sciences* 120.6 (Feb. 7, 2023), e2207183120. ISSN: 0027-8424, 1091-6490. DOI: 10.1073/pnas.2207183120. URL: https://pnas.org/doi/10.1073/pnas.2207183120 (visited on 04/17/2024).

[17] G. E. Elsinga et al. “Tomographic Particle Image Velocimetry”. In: *Experiments in Fluids* 41.6 (Dec. 2006), pp. 933–947. ISSN: 0723-4864, 1432-1114. DOI: 10.1007/s00348-006-0212-z. URL: http://link.springer.com/10.1007/s00348-006-0212-z (visited on 07/11/2024).

[18] Carlos Jose Simao Ferreira. “The near Wake of the VAWT 2D and 3D Views of the VAWT Aerodynamics.”

[19] Paul Fleming et al. “A Simulation Study Demonstrating the Importance of Large-Scale Trailing Vortices in Wake Steering”. In: *Wind Energy Science* 3.1 (May 14, 2018), pp. 243–255. ISSN: 2366-7451. DOI: 10.5194/wes-3-243-2018. URL: https://wes.copernicus.org/articles/3/243/2018/ (visited on 07/06/2024).

[20] Paul Fleming et al. “Continued Results from a Field Campaign of Wake Steering Applied at a Commercial Wind Farm – Part 2”. In: *Wind Energy Science* 5.3 (July 24, 2020), pp. 945–958. ISSN: 2366-7451. DOI: 10.5194/wes-5-945-2020. URL: https://wes.copernicus.org/articles/5/945/2020/ (visited on 07/06/2024).

[21] Paul A. Fleming et al. “Wind Plant System Engineering through Optimization of Layout and Yaw Control”. In: *Wind Energy* 19.2 (Feb. 2016), pp. 329–344. ISSN: 1095-4244, 1099-1824. DOI: 10.1002/we.1836. URL: https://onlinelibrary.wiley.com/doi/10.1002/we.1836 (visited on 08/14/2024).

[22] Sten Frandsen. “On the Wind Speed Reduction in the Center of Large Clusters of Wind Turbines”. In: *Journal of Wind Engineering and Industrial Aerodynamics* 39.1-3 (Jan. 1992), pp. 251–265. ISSN: 01676105. DOI: 10.1016/0167-6105(92)90551-K. URL: https://linkinghub.elsevier.com/retrieve/pii/016761059290551K (visited on 07/06/2024).

[23] Y. G. Guezennec et al. “Algorithms for Fully Automated Three-Dimensional Particle Tracking Velocimetry”. In: *Experiments in Fluids* 17.4 (Aug. 1994), pp. 209–219. ISSN: 0723-4864, 1432-1114. DOI: 10.1007/BF00203039. URL: http://link.springer.com/10.1007/BF00203039 (visited on 10/08/2023).

[24] Nicholas Hamilton et al. “Statistical Analysis of Kinetic Energy Entrainment in a Model Wind Turbine Array Boundary Layer”. In: *Journal of Renewable and Sustainable Energy* 4.6 (Nov. 1, 2012), p. 063105. ISSN: 1941-7012. DOI: 10.1063/1.4761921. URL: https://pubs.aip.org/jrse/article/4/6/063105/285984/Statistical-analysis-of-kinetic-energy-entrainment (visited on 07/06/2024).

[25] Kurt S. Hansen et al. “The Impact of Turbulence Intensity and Atmospheric Stability on Power Deficits Due to Wind Turbine Wakes at Horns Rev Wind Farm”. In: *Wind Energy* 15.1 (Jan. 2012), pp. 183–196. ISSN: 1095-4244, 1099-1824. DOI: 10.1002/we.512. URL: https://onlinelibrary.wiley.com/doi/10.1002/we.512 (visited on 07/07/2024).

[26] Seyed Hossein Hezaveh et al. “Increasing the Power Production of Vertical-Axis Wind-Turbine Farms Using Synergistic Clustering”. In: *Boundary-Layer Meteorology* 169.2 (Nov. 2018), pp. 275–296. ISSN: 0006-8314, 1573-1472. DOI: 10.1007/s10546-018-0368-0. URL: http://link.springer.com/10.1007/s10546-018-0368-0 (visited on 08/06/2024).

[27] T.C. Hohman, L. Martinelli, and A.J. Smits. “The Effect of Blade Geometry on the Structure of Vertical Axis Wind Turbine Wakes”. In: *Journal of Wind Engineering and Industrial Aerodynamics* 207 (Dec. 2020), p. 104328. ISSN: 01676105. DOI: 10.1016/j.jweia.2020.104328. URL: https://linkinghub.elsevier.com/retrieve/pii/S0167610520302385 (visited on 07/06/2024).

[28] Michael F. Howland, Sanjiva K. Lele, and John O. Dabiri. “Wind Farm Power Optimization through Wake Steering”. In: *Proceedings of the National Academy of Sciences* 116.29 (July 16, 2019), pp. 14495–14500. ISSN: 0027-8424, 1091-6490. DOI: 10.1073/pnas.1903680116. URL: https://pnas.org/doi/full/10.1073/pnas.1903680116 (visited on 07/06/2024).

[29] Michael F. Howland et al. “Wake Structure in Actuator Disk Models of Wind Turbines in Yaw under Uniform Inflow Conditions”. In: *Journal of Renewable and Sustainable Energy* 8.4 (July 1, 2016), p. 043301. ISSN: 1941-7012. DOI: 10.1063/1.4955091. URL: https://pubs.aip.org/jrse/article/8/4/043301/841090/Wake-structure-in-actuator-disk-models-of-wind (visited on 07/06/2024).

[30] M Huang et al. “Experimental Comparison of the Wake of a Vertical Axis Wind Turbine and Planar Actuator Surfaces”. In: *Journal of Physics: Conference Series* 1618.5 (Sept. 1, 2020), p. 052063. ISSN: 1742-6588, 1742-6596. DOI: 10.1088/1742-6596/1618/5/052063. URL: https://iopscience.iop.org/article/10.1088/1742-6596/1618/5/052063 (visited on 04/17/2024).

[31] M. Huang. “Wake and Wind Farm Aerodynamics of Vertical Axis Wind Turbines”. Delft University of Technology, 2023. DOI: 10.4233/UUID:14619578-E44F-45BB-A213-A9D179A54264. URL: http://resolver.tudelft.nl/uuid:14619578-e44f-45bb-a213-a9d179a54264 (visited on 07/04/2024).

[32] Ming Huang, Andrea Sciacchitano, and Carlos Ferreira. “On the Wake Deflection of Vertical Axis Wind Turbines by Pitched Blades”. In: *Wind Energy* 26.4 (Apr. 2023), pp. 365–387. ISSN: 1095-4244, 1099-1824. DOI: 10.1002/we.2803. URL: https://onlinelibrary.wiley.com/doi/10.1002/we.2803 (visited on 04/17/2024).

[33] Ángel Jiménez, Antonio Crespo, and Emilio Migoya. “Application of a LES Technique to Characterize the Wake Deflection of a Wind Turbine in Yaw”. In: *Wind Energy* 13.6 (Sept. 2010), pp. 559–572. ISSN: 1095-4244, 1099-1824. DOI: 10.1002/we.380. URL: https://onlinelibrary.wiley.com/doi/10.1002/we.380 (visited on 07/06/2024).

[34] C Jux. “Robotic Volumetric Particle Tracking Velocimetry by Coaxial Imaging and Illumination”. In: ().

[35] Matthias Kinzel, Quinn Mulligan, and John O. Dabiri. “Energy Exchange in an Array of Vertical-Axis Wind Turbines”. In: *Journal of Turbulence* 13 (Jan. 2012), N38. ISSN: 1468-5248. DOI: 10.1080/14685248.2012.712698. URL: https://www.tandfonline.com/doi/full/10.1080/14685248.2012.712698 (visited on 08/06/2024).

[36] J. Kitzhofer and C. Brücker. “Tomographic Particle Tracking Velocimetry Using Telecentric Imaging”. In: *Experiments in Fluids* 49.6 (Dec. 2010), pp. 1307–1324. ISSN: 0723-4864, 1432-1114. DOI: 10.1007/s00348-010-0879-z. URL: http://link.springer.com/10.1007/s00348-010-0879-z (visited on 10/08/2023).

[37] Elektra Kleusberg, Philipp Schlatter, and Dan S. Henningson. “Parametric Dependencies of the Yawed Wind□turbine Wake Development”. In: *Wind Energy* 23.6 (June 2020), pp. 1367–1380. ISSN: 1095-4244, 1099-1824. DOI: 10.1002/we.2395. URL: https://onlinelibrary.wiley.com/doi/10.1002/we.2395 (visited on 07/16/2024).

[38] H.F. Lam and H.Y. Peng. “Measurements of the Wake Characteristics of Co- and Counter-Rotating Twin H-rotor Vertical Axis Wind Turbines”. In: *Energy* 131 (July 2017), pp. 13–26. ISSN: 03605442. DOI: 10.1016/j.energy.2017.05.015. URL: https://linkinghub.elsevier.com/retrieve/pii/S0360544217307600 (visited on 08/09/2024).

[39] Bruce LeBlanc and Carlos Ferreira. “Estimation of Blade Loads for a Variable Pitch Vertical Axis Wind Turbine from Particle Image Velocimetry”. In: *Wind Energy* 25.2 (Feb. 2022), pp. 313–332. ISSN: 1095-4244, 1099-1824. DOI: 10.1002/we.2674. URL: https://onlinelibrary.wiley.com/doi/10.1002/we.2674 (visited on 07/06/2024).

[40] J. Gordon Leishman. *Principles of Helicopter Aerodynamics*. 2nd ed. Cambridge Aerospace Series 18. Cambridge: Cambridge University press, 2006. ISBN: 978-0-521-85860-1.

[41] Lorenzo E M Lignarolo. “ON THE TURBULENT MIXING IN HORIZONTAL AXIS WIND TURBINE WAKES”.

[42] Lorenzo E M Lignarolo, Daniele Ragni, and Carlos J Simão Ferreira. “Wind Turbine and Actuator Disc Wake: Two Experimental Campaigns”. In: (2015).

[43] Paolo Luzzatto-Fegiz and Colm-cille P. Caulfield. “An Entrainment Model for Fully-Developed Wind Farms: Effects of Atmospheric Stability and an Ideal Limit for Wind Farm Performance”. In: *Physical Review Fluids* 3.9 (Sept. 10, 2018), p. 093802. ISSN: 2469-990X. DOI: 10.1103/PhysRevFluids.3.093802. arXiv: 1703.06553 [physics]. URL: http://arxiv.org/abs/1703.06553 (visited on 07/15/2024).

[44] Bernd Möller et al. “Evaluation of Offshore Wind Resources by Scale of Development”. In: *Energy* 48.1 (Dec. 2012), pp. 314–322. ISSN: 03605442. DOI: 10.1016/j.energy.2012.01.029. URL: https://linkinghub.elsevier.com/retrieve/pii/S0360544212000345 (visited on 04/18/2024).

[45] A S Monin. “The Atmospheric Boundary Layer”. In: *Annual Review of Fluid Mechanics* 2 (Volume 2, 1970 1970), pp. 225–250. ISSN: 1545-4479. DOI: 10.1146/annurev.fl.02.010170.001301. URL: https://www.annualreviews.org/content/journals/10.1146/annurev.fl.02.010170.001301.

[46] *North Sea Programme 2022-2027*. Netherlands: Government of the Netherlands, Mar. 2022, p. 158. URL: https://www.noordzeeloket.nl/en/policy/north-sea-programme-2022-2027/.

[47] *Wind Energy in Europe: 2022 Statistics and the Outlook for 2023-2027*. WindEurope, p. 58. URL: https://windeurope.org/intelligence-platform/product/wind-energy-in-europe-2022-statistics-and-the-outlook-for-2023-2027/.

[48] Alfredo Peña and Ole Rathmann. “Atmospheric Stability□dependent Infinite Wind□farm Models and the Wake□decay Coefficient”. In: *Wind Energy* 17.8 (Aug. 2014), pp. 1269–1285. ISSN: 1095-4244, 1099-1824. DOI: 10.1002/we.1632. URL: https://onlinelibrary.wiley.com/doi/10.1002/we.1632 (visited on 04/22/2024).

[49] Fernando Porté-Agel, Majid Bastankhah, and Sina Shamsoddin. “Wind-Turbine and Wind-Farm Flows: A Review”. In: *Boundary-Layer Meteorology* 174.1 (Jan. 2020), pp. 1–59. ISSN: 0006-8314, 1573-1472. DOI: 10.1007/s10546-019-00473-0. URL: http://link.springer.com/10.1007/s10546-019-00473-0 (visited on 07/06/2024).

[50] Antonio Posa et al. “Wake Structure of a Single Vertical Axis Wind Turbine”. In: *International Journal of Heat and Fluid Flow* 61 (Oct. 2016), pp. 75–84. ISSN: 0142727X. DOI: 10.1016/j.ijheatfluidflow.2016.02.002. URL: https://linkinghub.elsevier.com/retrieve/pii/S0142727X16300285 (visited on 07/06/2024).

[51] Vincent F-C. Rolin and Fernando Porté-Agel. “Experimental Investigation of Vertical-Axis Wind-Turbine Wakes in Boundary Layer Flow”. In: *Renewable Energy* 118 (Apr. 2018), pp. 1–13. ISSN: 09601481. DOI: 10.1016/j.renene.2017.10.105. URL: https://linkinghub.elsevier.com/retrieve/pii/S0960148117310753 (visited on 05/30/2024).

[52] Fulvio Scarano et al. “On the Use of Helium-Filled Soap Bubbles for Large-Scale Tomographic PIV in Wind Tunnel Experiments”. In: *Experiments in Fluids* 56.2 (Feb. 2015), p. 42. ISSN: 0723-4864, 1432-1114. DOI: 10.1007/s00348-015-1909-7. URL: http://link.springer.com/10.1007/s00348-015-1909-7 (visited on 04/17/2024).

[53] Daniel Schanz et al. “‘Shake The Box’: A Highly Efficient and Accurate Tomographic Particle Tracking Velocimetry (TOMO-PTV) Method Using Prediction of Particle Positions”. In: ().

[54] Jan F. G. Schneiders et al. “Large-Scale Volumetric Pressure from Tomographic PTV with HFSB Tracers”. In: *Experiments in Fluids* 57.11 (Nov. 2016), p. 164. ISSN: 0723-4864, 1432-1114. DOI: 10.1007/s00348-016-2258-x. URL: http://link.springer.com/10.1007/s00348-016-2258-x (visited on 07/19/2024).

[55] Matt Shields et al. “Impacts of Turbine and Plant Upsizing on the Levelized Cost of Energy for Offshore Wind”. In: *Applied Energy* 298 (Sept. 2021), p. 117189. ISSN: 03062619. DOI: 10.1016/j.apenergy.2021.117189. URL: https://linkinghub.elsevier.com/retrieve/pii/S0306261921006164 (visited on 04/17/2024).

[56] G. Sieros et al. "Upscaling Wind Turbines: Theoretical and Practical Aspects and Their Impact on the Cost of Energy". In: *Wind Energy* 15.1 (Jan. 2012), pp. 3–17. ISSN: 1095-4244, 1099-1824. DOI: 10.1002/we.527. URL: https://onlinelibrary.wiley.com/doi/10.1002/we.527 (visited on 04/17/2024).

[57] J N Sørensen, G C Larsen, and A Cazin-Bourguignon. "Production and Cost Assessment of Offshore Wind Power in the North Sea". In: *Journal of Physics: Conference Series* 1934.1 (May 1, 2021), p. 012019. ISSN: 1742-6588, 1742-6596. DOI: 10.1088/1742-6596/1934/1/012019. URL: https://iopscience.iop.org/article/10.1088/1742-6596/1934/1/012019 (visited on 04/22/2024).

[58] Jens Nørkær Sørensen and Gunner Christian Larsen. "A Minimalistic Prediction Model to Determine Energy Production and Costs of Offshore Wind Farms". In: *Energies* 14.2 (Jan. 15, 2021), p. 448. ISSN: 1996-1073. DOI: 10.3390/en14020448. URL: https://www.mdpi.com/1996-1073/14/2/448 (visited on 04/22/2024).

[59] Roland Stull. *Practical Meteorology: An Algebra-Based Survey of Atmospheric Science*. Place of publication not identified: publisher not identified, 2015. ISBN: 978-0-88865-176-1.

[60] G. Tescione. "On the Aerodynamics of a Vertical Axis Wind Turbine Wake: An Experimental and Numerical Study". Delft University of Technology, 2016. DOI: 10.4233/UUID:86AC7352-46B8-4C2D-9014-817472D80174. URL: http://resolver.tudelft.nl/uuid:86ac7352-46b8-4c2d-9014-817472d80174 (visited on 07/06/2024).

[61] Willy Tjiu et al. "Darrieus Vertical Axis Wind Turbine for Power Generation I: Assessment of Darrieus VAWT Configurations". In: *Renewable Energy* 75 (Mar. 2015), pp. 50–67. ISSN: 09601481. DOI: 10.1016/j.renene.2014.09.038. URL: https://linkinghub.elsevier.com/retrieve/pii/S096014811400603X (visited on 07/06/2024).

[62] Antoine Vergaerde et al. "Experimental Characterisation of the Wake behind Paired Vertical-Axis Wind Turbines". In: *Journal of Wind Engineering and Industrial Aerodynamics* 206 (Nov. 2020), p. 104353. ISSN: 01676105. DOI: 10.1016/j.jweia.2020.104353. URL: https://linkinghub.elsevier.com/retrieve/pii/S0167610520302634 (visited on 08/09/2024).

[63] Claire VerHulst and Charles Meneveau. "Altering Kinetic Energy Entrainment in Large Eddy Simulations of Large Wind Farms Using Unconventional Wind Turbine Actuator Forcing". In: *Energies* 8.1 (Jan. 6, 2015), pp. 370–386. ISSN: 1996-1073. DOI: 10.3390/en8010370. URL: https://www.mdpi.com/1996-1073/8/1/370 (visited on 07/11/2024).

[64] L.J. Vermeer, J.N. Sørensen, and A. Crespo. "Wind Turbine Wake Aerodynamics". In: *Progress in Aerospace Sciences* 39.6-7 (Aug. 2003), pp. 467–510. ISSN: 03760421. DOI: 10.1016/S0376-0421(03)00078-2. URL: https://linkinghub.elsevier.com/retrieve/pii/S0376042103000782 (visited on 07/06/2024).

[65] Chengyu Wang et al. *How Realistic Are the Wakes of Scaled Wind Turbine Models?* Nov. 10, 2020. DOI: 10.5194/wes-2020-115. URL: https://wes.copernicus.org/preprints/wes-2020-115/wes-2020-115.pdf (visited on 07/06/2024). Pre-published.

[66] Miao Weipao et al. "Numerical Investigation of Wake Control Strategies for Maximizing the Power Generation of Wind Farm". In: *Journal of Solar Energy Engineering* 138.3 (June 1, 2016), p. 034501. ISSN: 0199-6231, 1528-8986. DOI: 10.1115/1.4033110. URL: https://asmedigitalcollection.asme.org/solarenergyengineering/article/doi/10.1115/1.4033110/379529/Numerical-Investigation-of-Wake-Control-Strategies (visited on 07/06/2024).